



TECHNISCHE UNIVERSITÄT MÜNCHEN
Fakultät für Elektrotechnik und Informationstechnik

Methods for standardizing and enhancing Biomedical Fluorescence Imaging

Maria Anastasopoulou

Vollständiger Abdruck der von der Fakultät für Elektrotechnik und Informationstechnik der Technischen Universität München zur Erlangung des akademischen Grades einer

Doktorin der Ingenieurwissenschaften (Dr.-Ing.)

genehmigten Dissertation.

Vorsitzender: Prof. Dr.-Ing. Christian Jirauschek

Prüfer der Dissertation:

1. Prof. Dr. Vasilis Ntziachristos
2. Prof. Dr.-Ing. habil. Dr. h.c. Alexander W. Koch

Die Dissertation wurde am 27.10.2020 bei der Technischen Universität München eingereicht und durch die Fakultät für Elektrotechnik und Informationstechnik am 31.08.2021 angenommen.

Contents

Abstract	5
Zusammenfassung	7
Abbreviations	9
1. Introduction to Fluorescence Imaging and Motivation	10
1.1 Introduction to Fluorescence Imaging	10
1.2 Challenges and Thesis Motivation	14
1.2.1 Dependence on camera system	14
1.2.2 Dependence on tissue optical properties	14
1.2.3 Thesis goal	15
2. Standardization for Fluorescence Imaging (FI)	17
2.1 The Need for Standardization in FI	17
2.2 Design Criteria for Phantoms	17
2.2.1 Optical properties	17
2.2.2 Other design factors that should be considered	18
2.3 Material Selection for Phantom Fabrication	18
2.3.1 Matrix material	18
2.3.2 Scattering agent	19
2.3.3 Absorbing agent	19
2.3.4 Fluorescent agent.....	19
2.3.5 Fabrication techniques	20
2.4 Comprehensive Phantoms	20
2.4.1 Phantom description	21
2.4.2 Phantom fabrication process	22
2.4.3 Phantom optical properties characterization process.....	23
2.4.4 Discussion	24
3. Fluorescence Imaging (FI) Enhancement	26
3.1 Optical Properties of Tissue	26
3.1.1 Optical properties as tissue biomarkers.....	26
3.1.2 Absorption and scattering as a fluorescence signal distortion factor	26
3.2 Resolution and Contrast Correction	27
3.2.1 Methods for enhancing the resolution in FI	27

3.3 Fluorescence Diffusion Correction Through a Spatially Variant Deconvolution Scheme	28
3.3.1 Method description	29
3.3.2 Discussion	31
3.4 SWIR Imaging	32
3.5 Fluorescence Intensity Disengagement from Optical Properties	34
3.5.1 Requirements for a new method	34
4. Conclusion and Future Outlook: Toward a New Framework	36
5. References	39
Appendix A. Publication 1: Comprehensive Phantom for interventional fluorescence molecular imaging	48
Appendix B. Publication 2: Fluorescence imaging reversion using spatially variant deconvolution	71
Appendix C. Publication Record	97
Appendix D. Acknowledgements	99
Appendix E. Letters of approval from publishers	101

Abstract

Fluorescence imaging in the near-infrared spectral range has unlocked new imaging possibilities in surgical guidance over the past decade. With the administration of fluorescent agents into the tissue and the use of highly sensitive fluorescence cameras, pathophysiological tissue sites that are invisible to human vision can be identified during a surgical operation. The advent of fluorescence agents that target specific molecular characteristics of disease has facilitated the identification and demarcation of cancerous tissue with greater sensitivity and accuracy over nonspecific fluorescence agents that circulate in the vascular system. Despite the advances in cameras and specificity of fluorescence agents, fluorescence imaging still faces challenges toward its clinical translation. The aim of this work is to propose novel solutions to overcome these challenges.

The first challenge is the lack of calibration and standardization of fluorescence imaging systems. There are various fluorescence imaging systems across different laboratories and clinics, and each system operates with a combination of parameters such as exposure time, working distance, gain, and magnification. The variety of interlaboratory systems and imaging parameters highlights the need to calibrate the system before the measurement to ensure the best performance and reproducibility of the imaging results for the same target. To tackle this challenge, we present the first and second generation of comprehensive solid phantoms that can simultaneously evaluate multiple system parameters. These parameters include camera sensitivity, fluorescence intensity variations as a function of optical properties and depth, illumination homogeneity, optical and fluorescence resolution, and cross talk from excitation light and parasitic illumination leaking into the fluorescence channel. Moreover, these phantoms can be employed for the correction of inhomogeneous illumination.

The second challenge of fluorescence imaging is the distortion of the fluorescence signal due to tissue scattering and absorption. Photon diffusion in tissue distorts image quality. Poor image resolution and contrast make tumor delineation difficult, leading to ambiguity in the interpretation of the image. Thus, incomplete tumor resection or excessive healthy tissue removal can occur, both of which negatively affect patients' quality of life. In this thesis, a new method for fluorescence imaging enhancement is proposed that takes into account tissue heterogeneity, unlike traditional methods that presume tissue homogeneity. We introduce the concept of scanning the tissue with a point-like beam to acquire spatially variant impulse responses (kernels) that are dependent on the local optical properties. Subsequently, these kernels are used in a fast, spatially variant deconvolution scheme to revert the degradation of image quality.

Experimental measurements from phantoms and ex vivo mice were used, and improvements were shown and validated.

Finally, the correction of intensity values in fluorescence imaging is discussed in the context of a method that could be applied as an extension of the spatially variant deconvolution method. Overall, a comprehensive framework comprising all correction methods described in this thesis is suggested, and a future outlook is described.

Zusammenfassung

Die Fluoreszenzbildgebung im nahen Infrarotspektralbereich hat in den letzten zehn Jahren in der chirurgischen Anleitung neue Bildgebungsmöglichkeiten eröffnet. Durch die Verabreichung von Fluoreszenzmitteln in das Gewebe und die Verwendung hochempfindlicher Fluoreszenzkameras können pathophysiologische Gewebestellen, die für den unsichtbar sind, während einer Operation identifiziert werden. Das Aufkommen neuer Fluoreszenzmittel, die auf bestimmte molekulare Merkmale von Krankheiten abzielen, hat die Identifizierung und Abgrenzung von Krebsgebieten mit größerer Empfindlichkeit und Genauigkeit gegenüber unspezifischen Fluoreszenzmitteln, die im Gefäßsystem zirkulieren, erleichtert. Trotz der Fortschritte bei Kameras und der Spezifität von Fluoreszenzmitteln steht die Fluoreszenzbildgebung immer noch vor Herausforderungen, die ihre klinische Translation verzögern. Ziel dieser Arbeit ist es, neue Lösungen vorzuschlagen, um diese Herausforderungen zu bewältigen.

Die erste Herausforderung hängt mit dem Mangel an Kalibrierung und Standardisierung der Fluoreszenzbildgebungssysteme zusammen. Es gibt eine Vielzahl von Fluoreszenzbildgebungssystemen in verschiedenen Labors und Kliniken, die mit einer Kombination verschiedener Parameter wie Belichtungszeit, Arbeitsabstand, Verstärkung, Vergrößerung usw. arbeiten. Diese Vielzahl von Systemen und Bildgebungsparametern macht es unbedingt erforderlich, das System vor der Messung zu kalibrieren, um die beste Leistung und Reproduzierbarkeit der Bildgebungsergebnisse für dasselbe Ziel sicherzustellen. Um dieser Herausforderung zu begegnen, präsentieren wir hier die erste und zweite Generation von umfassenden festen Phantomen, die gleichzeitig mehrere Systemparameter wie Kameraempfindlichkeit, Fluoreszenzintensitätsschwankungen als Funktion der optischen Eigenschaften und der Tiefe, Beleuchtungshomogenität, optische und Fluoreszenzauflösung sowie Interferenzen von Anregungslicht und parasitärer Beleuchtung, die in den Fluoreszenzkanal gelangen, bewerten können. Darüber hinaus können diese Phantome zur Korrektur inhomogener Beleuchtung eingesetzt werden.

Die zweite Herausforderung der Fluoreszenzbildgebung hängt mit der Verzerrung des Fluoreszenzsignals aufgrund von Gewebestreuung und -absorption zusammen. Die Photonendiffusion im Gewebe verzerrt die Bildqualität. Eine schlechte Bildauflösung und ein schlechter Kontrast erschweren die Tumorabgrenzung und führen zu Mehrdeutigkeiten bei der Interpretation des Bildes. Daher kann es zu einer unvollständigen Tumorsektion oder einer übermäßigen Entfernung von gesundem Gewebe kommen, was sich beides negativ auf die

Lebensqualität des Patienten auswirken. In dieser Arbeit wird eine neue Methode zur Verbesserung der Fluoreszenzbildgebung vorgeschlagen, die die Heterogenität des Gewebes berücksichtigt, im Gegensatz zu herkömmlichen Methoden, die eine Homogenität des Gewebes voraussetzen. Wir führen das Konzept ein, das Gewebe mit einem punktförmigen Strahl abzutasten, um räumlich variierende Impulsantworten (Kernel) zu erhalten, die von den lokalen optischen Eigenschaften abhängen. Anschließend werden diese Kernel in einem schnellen räumlich varianten Entfaltungsschema verwendet, um die Verschlechterung der Bildqualität umzukehren. Experimentelle Messungen von Phantomen und Ex-vivo-Mäusen wurden verwendet und Verbesserungen wurden gezeigt und validiert.

Schließlich wird die Korrektur von Intensitätswerten in der Fluoreszenzbildgebung im Zusammenhang mit einem Verfahren diskutiert, das als Erweiterung des räumlich varianten Entfaltungsverfahrens angewendet werden könnte. Insgesamt wird ein umfassender Rahmen vorgeschlagen, der alle in dieser Arbeit beschriebenen Korrekturmethode umfasst, und Zukunftsperspektiven werden beschrieben.

Abbreviations

ALA	Aminolevulinic Acid
CCD	Charge Coupled Device
DLP	Digital Light Processing
FDA	Food and Drug Administration
FI	Fluorescence Imaging
FMI	Fluorescence Molecular Imaging
FOV	Field of View
ICG	IndoCyanine Green
NIR	Near InfraRed
QDs	Quantum Dots
SDR	Spatially Diffused Reflectance
SNR	Signal to Noise Ratio
SWIR	Shortwave Infrared
TiO ₂	Titanium Dioxide
USAF	United States Air Force

1. Introduction to Fluorescence Imaging and Motivation

1.1 Introduction to Fluorescence Imaging

Surgical intervention can be the leading choice for disease treatment, especially regarding malignancies. For a positive disease prognosis, the success of a tumor resection lies in accurate malignant tissue detection and area demarcation. This suggests that even though the cancerous area was defined initially through diagnostic tests before the surgical operation, there is a need for real-time surgical guidance and accurate tumor localization during the resection process. Conventionally, during surgical or endoscopic operations, surgical guidance is achieved either by the experienced eye of the surgeon or by conventional color cameras operating in the visible wavelength spectrum (400–700 nm). Despite the benefits of this approach on resection guidance, the lack of contrast between healthy and diseased tissue remains the main challenge. The differentiation among tissue structures is not always recognizable, and the subsurface malignant structures are not easily detectable. Even though there are various potent imaging methods for diagnostic purposes such as computed tomography, magnetic resonance imaging, positron emission tomography, single-photon emission tomography, and ultrasound imaging, imaging options for intraoperative guidance are limited [1],[2]. In addition, the use of ionizing radiation such as X- or gamma rays [3] can induce hazardous side effects. In contrast, the emergence of interventional fluorescence imaging (FI) with new fluorescence contrast agents has opened new opportunities for surgical guidance [4]–[7]. Fluorescence imaging fulfills the requirements of real-time, high-contrast, sensitive, cost-effective imaging technology in the operation room.

FI has been broadly explored as a potential tool for surgical guidance in preclinical and clinical environments, [8]–[10] and it can address the limitations of white light imaging, such as the inefficiency of healthy–unhealthy tissue differentiation, and improve cancer detection. It presents the advantages of high sensitivity, multiplexed real-time imaging, and subsurface signal detection in surgical or endoscopic guidance.

The detection wavelength at the camera sensor in FI usually lies in the so-called near-infrared (NIR) or therapeutic window (700–1000 nm). At the NIR window, the absorption of hemoglobin and water, the main absorbers in tissue, is low compared to other spectral regions. Moreover, the amount of scattered light is significantly lower at the NIR than the visible (400–700 nm) window, increasing the light penetration depth. Another desirable property of FI at the NIR is the

low autofluorescence compared to shorter wavelengths. Consequently, imaging of subsurface structures that are several millimeters to centimeters deep is feasible.

The cornerstone of interventional FI is the rendering of contrast among healthy and unhealthy tissues. Contrast can be achieved through three mechanisms: visualizing tissue autofluorescence, using nonspecific fluorescence tracers, or using specific fluorescence tracers. Regarding the first mechanism, several autofluorescence molecules, such as nicotinamide adenine dinucleotide, collagen, and elastin, can be found in tissues. Their main characteristic is that they emit light when they absorb light with certain excitation wavelengths. The advantage of the autofluorescence contrast mechanism in FI is that it does not require the administration of any external fluorescence agent. The administration of external fluorescence agents complicates the imaging procedure because of the risk of potential toxicity with impending harmful effects for the patient. Autofluorescence imaging has been used successfully in intraoperative imaging and minimally invasive FI [11]–[13]. Furthermore, autofluorescence imaging has gained attention in endocrinology because it has been used in several studies to localize the hardly visible parathyroid glands in thyroidectomy and parathyroidectomy [14], [15]. In contrast, apart from particular applications, autofluorescence lacks specificity and does not appear useful in a broad range of malignant tumor resection surgeries. Thus, researchers have given more attention to administering external specific and nonspecific fluorescence agents.

The most widely used nonspecific fluorescence agent is indocyanine green (ICG), broadly used in clinical applications [5],[16] since it was approved by the Food and Drug Administration (FDA) in 1959 [17]. ICG has a long history of use in angiography and a variety of clinical applications. ICG can perfuse tumors through the enhanced permeability and retention effect and has already been employed in tumor imaging for sentinel lymph node mapping [18]–[20]. Another nonspecific dye that has been widely used is methylene blue, which has also been successfully used in sentinel lymph node mapping [21], [22]. Although nonspecific dyes have been widely investigated and employed, their lack of specificity hampers their broad use in tumor resections.

Consequently, research focus has been shifted to the development of fluorescence agents that are tailored to target specific characteristics of cancer cells. Specific tumor uptake is a key requirement for better tumor delineation and a design requirement for the new fluorescence agents. With the advent of fluorescence agents that have better tissue clearance and, most importantly, target specific marker expressions [23], fluorescence molecular imaging (FMI) [4] has become more popular in tumor resection. Despite the fact that the clinical translation of FMI is not fast, the development progress of new agents is encouraging. Recently, the FDA

approved 5-ALA (aminolevulinic acid), which can induce autofluorescence of cancer. It has been successfully employed in malignant gliomas and benign tumor resection [24]–[27]. The first-in-human study [8] with folate (B-vitamin) conjugated to fluorescein isothiocyanate (Folate-FITC) to detect cancer foci in ovarian cancer patients showed promising results that paved the path for subsequent clinical studies [9],[10]. FITC-labeled peptide has been developed and applied to esophageal neoplasia visualization [28] and FITC-labeled adalimumab to Crohn's disease [29]. Many more potential agents are being developed, [5],[30] and some of them are already in phase 2 and 3 clinical trials [31].

On the technical side, various fluorescence camera systems have already been developed for either intraoperative surgery or endoscopy [6],[19],[32],[33]. FI requires a camera with high sensitivity, low readout noise, and high dynamic range. Cameras for FI have been based on different silicon sensor technologies and architectures, such as the complementary metal–oxide semiconductor, the charge-coupled device (CCD), the intensified charge-coupled device, and the electron multiplying coupled device. Each sensor architecture has advantages and disadvantages regarding sensitivity, dynamic range, and noise, parameters that are critical for the quality of the fluorescence image [34],[35]. Furthermore, different camera system configurations range from a single camera to multiple cameras. The simplest and most straightforward system uses a single camera (Fig. 1a), where an objective lens and relay optics image the sample on the camera sensor. A spectral filter selects the light at emission wavelength that will reach the camera sensor. In more complex configurations, images are captured on more than one camera with the same field of view (FOV). Usually the second camera acquires color images (Fig. 1b). The addition of the color camera provides the surgeon with anatomical information of the region for better orientation and guidance. Both images are acquired simultaneously, and the fluorescence image is superimposed on the color image as pseudo color. Other cameras (Fig. 1c) can be used to record other bands of the fluorescence emission spectrum, allowing the simultaneous interrogation of more fluorescence agents (e.g., methylene blue and ICG [18]).

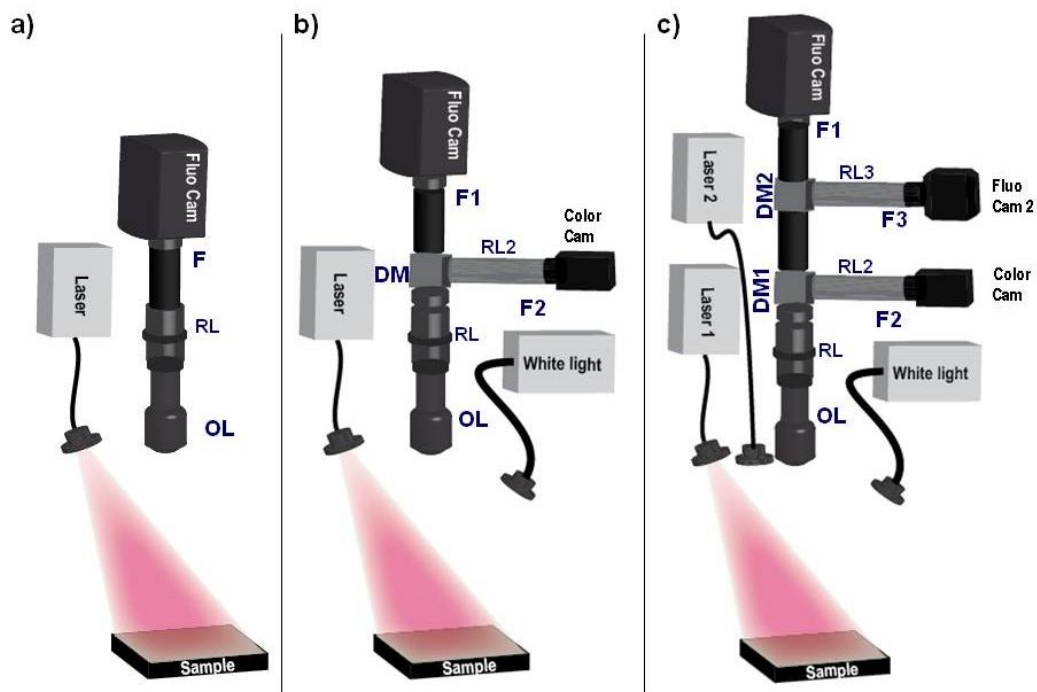


Figure 1: Configurations of fluorescence intraoperative systems. a) Single fluorescence camera system. **b)** Two-camera system: one fluorescence and one color camera. **c)** Three-camera system: two fluorescence and one color camera. OL: Objective lens, RL: Relay lens, F: Emission filter, DM: Dichroic Mirror.

Fluorescence intraoperative systems as well as several configurations of endoscopic and laparoscopic systems have been developed [6],[36],[37]. Promising results in endoscopy [38] and colonoscopy [37],[39] with early lesion detection have already been demonstrated. Finally, apart from the FI systems that have been developed in research laboratories in the context of phantoms and animal experiments, some of them have already been successfully commercialized [7].

1.2 Challenges and Thesis Motivation

Despite the advances in developing camera systems with enhanced sensitivity and resolution and new fluorescence agents with higher specificity and less toxicity, FI still faces some major challenges. These challenges can be divided into two categories according to their relevance to the camera system or tissue optical characteristics.

1.2.1 Dependence on camera system

The wide variety of intraoperative FI systems and their parameters (Fig. 2a) creates a fundamental need to calibrate and standardize them. The imaging results should be reproducible across FI systems and across time for the same sample. Therefore, the FI systems should be calibrated before the measurements, ensuring the best performance. To tackle this issue, a multiparameter phantom, with temporal stability of its optical properties, is required to comprehensively address the parameters of different systems.

1.2.2 Dependence on tissue optical properties

The performance of FI is restricted by the interaction of light with the tissue regardless of its demonstrated clinical potential. The image quality in terms of resolution and accuracy is hampered because of the fluorescence signal dependence on the sample's optical properties. Resolution and contrast degradation of the fluorescence image can have a significant impact on the interpretation of clinical fluorescence images, especially in tumor surgery, where the accurate delineation of the tumor margins is essential for the successful operation outcome. A blurry fluorescence image can lead to incomplete tumor resection or excessive removal of healthy tissue. Incomplete tumor resection can lead to disease recurrence and the need for residual tumor operation and follow-up surgery. In contrast, excessive healthy tissue removal may have immense side effects on the patient's quality of life. For this reason, the resolution and contrast quality of the fluorescence images need to be enhanced. An example of a blurry and a resolved phantom image can be seen in Fig. 2b.

In addition to the degradation of the spatial resolution, absorption and scattering distort the fluorescence intensity as well. For example, each well of the phantom shown in Fig. 2c has the same amount of fluorophore but different absorption and scattering properties. Therefore, the fluorescence intensities vary according to the concentrations of scatterers and absorbers, even though the fluorophore concentrations are the same. This can complicate the discrimination between fluorescently labeled tissues and normal or non-labeled tissues. For example, an area with high attenuation can lead to very low fluorescence signal intensity and inaccurate surgical resectioning for an area of nonmalignancy. Thus, the evaluation of the fluorophore distribution in

tissues would be more accurate if the effects of optical properties on the fluorescence signal were disengaged.

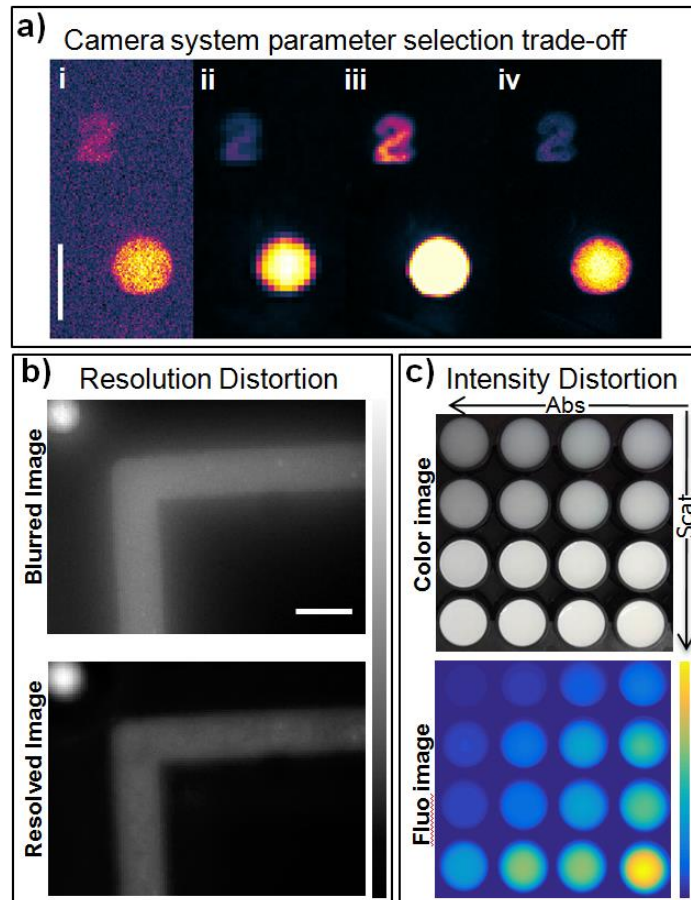


Figure 2: Demonstration of fluorescence imaging challenges. a) Fluorescence image with different system parameters: i) Binning: 1, Exp.Time: 0.1 s, Gain: 500, ii) Binning: 4, Exp.Time: 0.1 s, Gain: 500, iii) Binning: 2, Exp.Time: 0.6 s, Gain: 3000 and iv) Binning: 1, Exp.Time: 0.6 s, Gain: 3000. b) Upper image: Low-resolution fluorescence image due to the effect of optical properties. Lower image: High-resolution fluorescence image. c) Upper: Color. Lower image: Fluorescence image of 16 wells with the same fluorophore concentration and different scattering and absorption properties. Arrows point to absorption increment for each column and scattering increment for each row. Scale bars: 10 mm.

1.2.3 Thesis goal

The scope of this thesis is to address the aforementioned challenges by either suggesting a strategy to overcome them or providing insight for better understanding.

The first goal is to address the calibration and benchmarking requirement for intraoperative fluorescence systems with a proposal for a new standardization phantom. For this challenge, a

novel class of phantoms is introduced in Section 2 and Appendix A. This class of phantoms can be used for the comprehensive and simultaneous assessment of a large range of parameters (e.g., uniformity of illumination, camera dynamic, and sensitivity) required for the clinical use of fluorescence systems.

The second goal is to introduce and demonstrate a novel method for improving both spatial resolution and contrast of fluorescence images that were deteriorated by photon diffusion in tissue. This approach is based on the acquisition of the local spatially resolved reflectance from the tissue, which carries information related to the local optical properties, and its use in a digital processing scheme to enhance the NIR fluorescence images. A raster scanning scheme, acquiring the reflectance profile from each point on the tissue, and the use of a fast deconvolution scheme are employed toward this goal. This method is described and experimentally demonstrated using phantoms and ex vivo tissues in Section 3.3 and Appendix B. Section 3.4 describes a second approach to enhance fluorescence image quality that is based on a totally different concept of shifting the fluorescence signal acquisition to the shortwave infrared (SWIR) regime, and the need to compare it with the conventional NIR imaging regime is highlighted. Finally, in Section 3.5, the requirements for developing a new method to tackle the challenge of fluorescence intensity correction are discussed.

2. Standardization for Fluorescence Imaging (FI)

2.1 The Need for Standardization in FI

FI system parameters, such as exposure time, gain, working distance, magnification, and binning, can be optimized for the best performance before the imaging procedure. Furthermore, different FI devices across laboratories and hospitals have various specifications such as camera types, optical systems, and laser sources. These differences among devices make urgent the need for a standardization methodology that will facilitate the clinical translation of FMI. The recorded results should be able to be reproduced for the same imaging target across different time points and laboratories. Therefore, methods for FMI standardization are required.

Toward this standardization aim, the development of tissue-mimicking phantoms has emerged. Phantoms can be used from simple testing to more comprehensive and complete performance assessments of a system [40]. Phantoms may serve other purposes as well, e.g., the optimization of laser dosimetry [41] and training of surgeons in the use of NIR fluorescence intraoperative systems [42].

2.2 Design Criteria for Phantoms

The design and fabrication of a phantom depend on the specific purpose that it will serve. The optical characteristics of the phantom, alongside other morphological properties, are fundamental design criteria and are discussed below.

2.2.1 Optical properties

The selection of suitable optical properties of phantoms is of utmost importance for their proper application. In particular, when a phantom is intended to be used in a customized application to mimic a specific tissue, it should be fabricated with the greatest accuracy of the desired optical properties. Conversely, for standardization phantoms, such a level of accuracy is not that crucial because their main purpose is to reveal information regarding system parameters. To ensure that the optical properties lie in the design range, a measurement method for the optical properties retrieval is needed. Several methods and inverse models for the estimation of the optical properties of phantoms have been developed, with the most common being diffuse reflectance measurements in the time domain, frequency domain, and spatially resolved steady state. However, there is neither a gold-standard method nor a consensus among laboratories

for the absolute values of optical properties for the same sample. This happens because values of the optical properties may depend on irradiance, time, environmental conditions (e.g., temperature, pressure), the polarization of light, etc. [43]. In this way, the accuracy of the measurement is obscured. Nevertheless, coarse estimations for the absolute values and finer estimations for the relative values of optical properties can be achieved.

2.2.2 Other design factors that should be considered

In addition to the optical properties, some other design factors play a significant role in the utility of the phantom. These design factors need to be considered, such as the mechanical properties, photosensitivity (or the material response to environmental conditions), temporal degradation, and reproducibility. The phantom's specific use determines the specifications that should be met. In the case of phantoms for standardization purposes, the temporal stability of optical and mechanical properties, regardless of environmental conditions, is crucial. Accordingly, phantoms for clinical simulation purposes may require accurate modeling of tissue mechanical properties like softness and elasticity.

2.3 Material Selection for Phantom Fabrication

A subsequent step for phantom fabrication is material selection. Typically, the phantoms consist of four components: the matrix material, a scattering agent, an absorbing agent, and a fluorescence agent. However, there are cases where the same material is used as scatterer and absorber [41],[44] or more than one scatterer or absorber are used [45]. Solvent materials such as ethanol or dimethyl sulfoxide that are used for the homogenization of the other components with the matrix material are commonly used in such low amounts that the impact on the phantom's properties is negligible.

2.3.1 Matrix material

The selection of the matrix material is key in phantom fabrication. Matrix materials such as agar, silicone, polyester, epoxy resin, and polyurethane have been widely employed. Other materials such as polydimethylsiloxane (PDMS) and polyvinyl alcohol cryogel have been recently used, and their use is becoming more extensive. Hydrogels [40] (e.g., agar and gelatin) are considered suitable as matrix materials in many phantom applications because of their mechanical properties and low price. Even though they are low-priced and can be cast into various shape molds, they have the drawback of short durability. When long durability is needed, materials such as polyester, epoxy, and polyurethane [40], [46]–[48] are preferred

because of their rigidity, stability, and compatibility with infrared dyes. Resin phantoms can be used for years without significant optical property change, but they are stiffer than tissues [49]. Consequently, agar and gelatine are preferred for applications that require phantoms to simulate tissue texture for a limited temporal span (days or weeks). In contrast, epoxy, polyester, and polyurethane are suitable for phantoms that require long-term stability, as it is demanded in system standardization and calibration. Another interesting material, broadly used in microfluidics applications, is the silicon-based elastomer, PDMS [50]. It has recently gained attention and has been reported [51],[52] as an eligible matrix material with predictable and repeatable optical properties at NIR.

2.3.2 Scattering agent

The main groups of scattering agents are lipid microparticles, white metal oxide powders, and polymer microparticles [40]. Intralipid is a widespread lipid-based scatterer [53]–[56], an emulsion of soya oil in water. It is one of the most widely studied reference materials in the biomedical optics community. Titanium dioxide [45], [57] and aluminum oxide powders are well-known and extensively used scatterers. In the group of polymer microspheres, polystyrene is the most popular scatterer [40]. Although its scattering properties can be well predicted using Mie theory [58], [59], it can contribute to fluorescence quantum yield decay [60].

2.3.3 Absorbing agent

Some researchers have adopted the addition of blood or blood derivatives as an absorbing agent because of its excellent tissue-mimicking properties. Nevertheless, simpler components like inks and powders are becoming more popular because of the instability of oxygen hemoglobin binding and clotting. Nigrosin, graphite, and Naphthol Green B powders have been reported as useful absorbers [61],[62]. India ink [63], which has a relatively flat absorption spectrum, is the most well-known ink.

2.3.4 Fluorescent agent

The last constituent of a fluorescence imaging phantom is the selection of the fluorescence agent. First, it should be mentioned that there is no specificity requirement. Therefore, the molecular component from the fluorescence agent that provides the specificity (e.g., conjugated antibody) is omitted, and only the fluorescence moiety is used in the phantom. An important requirement is that the emission of the fluorescence agent must be within the wavelength range of the relevant fluorescence imaging application. Photostability also counts as an important factor. For phantoms designated to be used in standardization, quantum dots (QDs) are an

attractive choice [64]–[66]. They do not suffer from fast photobleaching, and they can provide unique emission spectra.

2.3.5 Fabrication techniques

Typically, the fabrication of homogeneous phantoms does not require any sophisticated manufacturing process. Molds of simple geometrical shapes are used to cast the phantom mixture. The mixture of the four basic components (scatterer, absorber, base, fluorophore) has to be thoroughly stirred to avoid any aggregation that may alter the optical properties. If the matrix material requires a stage of curing, a step of degassing may also be required. Because of the increasing demand for more complex phantoms, 3D phantom printing [67] has also emerged. 3D printing has the advantage of fast fabrication tailored to the complex geometry design demands of tissue-simulating phantoms. Therefore, it has become increasingly popular.

2.4 Comprehensive Phantoms

The development of standardization phantoms is an answer to the undisputable demand for the calibration and benchmarking of FI systems. This type of phantom needs to a) offer long-term photostability, regardless of the environmental conditions, and b) maintain its shape over time. The first requirement usually can be met with the use of QDs as a fluorescence agent because they do not suffer from photobleaching. The second requirement can be met with the use of specific matrix materials (e.g., polyester, polyurethane) that result in rigid phantoms.

Several camera system specifications, such as sensitivity and dynamic range, can be assessed with standardization phantoms. For example, the sensitivity of fluorescence camera systems has been interrogated with a polyurethane-based phantom with wells of varying quantities of NIR QDs [35]. The camera sensitivity has been assessed from the photon counts of the fluorescence image of the wells. Another important specification is the light leakage assessment, referring to the backscattered excitation light that passes through the filters or parasitic light from the environment into the fluorescence channel. For the light leakage interrogation, a solid phantom consisting of QDs in polyurethane solution that was sprayed onto a reflective surface has been used [34]. The dynamic range characteristic of the camera has also been interrogated [34],[68]. Furthermore, the imaging quality with respect to depth is also a fluorescence parameter that has been addressed by fully submerging fluorescence thin tubes [62].

There is a need for the aforementioned specifications and even more to be interrogated simultaneously so that the trade-off among them is evident. Parameters such as the illumination homogeneity, resolution, dependency of fluorescence intensity on tissue optical properties, and depth should be addressed comprehensively in the phantom. Consequently, there is a requirement for a new class of phantoms that enables the measurement of multiple parameters. The development of a comprehensive phantom that tests multiple parameters simultaneously using a single snapshot or very few images is a necessary advance for the comparison of different systems and operational parameters.

Toward this end, we designed and developed comprehensive solid polyurethane phantoms that can assess multiple system parameters simultaneously, such as the camera sensitivity, fluorescence intensity variations as a function of optical properties and depth, illumination homogeneity, resolution, and cross talk from excitation light leaking into the fluorescence channel.

2.4.1 Phantom description

The first developed standardization phantom [69] is made of polyurethane, with $10 \times 10 \times 2.2 \text{ cm}^3$ dimensions, and it includes structural formations that assess different system specifications, as shown in Fig. 3a. For the background, alcohol soluble nigrosin and titanium dioxide (TiO_2) were used as absorbing and scattering agents, respectively. The rest of the structures have hemin instead of nigrosin as the absorbing agent. QDs at 800 nm emission were selected as the fluorescence agent because of the high photostability. Different structures were placed in each quadrant of the phantom for different assessments of the system. In the upper-right quadrant, an array of nine wells with varying absorption and scattering coefficients and varying fluorophore concentration is used to interrogate the sensitivity. In the lower-right quadrant, an array of nine wells with the same fluorescence concentration at varying depths is used to evaluate the relationship between fluorescence signal and depth. In the upper-left quadrant, one well with high scattering properties and another with high absorption was placed for the light leakage interrogation. The spatial resolution of the imaging systems is evaluated with the lower-left quadrant. For the spatial resolution of the fluorescent image, an L-shaped structure with fluorescence properties is used as the target. An estimation of the spatial optical resolution can be achieved by using a standard 1951 United States Air Force resolution test chart that was fixed in this quadrant on the phantom's surface. Finally, the light's illumination homogeneity is evaluated through five identical reflective wells on the phantom. Likewise, this illumination homogeneity information can also be used to correct inhomogeneous white light illumination.

The detailed phantom description and phantom specification interrogation can be found in Appendix A.

Fig. 3b shows a new and improved version of the phantoms [70] that is being developed with more substructures and a wider range of the main block scattering properties. The background has a higher amount of TiO₂ and less nigrosin than the previous version. Moreover, these phantoms include a structure to quantify the dynamic range and a five-spot structure to correct the acquired fluorescence inhomogeneity using the fluorescence snapshot of the phantom. The upper-right side (Fig. 3b) has a nine-well structure with different optical properties but the same amount of QDs and can also be used for testing algorithms of fluorescence intensity correction. The development of this novel class of multiparameter solid phantoms (both first- and second-generation) allows, for the first time, a comprehensive way to standardize fluorescence imaging systems.

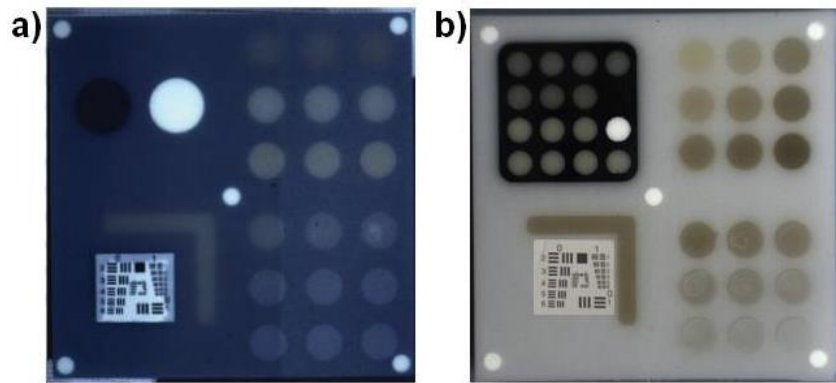


Figure 3: Developed phantoms. a) First generation of phantoms. **b)** Second generation of phantoms.

2.4.2 Phantom fabrication process

The fabrication process is similar for both versions of the phantom. The fabrication process for the second generation of phantoms is depicted in Fig. 4. This can be summarized in six steps. First, the mixture of the background material (polyurethane, TiO₂, nigrosin) is degassed and poured into a metallic square-shaped mold and is left to be cured for 24 hours (Fig. 4a). Second, the wells and structures are drilled on the cuboid with computer numerical control machining (Fig. 4b). Third, they are filled with specific amounts of hemin, TiO₂, and QDs (Fig. 4c). In the fourth step, after the first filling, the wells in the lower-right and upper-left structures are drilled (Fig. 4d) on the cured phantom of Fig. 4c. Fifth, the varying depths in the depth structure are filled with the background material mixture up to the surface, and the remaining unfilled wells are filled (Fig. 4e). Finally, the phantom is trimmed to remove the upper imperfect surface layers that contain bubbles (Fig. 4f).

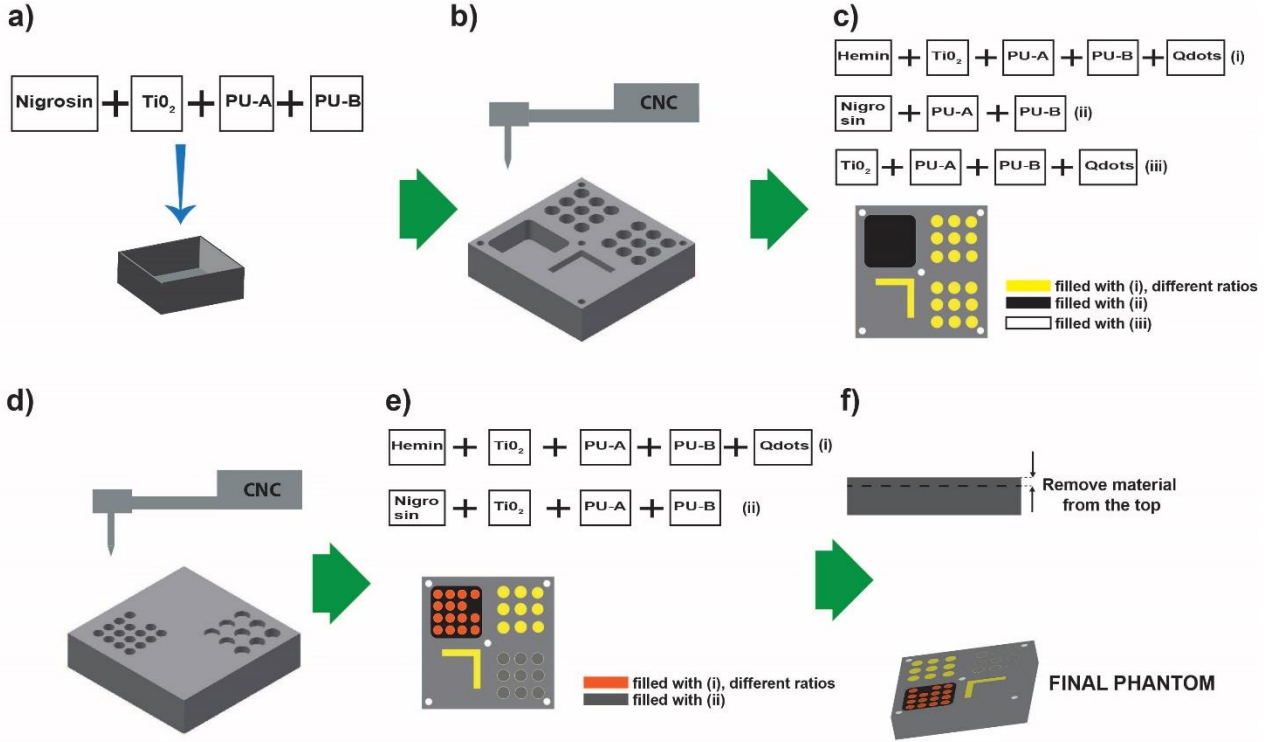


Figure 4: Phantom development process. **a)** The background mixture is filled in the mold. **b)** First drilling of the structures. **c)** First filling of the structure. **d)** Second drilling of the different depths and the rest of the wells. **e)** Second filling. **f)** Trimming of the final phantom piece.

2.4.3 Phantom optical properties characterization process

For the measurement of optical properties of the fabricated phantoms, it is assumed that used scattering and absorbing agents have minimal absorption and scattering, respectively [46]. Hence, the following procedure was performed: The absorption coefficient was measured using a spectrometer coupled to a fiber that collects the light that passed through a cuvette filled with the corresponding absorbing agent (Fig. 5a). Then, a homogeneous slab of a specific thickness that was composed of the exact phantom materials was made. The steady-state spatially resolved transmittance profile of a point-like source through the slab was recorded with a CCD camera (Fig. 5b). A continuous laser was used for the transillumination of the slab and fiber with a small core size so that a point source could be approximated. Monte Carlo simulations [71] with a fixed μ_a (measured μ_a) and a range of μ'_s values were performed (Fig. 5c), and the cost function between the measurement and simulation was calculated (Fig. 5d). Finally, the μ'_s value that minimized the cost function was selected, so both μ_a and μ'_s were retrieved.

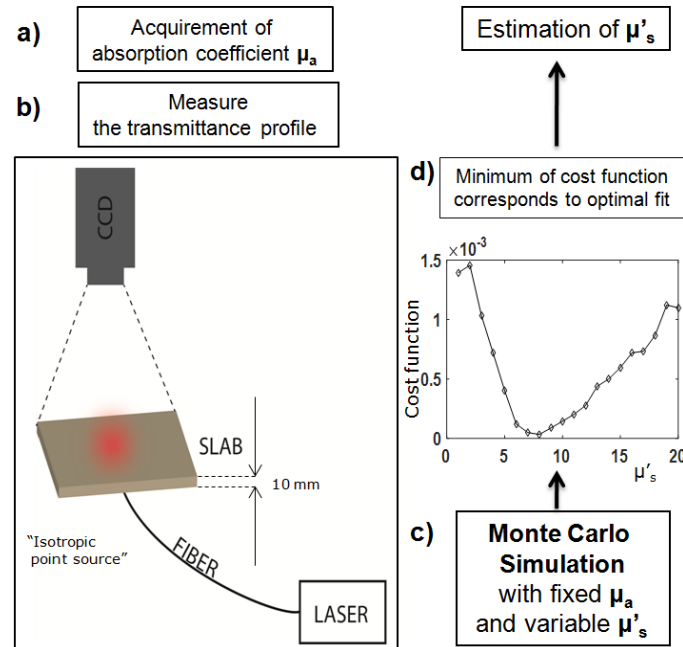


Figure 5: Procedure for phantom optical properties estimation. **a)** The absorption coefficient is acquired through a spectrophotometer. **b)** The spatially resolved transmittance profile from a point-like source through a slab is recorded. **c)** Monte Carlo simulations are performed with the measured μ_a and a range of μ'_s . **d)** The cost between the measured transmittance profile and the calculated Monte Carlo profile is calculated, and the μ'_s for which the cost is minimized is selected.

2.4.4 Discussion

Herein, a standardization phantom that can serve as a comprehensive tool assessing a system's performance and comparing systems with different specifications is shown. By applying cross sections to the entities of the fluorescence image (Fig. 6a), a first impression of parameters performance can be shown. For example, the performance of camera systems regarding depth-related fluorescence signal differences can be examined through the nine-well depth entity on the phantom (Fig. 6b) using the fluorescence signal plot versus the depth (Fig. 6d). Moreover, the 3D profile of the five reflective spots can be used to render a 3D surface that approximates the illumination field and can be used for flat field correction (Fig. 6c). Finally, such phantoms could also be used for system benchmarking automatically and even for correcting the acquired data [70].

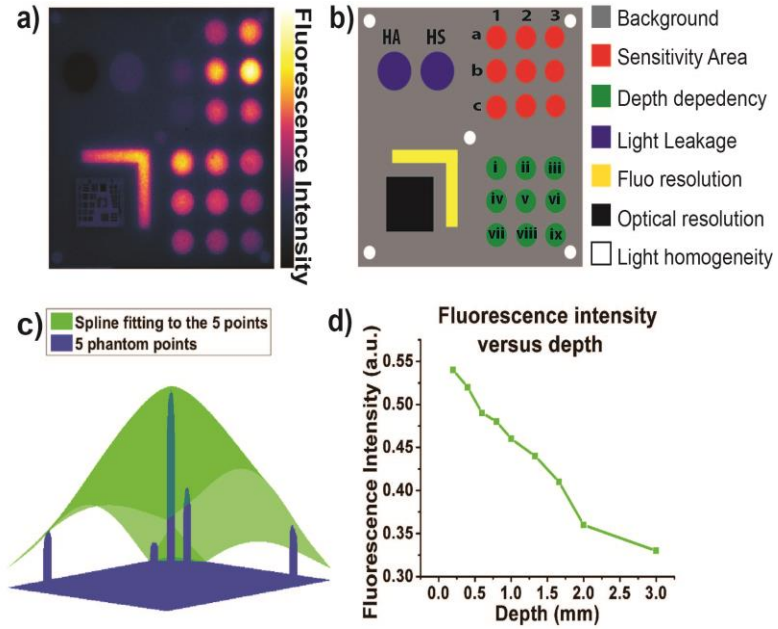


Figure 6: Phantom areas demonstration. **a)** Fluorescence image of the phantom. **b)** Schematic of the phantom where HA is the high-absorbing area and HS is the high-scattering area. 1->3: increasing fluorescence and absorption. a->c: increasing scattering. i to ix: increasing depth from the surface. **c)** Rendered profile from the five identical reflective spots. **d)** Fluorescence intensity versus depth from the depth dependency section. Adapted from [72].

3. Fluorescence Imaging (FI) Enhancement

3.1 Optical Properties of Tissue

The interaction of light with the tissue depends on the features of the illumination and, most critically, on the optical properties of the tissue. These properties control how the light will propagate through the material and whether the photons will be scattered or absorbed. The tissue's optical properties can be described by the following parameters:

- a) The absorption coefficient μ_a (commonly given in cm^{-1} units), which accounts for the probability that an incident photon is absorbed after an infinitesimal distance
- b) The scattering coefficient μ_s (commonly given in cm^{-1} units), which accounts for the probability that an incident photon is scattered after an infinitesimal distance; the reduced scattering coefficient is defined as $\mu'_s = \mu_s(1-g)$, where g is the average cosine of the scattering angle, describing the isotropic scattering equivalent of a photon undergoing multiple scattering events
- c) The scattering function p (in sr^{-1} units), which describes the angular-dependent scattering of an incident photon
- d) The real refractive index of the tissue n (dimensionless)

3.1.1 Optical properties as tissue biomarkers

The differentiation in tissue optical properties has been employed as a contrast mechanism and disease biomarker [73], as in the case of the distinction between malignant and benign breast tissues [74]. Likewise, it has been shown that important information regarding tissue oxygenation, or the presence of malignant tissue, can be inferred by monitoring the absorption of hemoglobin. The absorption coefficient of hemoglobin, the protein that transports oxygen, depends on oxygen saturation. Cancerous breast tissue has shown higher hemoglobin concentration, as long as higher scattering and refractive index increase in comparison to healthy breast tissue [75],[76]. Encouraging results have also been shown to differentiate colon cancer [77] and nerves [78] from other tissues.

3.1.2 Absorption and scattering as a fluorescence signal distortion factor

The scattering and absorption phenomena in tissue distort the fluorescence signal in FI. The aim of FI is to provide accurate localization of the specific fluorescence signal, which respectively means accurate localization of the diseased tissue. Ideally, the signal should be dependent only on the concentration of the fluorophore and disentangled from optical properties

variation. However, scattering and absorption in tissue affect the spatial quantification of the amount of fluorophore from the recorded images. Moreover, the fluorescence image appears blurred due to photon diffusion. Therefore, the main aim is to decouple the signal from the effects of the optical properties.

3.2 Resolution and Contrast Correction

Scattering and absorption of light in turbid biological tissue limit the image fidelity and result in degraded fluorescence images. Low image quality leads to misinterpretation of the fluorescence distribution in the tissue, which is crucial in both medical practice and research [79], [80]. Concerning medical practice, in tumor resection surgeries, a blurry fluorescence image can impair the surgeon's decision-making regarding the proper tumor margins. This can greatly affect on a patient's sequential treatment and overall life quality. In addition to clinical applications, high-fidelity—or high-spatial-resolution—images are required in cryo-imaging [81] to provide information about the biodistribution of fluorescence agents [82]. Consequently, new methods that can sufficiently address the aforementioned issues are needed.

3.2.1 Methods for enhancing the resolution in FI

Different imaging strategies have been proposed to tackle the fluorescence signal degradation caused by light interaction with tissue. Usually in fluorescence microscopy, tissue slices are sufficiently thin to minimize scattering effects. Thus, the image degradation mainly emanates from the optical system aberrations and diffraction instead of the scattering and absorption. Even though the cause is different, the distortion can confer a similar effect on the appearance of the acquired image. To overcome these system limitations and the diffraction limit, there is an exhaustive list of techniques in microscopy before, during, and after image acquisition for enhancing image quality [83]. Stimulated emission depletion microscopy, saturated structured-illumination microscopy, photoactivated localization microscopy, fluorescence photoactivation localization microscopy, and stochastic optical reconstruction microscopy are a few [84] to mention. These techniques aim to enhance the optical resolution of the system, which is limited by diffraction, optical system aberrations, and wavelength.

Unlike fluorescence microscopy, there is a lack of approaches that successfully address image distortion in wide-field fluorescence imaging of turbid tissues. Optical clearing [85], [86] is a chemical method that augments tissue transparency to increase the resolution and depth of penetration. However, this is only applied to ex vivo tissues. Another method that has made

progress is spatial frequency domain imaging [87],[88], but the correction is applied on a pixel-to-pixel basis, and spatial dependencies on the image are ignored.

Herein, a novel approach is presented that is based on the post-processing of the acquired imaging data from a typical NIR interventional system. The reasoning behind this approach is to gather information related to optical properties from the area of interest and later use this information in a post-processing algorithm to increase the resolution and enhance the quality of the fluorescence image (Section 3.3). In Appendix B, the implementation of the diffusion correction through a spatially variant deconvolution regime is described in detail, being tested in phantoms and ex vivo mice. There is a second approach to achieve fluorescence image enhancement that has an entirely different philosophy. Instead of post-processing the images, the wavelength for image acquisition is shifted toward the SWIR range. This suggests the use of entirely different camera imaging systems, optics, sensors, filters, etc. In Section 3.4, SWIR imaging with potential advantages and drawbacks is discussed.

3.3 Fluorescence Diffusion Correction Through a Spatially Variant Deconvolution Scheme

A standard image processing technique for image restoration is deconvolution. An acquired blurry image is considered the result of a convolution of an ideal highly resolved image with a degradation kernel. That convolution process needs to be reverted to retrieve the ideal image from the captured blurry image. This can be done through deconvolution, which has been effectively used in various applications such as astronomy [89], computer vision [90], and wide-field fluorescence microscopy [91]. Typically, the degradation kernel is space and time invariant and depends on the imperfections of the imaging system configuration. Although deconvolution is a broadly used technique for image restoration, it has been employed only in very specific preclinical fluorescence imaging applications [92] but not in clinical ones. The main reason is that the degradation in clinical fluorescence images is not a result of the limitations of the acquisition device but mainly depends on the optical properties of the tissue. Thus, the deconvolution kernel changes every time a new sample is imaged, and the retrieval of the system's point spread function does not seem particularly useful. Consistent results can be achieved by using particular parameters specific for each tissue [93]. Typically, a spatially invariant kernel is used in deconvolution operations. A fixed kernel implies the underlying hypothesis for shift invariance of the tissue optical properties. Because tissues are also heterogeneous, the diffuse-measured fluorescence signal varies spatially in the sample due to

variations in local tissue optical properties. Consequently, there is a need for a spatially variant deconvolution process to correct the optical diffusion caused by scattering in inhomogeneous tissues.

The main challenges of performing a spatially variant deconvolution scheme are a) the acquisition of the proper degradation kernels, b) the selection of an appropriate deconvolution algorithm that will not result in enhancing the noise and artifacts, and c) the computational efficiency of the method so that it can be executed quickly.

Herein, a novel deconvolution framework for enhancing biological fluorescence images degraded by light diffusion using spatially variant kernels is presented. By illuminating each tissue area sequentially with a point-like source from a digital light processing (DLP) projector and capturing the spatially diffused reflectance (SDR), we acquire spatially varying kernels for the entire imaging area. After a binning process, these kernels are used in a modified fast Lucy-Richardson algorithm with total variation regularization [94], and the final corrected image is assembled.

3.3.1 Method description

The raw acquired fluorescence image is considered the result of a convolution operation of the ground truth fluorescence image with a kernel dependent upon the optical properties of the imaging area. The distortion introduced by the optical imaging system is considered negligible compared to the diffusion effect by the light–tissue interactions. To take into account the spatial variation in tissue optical properties, a different kernel for each point of the entire scanned region instead of a global one shall be applied. Because an image is represented as a discrete two-dimensional array, the convolution operation is defined as the following:

$$I_s(x, y) = \sum \sum I_{gt}(x-u, y-v) K(u, v, x, y) dudv \quad (1)$$

where I_s is the measured raw fluorescence image, I_{gt} is the ground truth fluorescence image that we want to retrieve, and K is the variant degradation kernel. A point-like source is projected on the sample by a DLP device, and the diffuse reflectance is acquired by a CCD camera, as shown in Fig. 7a. Then the kernel is fitted to a two-dimensional Gaussian curve, and the sigma value (standard deviation) is retrieved. The entire area of interest is sequentially scanned by this point-like source, and a sigma map (Fig. 7b) for the whole area is assembled. As a result, a

sigma value is assigned to each image pixel. The sigma values are corrected for uneven light distribution and projector system characteristics.

Because a per-pixel deconvolution step would be computationally exhaustive, the sigma values are binned into n equally sized bins (Fig. 7b), and the lowest sigma value of every bin is used to generate a new Gaussian kernel. This kernel is used in a Lucy-Richardson iterative restoration method, using a regularization constraint based on total variation to suppress the noise [94]. After m cycles of iterations for each deconvolution with the captured fluorescence raw image (Fig. 7c), the results are weighted such that the contribution of each deconvolution to a designated pixel is higher when the sigma value of this pixel is closer to the sigma value of the used kernel for this deconvolution result. Finally, the corrected fluorescence image is assembled (Fig. 7d).

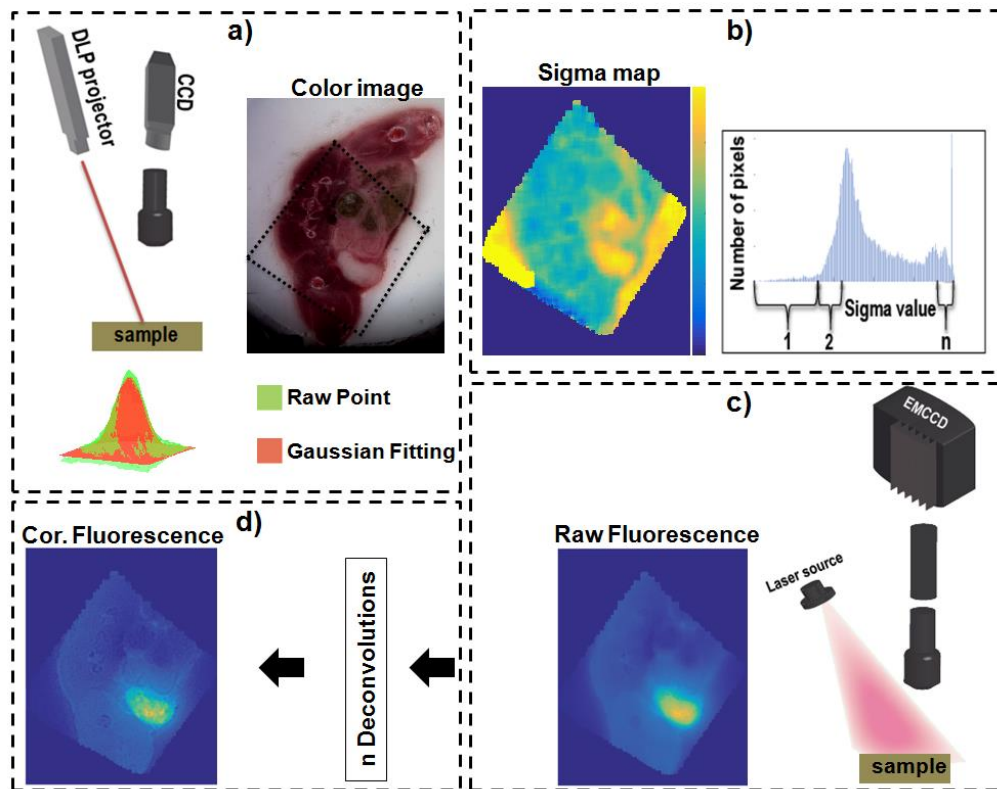


Figure 7: Spatially variant deconvolution scheme. **a)** Raster scanning with the DLP projector of a region of interest from a cryo-sliced mouse bearing HCT116 tumor model expressing iRFP720 and fitting of the reflectance kernels to Gaussian kernels. **b)** Sigma map acquisition from the Gaussian kernel fitting and binning of the sigma values into n bins. **c)** Acquisition of the fluorescence image. **d)** The final corrected fluorescence image after n number of deconvolutions and weighting of the results.

3.3.2 Discussion

The proposed method was evaluated and validated by imaging phantoms and cryo-sections of mice bearing tumors expressing NIR fluorescent proteins or mice bearing tumors injected with tumor-targeting fluorescence agents (Appendix B). For instance, Fig. 8 shows the diffusion correction method for two mice bearing different tumor models. The first mouse (see Fig. 8a) bears a KPL-4 tumor and has been injected with Integrinsense 750. The corrected image appears more resolved, and details of the tumor topology are revealed. This can be seen by comparing uncorrected (Fig. 8b) and corrected (Fig. 8c) images. For the second mouse (Fig. 8d), with the 4T1 tumor model that is expressing iRFP720, the corrected image in Fig. 8f also appears more resolved than the uncorrected one in Fig. 8e.

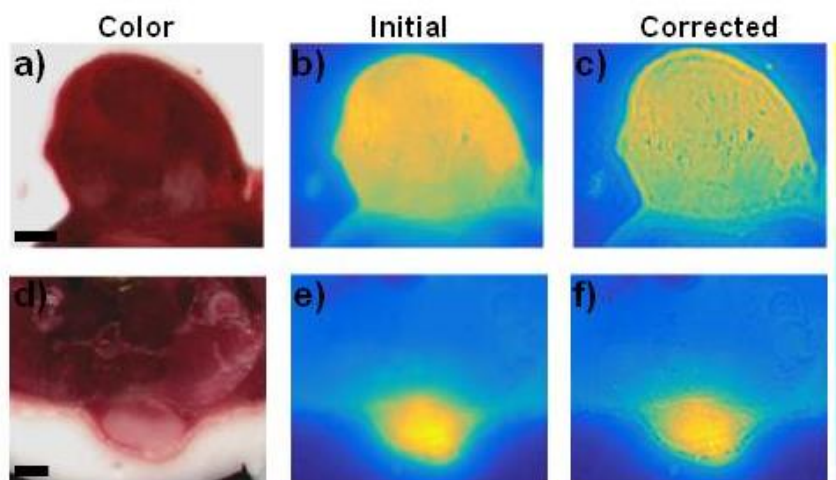


Figure 8: Correction of fluorescence images of mice bearing tumors. a) Color image of mouse containing a KPL-4 tumor injected with Integrinsense 750. b) Raw fluorescence image of a). c) Corrected fluorescence image of b). d) Color image of a mouse bearing a 4T1 tumor expressing iRFP720. e) Raw fluorescence image of d). f) Corrected fluorescence image e). Scalebar: 1 mm.

Our method has the flexibility to be used with different fluorescence agents, types of tissues, and combinations of imaging systems. Better tumor demarcation and tumor topology observation can be achieved by using the information acquired from the scanning with a fast spatially variant deconvolution algorithm, which is crucial for clinical decision-making. For a translation of this method into the clinical environment, real-time correction and visualization are required. Toward this goal, faster scanning with a grid of points, instead of single-point scanning, was implemented. Moreover, the DLP projector was upgraded so that different laser sources could be coupled. The current system is being continuously improved for better quality (e.g., the addition of crossed polarizers) and faster acquisition. Overall, the application of our

method into preclinical and clinical imaging setups can enhance the quality of fluorescence imaging.

3.4 SWIR Imaging

An entirely different approach to enhance FMI is imaging in the SWIR window, also known as NIR-II [95],[96], which lies in the range of 1000–1700 nm, instead of in the NIR window. SWIR fluorescence imaging has demonstrated the ability to provide higher resolution than NIR because of the significantly lower scattering in tissue at higher wavelengths [97]. Because silicon sensors cannot detect wavelengths longer than 1000 nm, different sensor materials are required, such as indium gallium arsenide and mercury cadmium telluride. This entails the use of different camera systems over conventional NIR systems, which can be costly. The image detection at higher wavelengths than NIR also suggests that fluorescence agents with emission peaks in the SWIR region are required. Hence, this new regime has prompted the advent of fluorescence agents whose emission peak lies in the SWIR spectral range, such as single-walled carbon nanotubes [98], [99], rare-earth-doped nanoparticles [100], QDs [101],[102], and small organic molecule dyes [103]. Despite their outstanding performance, none of these fluorescence probes has been translated to clinical studies because of limited clinical trials to ensure patients' safety regarding toxicity and tissue clearance. To overcome this burden, researchers have been investigating the potential of the already approved and commercially available NIR dyes to be used as contrast agents in SWIR. The potential of accessible, well-established, and characterized fluorophores in SWIR such as indocyanine green (ICG), IRDye 800CW, and methylene blue has already been demonstrated [104]. Specifically, the use of ICG in SWIR imaging has recently been explored [105],[106], and the potential of SWIR imaging with ICG was shown in mice [106], large animals [107], and humans [108]. The use of ICG in SWIR regimes is of critical importance because it can accelerate and facilitate the entrance of SWIR imaging into the clinic.

Despite these recent advances, it remains unclear under what conditions and for which applications SWIR truly outperforms NIR imaging concerning clinical needs for surgical guidance and early cancer detection. The realistic potential benefits of SWIR imaging, compared to NIR, must be better understood and studied before it transitions to the clinic. The effect of the depth of the imaged structure concerning clinically relevant parameters needs to be investigated for both regimes, and the trade-off among these clinical parameters needs to be

elucidated. Therefore, an investigation with phantom, ex vivo, and in vivo experiments is currently being undertaken.

Toward this goal, capillaries with ICG diluted in blood were placed under a different number of ex vivo pork slices to evaluate the effect of depth on the resolution and signal-to-noise ratio (SNR) of the fluorescence signal (Fig. 9). As can be seen from Fig. 9c and Fig. 9d, even though the resolution for 1100 long pass (LP) and 1200 LP filter in the SWIR regime is better than 810/90 band pass (BP) filter in the NIR regime, the SNR value is decaying faster in the SWIR region. This trade-off between SNR and resolution among the imaging bands suggests that the selection of imaging regime and emission wavelengths should be made according to the need of the specific clinical application.

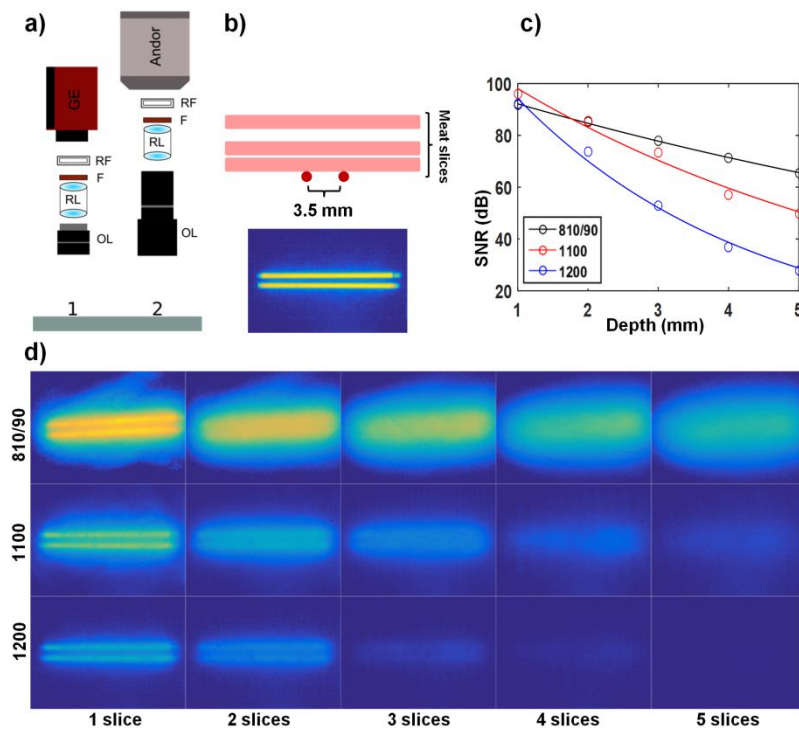


Figure 9: Comparison of SWIR versus NIR imaging of capillaries under a different number of pork slices. a) SWIR and NIR imaging system schematic. **b)** Two capillaries filled with ICG dissolved in blood are placed under pork slices of 1mm each. **c)** SNR in dB for different depths of the capillaries and different emission wavelengths. **d)** Fluorescence images of the capillaries under a different number of slices for NIR (810/90 BP filter) and for SWIR (1100 LP and 1200 LP filter). OL: Objective lens, RL: Relay lens, F: Fixed position filter, RF: Removable filter.

3.5 Fluorescence Intensity Disengagement from Optical Properties

One of the main challenges of FI is the signal intensity degradation due to scattering and absorption that affect the fluorescence intensity in a nonlinear way. A variety of techniques have been developed in an attempt to restore the signal intensity. The main step to reverse the fluorescence intensity is to capture, through measurement, information from the tissue sample relevant to the optical characteristics (e.g., optical properties, reflectance images) and to use this information in an empirical or theoretical formula to estimate the true fluorescence intensity [109]–[111]. Researchers have been trying to tackle this issue by applying a vast number of different approaches [112] from empirical to theoretical techniques. However, each technique has limitations, such as a trade-off between accuracy and a limited range of optical properties, certain limiting conditions, long computational times, and impracticality in an operation room. Furthermore, the dependence of the fluorescence signal both on the excitation and emission light exacerbates the ambiguity of a method's effectiveness and result interpretation. Overall, even if accuracy could be achieved in a phantom intensity correction method, the translation into the clinical environment is not straightforward. The need for approximations, the limited range of optical properties for which the method is reliable, the low SNRs, the tissue homogeneity hypothesis, and the time-consuming correction process are some of the limitations for clinical translation. Therefore, the quest to find an appropriate method for intensity correction remains an open challenge.

3.5.1 Requirements for a new method

Toward this direction, an ideal technique shall have the following characteristics:

- Is applicable for a wide range of optical properties
- Takes into account the tissue inhomogeneity
- Can be implemented simply
- Can be combined with a resolution correction method
- Operates in real time (>10 fps)
- Has an intensity correction that can be uniquely reversed [113]

An approach toward the development of a method that reflects as many of these characteristics as possible is to use the captured SDR from the projected point on the tissue as a means of diffusion correction and resolution enhancement (Section 3.3) and to correct the intensity values. The capture of SDR has been used in the literature to obtain optical properties using radiative transport equation for semi-infinite medium [114], a diffusion model [115]–[117], [118] or Monte Carlo simulation [119]. A look-up table can be constructed to accelerate and simplify the

retrieval of the optical properties [120],[121]. A feasible correction of fluorescence intensity can be possible by introducing the estimated optical properties in an empirical formula [110] that includes the raw fluorescence and reflectance [122],[87] as an additional correction to the previously described method (Section 3.3, Appendix B).

4. Conclusion and Future Outlook: Toward a New Framework

Despite the tremendous progress of FI, there are still some challenges (Section 1.3) to be addressed before FI is efficient enough to be used in surgical guidance applications.

The large number of FI systems at different locations working under different conditions and parameters has made system benchmarking and calibration imperative. Toward this aim, two generations of comprehensive solid phantoms were developed for the simultaneous assessment of several system parameters such as camera sensitivity, fluorescence intensity variations as a function of optical properties and depth, illumination homogeneity, resolution, and cross talk from excitation light leaking into the fluorescence channel. Moreover, it has been shown that the phantoms could also be used for illumination inhomogeneity correction for the color [69] and fluorescence [70] channel.

Currently, the wavelength of QDs and optical properties of the phantoms are being tailored to address more specific requirements for certain applications across laboratories. In the future, phantoms of a miniature size will also be developed to evaluate systems that have small FOVs so that no raster scanning and multiple image acquisitions of the phantom are needed. Overall, it is anticipated that our new class of phantoms and benchmarking methodology will be universally adopted across laboratories.

Moreover, a novel method for enhancing the resolution and contrast of fluorescence images that takes into account the tissue heterogeneity through the SDR kernel and a spatially variant deconvolution scheme was shown. Apart from the resolution and contrast correction, this method with some added steps has the potential to be used for the correction of the fluorescence intensity signal in a quantitative fashion. The information from SDR along with information from the reflectance images at excitation and emission wavelength could be used for the correction of the fluorescence image to account for the fluorophore spatial concentration. Then the final image can be corrected both in terms of a pixel-to-pixel intensity correction and neighbor pixel diffusion correction. The current focus is on an add-on intensity correction method, from the information that is retrieved from the scanning that should comply with the requirements for a new correction method, as mentioned above.

Currently, we are working toward optimizing and accelerating the acquisition of the kernels. A high-resolution projector that can be coupled to different laser sources is used, crossed linear polarizers are used to reduce reflections, etc. The scanning is being done not by a single point, but by a grid of points, which significantly reduces the scanning time. Furthermore, the fitting

processing is being optimized to operate in a parallel rather than serial regime. As a more advanced step, to accurately estimate the fluorescence agent uptake by tumorous tissue, our method could be combined with a dual tracer method [123],[124], where a targeted and a nontargeted tracer is used.

Overall, we envision the development of a new framework for FI enhancement that will include the already described methods with ongoing and future improvements and additions. Such a potential framework is demonstrated in Fig. 10. Initially, in Fig. 10a, our standardization phantom is used to calibrate the system and adjust the optimized parameters before the fluorescence image acquisition of the sample. The phantom fluorescence image that is acquired is used, as mentioned before, to correct for illumination inhomogeneity. Then, the sample/tissue is placed in the FOV of the camera system, and the scanning procedure with a grid of points that are projected using a laser with the excitation wavelength (Fig. 10bi) takes place. After that, reflectance images of the excitation (Fig. 10bii) and emission (Fig. 10biii) wavelengths are recorded. Finally, the initial uncorrected fluorescence image (Fig. 10biv) is captured after placing the corresponding emission filter in the optical path. In the last step, the information that has been recorded is used in such a way (Fig. 10c) that the final corrected image is formed. Even though the imaging data acquisitions in Fig. 10 are depicted in a serial way, they can be achieved in parallel with the right system configuration with multiple cameras and beamsplitters. Nevertheless, the major limitation of this framework is speed. Therefore, faster scanning and processing methods need to be developed and implemented so it is feasible in the future to be translated into a clinical environment.

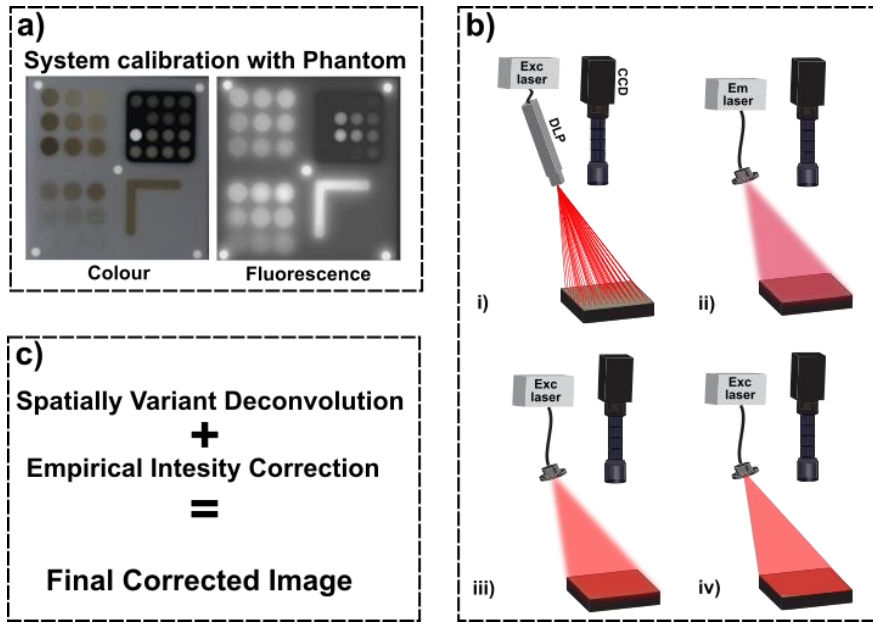


Figure 10: Toward a comprehensive method for fluorescence correction. **a)** Use of the solid phantom for system calibration and correction of illumination inhomogeneity. **b)** For the tissue ROI: i) Scanning with a grid of points for fast spatially resolved kernel retrieval. ii) Acquisition of reflectance image at the emission wavelength. iii) Acquisition of reflectance image at the excitation wavelength. iv) Acquisition of fluorescence image (emission filter F is placed in the light path). **c)** Use of the information acquired from b) to improve the resolution and intensity to get a final corrected image.

5. References

- [1] H. C. Burkholder, L. E. Witherspoon, R. P. Burns, J. S. Horn, and M. D. Biderman, "Breast surgery techniques: Preoperative bracketing wire localization by surgeons," *Am. Surg.*, vol. 73, no. 6, pp. 574–578, 2007, doi: 10.1177/000313480707300608.
- [2] R. G. Pleijhuis, M. Graafland, J. De Vries, J. Bart, J. S. De Jong, and G. M. Van Dam, "Obtaining adequate surgical margins in breast-conserving therapy for patients with early-stage breast cancer: Current modalities and future directions," *Ann. Surg. Oncol.*, vol. 16, no. 10, pp. 2717–2730, 2009, doi: 10.1245/s10434-009-0609-z.
- [3] S. Chondrogiannis *et al.*, "Intraoperative hand-held imaging γ -camera for sentinel node detection in patients with breast cancer: Feasibility evaluation and preliminary experience on 16 patients," *Clin. Nucl. Med.*, vol. 38, no. 3, 2013, doi: 10.1097/RLU.0b013e31827a278d.
- [4] V. Ntziachristos, "Fluorescence Molecular Imaging," *Annu. Rev. Biomed. Eng.*, vol. 8, no. 1, pp. 1–33, 2006, doi: 10.1146/annurev.bioeng.8.061505.095831.
- [5] M. Koch and V. Ntziachristos, "Advancing Surgical Vision with Fluorescence Imaging," *Annu. Rev. Med.*, vol. 67, no. 1, pp. 153–164, 2016, doi: 10.1146/annurev-med-051914-022043.
- [6] C. Chi *et al.*, "Intraoperative Imaging-Guided Cancer Surgery: From Current Fluorescence Molecular Imaging Methods to Future Multi-Modality Imaging Technology," *Theranostics*, vol. 4, no. 11, pp. 1072–1084, 2014, doi: 10.7150/thno.9899.
- [7] S. Sajedi, H. Sabet, and H. S. Choi, "Intraoperative biophotonic imaging systems for image-guided interventions," *Nanophotonics*, vol. 8, no. 1, pp. 99–116, Jan. 2019, doi: 10.1515/nanoph-2018-0134.
- [8] G. M. van Dam *et al.*, "Intraoperative tumor-specific fluorescence imaging in ovarian cancer by folate receptor- α targeting: first in-human results," *Nat. Med.*, vol. 17, no. 10, pp. 1315–1319, 2011, doi: 10.1038/nm.2472.
- [9] L. E. Lamberts *et al.*, "Tumor-specific uptake of fluorescent bevacizumab-IRDye800CW microdosing in patients with primary breast cancer: A phase I feasibility study," *Clin. Cancer Res.*, vol. 23, no. 11, pp. 2730–2741, 2017, doi: 10.1158/1078-0432.CCR-16-0437.
- [10] S. E. Miller *et al.*, "First-in-human intraoperative near-infrared fluorescence imaging of glioblastoma using cetuximab-IRDye800," *J. Neurooncol.*, vol. 139, no. 1, pp. 135–143, 2018, doi: 10.1007/s11060-018-2854-0.
- [11] P. Von Breitenbuch *et al.*, "Autofluorescent imaging in patients with peritoneal carcinomatosis," *Surg. Innov.*, vol. 21, no. 2, pp. 187–193, 2014, doi: 10.1177/1553350613495114.
- [12] O. Buchweitz, A. Staebler, J. Tio, and L. Kiesel, "Detection of peritoneal endometriotic lesions by autofluorescence laparoscopy," *Am. J. Obstet. Gynecol.*, vol. 195, no. 4, pp. 949–954, 2006, doi: 10.1016/j.ajog.2006.02.044.
- [13] G. W. Falk, "Autofluorescence Endoscopy," *Gastrointestinal Endoscopy Clinics of North America*, vol. 19, no. 2, pp. 209–220, 2009, doi: 10.1016/j.giec.2009.02.004.
- [14] M. A. McWade *et al.*, "Label-free intraoperative parathyroid localization with near-infrared

- autofluorescence imaging,” *J. Clin. Endocrinol. Metab.*, vol. 99, no. 12, pp. 4574–4580, 2014, doi: 10.1210/jc.2014-2503.
- [15] A. N. Di Marco and F. F. Palazzo, “Near-infrared autofluorescence in thyroid and parathyroid surgery,” *Gland Surgery*, vol. 9, pp. S136–S146, 2020, doi: 10.21037/gs.2020.01.04.
- [16] J. T. Alander *et al.*, “A Review of Indocyanine Green Fluorescent Imaging in Surgery,” *Int. J. Biomed. Imaging*, vol. 2012, pp. 1–26, 2012, doi: 10.1155/2012/940585.
- [17] M. B. Reinhart, C. R. Huntington, L. J. Blair, B. T. Heniford, and V. A. Augenstein, “Indocyanine Green :Historical Context, Current Applications, and Future Considerations,” *Surg. Innov.*, vol. 23, no. 2, pp. 166–175, 2016, doi: 10.1177/1553350615604053.
- [18] S. L. Troyan *et al.*, “The FLARE((TM)) Intraoperative Near-Infrared Fluorescence Imaging System: A First-in-Human Clinical Trial in Breast Cancer Sentinel Lymph Node Mapping,” *Ann. Surg. Oncol.*, vol. 16, no. 10, pp. 2943–2952, 2009, doi: Doi 10.1245/S10434-009-0594-2.
- [19] Y. Fujisawa, Y. Nakamura, Y. Kawachi, and F. Otsuka, “A custom-made, low-cost intraoperative fluorescence navigation system with indocyanine green for sentinel lymph node biopsy in skin cancer.,” *Dermatology*, vol. 222, no. 3, pp. 261–268, 2011, doi: 10.1159/000327080.
- [20] Y. Tajima *et al.*, “Sentinel node mapping guided by indocyanine green fluorescence imaging during laparoscopic surgery in gastric cancer,” *Ann. Surg. Oncol.*, vol. 17, no. 7, pp. 1787–1793, 2010, doi: 10.1245/s10434-010-0944-0.
- [21] M. Chu and Y. Wan, “Sentinel lymph node mapping using near-infrared fluorescent methylene blue.,” *J. Biosci. Bioeng.*, vol. 107, no. 4, pp. 455–9, 2009, doi: 10.1016/j.jbiosc.2008.11.011.
- [22] A. Nour, “Efficacy of methylene blue dye in localization of sentinel lymph node in breast cancer patients.,” *Breast J.*, vol. 10, no. 5, pp. 388–91, 2004, doi: 10.1111/j.1075-122X.2004.21360.x.
- [23] D. Hanahan and R. A. Weinberg, “Hallmarks of cancer: the next generation.,” *Cell*, vol. 144, no. 5, pp. 646–74, 2011, doi: 10.1016/j.cell.2011.02.013.
- [24] W. Stummer, A. Novotny, H. Stepp, C. Goetz, K. Bise, and H. J. Reulen, “Fluorescence-guided resection of glioblastoma multiforme utilizing 5-ALA-induced porphyrins: a prospective study in 52 consecutive patients,” <http://dx.doi.org/10.3171/jns.2000.93.6.1003>, vol. 93, no. 6, pp. 1003–1013, 2000, doi: 10.3171/jns.2000.93.6.1003.
- [25] S. Esteves, M. Alves, M. Castel-Branco, and W. Stummer, “A pilot cost-effectiveness analysis of treatments in newly diagnosed high-grade gliomas: The example of 5-aminolevulinic acid compared with white-light surgery,” *Neurosurgery*, vol. 76, no. 5, pp. 552–562, 2015, doi: 10.1227/NEU.0000000000000673.
- [26] W. Stummer *et al.*, “Predicting the ‘usefulness’ of 5-ALA-derived tumor fluorescence for fluorescence-guided resections in pediatric brain tumors: a European survey.,” *Acta Neurochir. (Wien).*, vol. 156, no. 12, pp. 2315–24, 2014, doi: 10.1007/s00701-014-2234-2.
- [27] L. M. Bernal García, J. M. Cabezudo Artero, M. Royano Sánchez, M. B. Marcelo

- Zamorano, and M. López Macías, "Fluorescence-guided resection with 5-aminolevulinic acid of meningeal sarcoma in a child," *Child's Nerv. Syst.*, vol. 31, no. 7, pp. 1177–1180, 2015, doi: 10.1007/s00381-015-2703-9.
- [28] M. B. Sturm *et al.*, "Targeted imaging of esophageal neoplasia with a fluorescently labeled peptide: First-in-human results," *Sci. Transl. Med.*, vol. 5, no. 184, p. 184ra61, 2013, doi: 10.1126/scitranslmed.3004733.
- [29] R. Atreya *et al.*, "In vivo imaging using fluorescent antibodies to tumor necrosis factor predicts therapeutic response in Crohn's disease," *Nat. Med.*, vol. 20, no. 3, pp. 313–318, 2014, doi: 10.1038/nm.3462.
- [30] W. Scheuer, G. M. van Dam, M. Dobosz, M. Schwaiger, and V. Ntziachristos, "Drug-Based Optical Agents: Infiltrating Clinics at Lower Risk," *Sci. Transl. Med.*, vol. 4, no. 134, pp. 134ps11-134ps11, 2012, doi: 10.1126/scitranslmed.3003572.
- [31] J. Y. K. Lee *et al.*, "Review of clinical trials in intraoperative molecular imaging during cancer surgery," *J. Biomed. Opt.*, vol. 24, no. 12, pp. 1–8, Dec. 2019, [Online]. Available: <https://doi.org/10.1117/1.JBO.24.12.120901>.
- [32] G. Themelis, J. S. Yoo, K.-S. Soh, R. Schulz, and V. Ntziachristos, "Real-time intraoperative fluorescence imaging system using light-absorption correction.," *J. Biomed. Opt.*, vol. 14, no. 6, p. 064012, 2014, doi: 10.1117/1.3259362.
- [33] J. S. D. Mieog *et al.*, "Novel intraoperative near-infrared fluorescence camera system for optical image-guided cancer surgery," *Mol. Imaging*, vol. 9, no. 4, pp. 223–231, 2010, doi: 10.2310/7290.2010.00014.
- [34] B. Zhu, I.-C. Tan, J. C. Rasmussen, and E. M. Sevick-Muraca, "Validating the sensitivity and performance of near-infrared fluorescence imaging and tomography devices using a novel solid phantom and measurement approach," *Technol. Cancer Res. Treat.*, vol. 11, no. 1, pp. 95–104, 2012, [Online]. Available: <http://www.ncbi.nlm.nih.gov/pubmed/22181335>.
- [35] B. Zhu, J. C. Rasmussen, and E. M. Sevick-Muraca, "A matter of collection and detection for intraoperative and noninvasive near-infrared fluorescence molecular imaging: to see or not to see?," *Med. Phys.*, vol. 41, no. 2, p. 022105, 2014, doi: 10.1118/1.4862514.
- [36] M. D. Jafari *et al.*, "The use of indocyanine green fluorescence to assess anastomotic perfusion during robotic assisted laparoscopic rectal surgery," *Surg. Endosc.*, vol. 27, no. 8, pp. 3003–3008, 2013, doi: 10.1007/s00464-013-2832-8.
- [37] P. B. Garcia-Allende *et al.*, "Towards clinically translatable NIR fluorescence molecular guidance for colonoscopy," *Biomed. Opt. Express*, vol. 5, no. 1, p. 78, 2014, doi: 10.1364/BOE.5.000078.
- [38] W. B. Nagengast *et al.*, "Near-infrared fluorescence molecular endoscopy detects dysplastic oesophageal lesions using topical and systemic tracer of vascular endothelial growth factor A," *Gut*, vol. 68, no. 1, pp. 7–10, 2019, doi: 10.1136/gutjnl-2017-314953.
- [39] P.-L. Hsiung *et al.*, "Detection of colonic dysplasia in vivo using a targeted heptapeptide and confocal microendoscopy.," *Nat. Med.*, vol. 14, no. 4, pp. 454–8, 2008, doi: 10.1038/nm1692.
- [40] B. W. Pogue and M. S. Patterson, "Review of tissue simulating phantoms for optical spectroscopy, imaging and dosimetry," *J. Biomed. Opt.*, vol. 11, no. 4, p. 041102, 2006,

doi: 10.1117/1.2335429.

- [41] E. Drakaki, S. Psycharakis, M. Makropoulou, and a. a. a. Serafetinides, "Optical properties and chromophore concentration measurements in tissue-like phantoms," *Opt. Commun.*, vol. 254, no. 1–3, pp. 40–51, 2005, doi: 10.1016/j.optcom.2005.05.013.
- [42] A. M. De Grand *et al.*, "Tissue-like phantoms for near-infrared fluorescence imaging system assessment and the training of surgeons.," *J. Biomed. Opt.*, vol. 11, no. 1, p. 014007, 2006, doi: 10.1117/1.2170579.
- [43] A. J. Welch and M. J. C. Van Gemert, *Optical-thermal response of laser-irradiated tissue*. 2011.
- [44] S. Leavesley and J. P. Robinson, "A calibrated tissue phantom for small animal fluorescence imaging," vol. 6870, no. 68700, pp. 68700C-68700C–5, 2008, doi: 10.1117/12.763125.
- [45] G. Wagnières *et al.*, "An optical phantom with tissue-like properties in the visible for use in PDT and fluorescence spectroscopy.," *Phys. Med. Biol.*, vol. 42, no. 7, pp. 1415–1426, 1997, doi: 10.1088/0031-9155/42/7/014.
- [46] T. Moffitt, Y.-C. Chen, and S. a Prah, "Preparation and characterization of polyurethane optical phantoms.," *J. Biomed. Opt.*, vol. 11, no. 4, p. 041103, 2006, doi: 10.1117/1.2240972.
- [47] I. Noiseux, M. Fortin, S. Leclair, J. Osouf, and O. Mermut, "Development of optical phantoms for use in fluorescence-based imaging," *Des. Perform. Valid. Phantoms Used Conjunction with Opt. Meas. Tissue II*, vol. 7567, p. 75670B, 2010, doi: 10.1117/12.841887.
- [48] M. L. Vernon, J. Freàchette, Y. Painchaud, S. Caron, and P. Beaudry, "Fabrication and characterization of a solid polyurethane phantom for optical imaging through scattering media," *Appl. Opt.*, vol. 38, no. 19, pp. 4247–4251, 1999, doi: 10.1364/ao.38.004247.
- [49] G. Lamouche *et al.*, "Review of tissue simulating phantoms with controllable optical, mechanical and structural properties for use in optical coherence tomography," *Biomed. Opt. Express*, vol. 3, no. 6, p. 1381, 2012, doi: 10.1364/BOE.3.001381.
- [50] P. P. Elastomer, B. Jo, L. M. Van Lerberghe, K. M. Motsegood, and D. J. Beebe, "Three-Dimensional Micro-Channel Fabrication in," vol. 9, no. 1, pp. 76–81, 2000.
- [51] G. J. Greening *et al.*, "Characterization of thin poly(dimethylsiloxane)-based tissue-simulating phantoms with tunable reduced scattering and absorption coefficients at visible and near-infrared wavelengths.," *J. Biomed. Opt.*, vol. 19, no. 11, p. 115002, 2014, doi: 10.1117/1.JBO.19.11.115002.
- [52] F. Ayers, A. Grant, D. Kuo, D. J. Cuccia, and A. J. Durkin, "Fabrication and characterization of silicone-based tissue phantoms with tunable optical properties in the visible and near infrared domain," *Proc. SPIE*, vol. 6870, pp. 07-1-7–9, 2008, doi: 10.1117/12.764969.
- [53] S. T. Flock, S. L. Jacques, B. C. Wilson, W. M. Star, and M. J. C. van Gemert, "Optical properties of intralipid: A phantom medium for light propagation studies," *Lasers Surg. Med.*, vol. 12, no. 5, pp. 510–519, 1992, doi: 10.1002/lsm.1900120510.
- [54] H. J. van Staveren, C. J. M. Moes, J. van Marie, S. A. Prah, and M. J. C. van Gemert, "Light scattering in Intralipid-10% in the wavelength range of 400–1100 nm," *Appl. Opt.*,

vol. 30, no. 31, p. 4507, 1991, doi: 10.1364/ao.30.004507.

- [55] T. Phantoms, P. Di Ninni, F. Martelli, and G. Zaccanti, "Intralipid: Towards a diffusive reference standard for optical," *Phys. Med. Biol.*, vol. 56, no. 2, 2011, doi: 10.1088/0031-9155/56/2/N01.
- [56] N. Bodenschatz *et al.*, "Surface layering properties of Intralipid phantoms," *Phys. Med. Biol.*, vol. 60, no. 3, pp. 1171–1183, 2015, doi: 10.1088/0031-9155/60/3/1171.
- [57] J. Baeten, M. Niedre, J. Dunham, and V. Ntziachristos, "Development of fluorescent materials for Diffuse Fluorescence Tomography standards and phantoms.," *Opt. Express*, vol. 15, no. 14, pp. 8681–8694, 2007, doi: 10.1364/OE.15.008681.
- [58] C. F. Bohren and D. R. Huffman, *Absorption and Scattering of Light by Small Particles*. 1998.
- [59] P. Naglič, Y. Zelinskyi, B. Likar, and M. Bürmen, "Determination of refractive index, size, and solid content of monodisperse polystyrene microsphere suspensions for the characterization of optical phantoms," *Biomed. Opt. Express*, vol. 11, no. 4, p. 1901, 2020, doi: 10.1364/boe.387619.
- [60] K. Vishwanath, W. Zhong, M. Close, and M.-A. Mycek, "Fluorescence quenching by polystyrene microspheres in UV-visible and NIR tissue-simulating phantoms.," *Opt. Express*, vol. 14, no. 17, pp. 7776–88, 2006, doi: 97668 [pii].
- [61] M. Wang, S. Shen, J. Yang, E. Dong, and R. Xu, "3D printing method for freeform fabrication of optical phantoms simulating heterogeneous biological tissue," *Prog. Biomed. Opt. Imaging - Proc. SPIE*, vol. 8945, p. 894509, 2014, doi: 10.1117/12.2041137.
- [62] M. Roy, A. Kim, F. Dadani, and B. C. Wilson, "Homogenized tissue phantoms for quantitative evaluation of subsurface fluorescence contrast.," *J. Biomed. Opt.*, vol. 16, no. 1, p. 016013, 2011, doi: 10.1117/1.3528646.
- [63] P. Di Ninni, F. Martelli, and G. Zaccanti, "The use of India ink in tissue-simulating phantoms.," *Opt. Express*, vol. 18, no. 26, pp. 26854–26865, 2010, doi: 10.1364/OE.18.026854.
- [64] U. Resch-Genger, M. Grabolle, S. Cavaliere-Jaricot, R. Nitschke, and T. Nann, "Quantum dots versus organic dyes as fluorescent labels," *Nat. Methods*, vol. 5, no. 9, pp. 763–775, 2008, doi: 10.1038/nmeth.1248.
- [65] X. Gao, L. Yang, J. A. Petros, F. F. Marshall, J. W. Simons, and S. Nie, "In vivo molecular and cellular imaging with quantum dots," *Curr. Opin. Biotechnol.*, vol. 16, no. 1, pp. 63–72, 2005, doi: 10.1016/j.copbio.2004.11.003.
- [66] A. P. Alivisatos, W. Gu, and C. Larabell, "Quantum Dots as Cellular Probes," *Annu. Rev. Biomed. Eng.*, vol. 7, no. 1, pp. 55–76, 2005, doi: 10.1146/annurev.bioeng.7.060804.100432.
- [67] J. I. Gear, C. Long, D. Rushforth, S. J. Chittenden, C. Cummings, and G. D. Flux, "Development of patient-specific molecular imaging phantoms using a 3D printer," *Med. Phys.*, vol. 082502, no. 41, pp. 2012–2015, 2014, doi: 10.1118/1.4887854.
- [68] B. Zhu, J. C. Rasmussen, Y. Lu, and E. M. Sevick-Muraca, "Reduction of excitation light leakage to improve near-infrared fluorescence imaging for tissue surface and deep tissue imaging.," *Med. Phys.*, vol. 37, no. 11, pp. 5961–5970, 2010, doi: 10.1118/1.3497153.

- [69] M. Anastasopoulou *et al.*, “Comprehensive phantom for interventional fluorescence molecular imaging,” *J. Biomed. Opt.*, vol. 21, no. 9, p. 091309, 2016, doi: 10.1117/1.jbo.21.9.091309.
- [70] D. Gorpas *et al.*, “Multi-Parametric Standardization of Fluorescence Imaging Systems Based on a Composite Phantom,” *IEEE Trans. Biomed. Eng.*, vol. 67, no. 1, pp. 185–192, 2020, doi: 10.1109/TBME.2019.2910733.
- [71] Q. Fang, “Mesh-based Monte Carlo method using fast ray-tracing in Plücker coordinates,” *Biomed. Opt. Express*, vol. 1, no. 1, p. 165, 2010, doi: 10.1364/boe.1.000165.
- [72] M. Anastasopoulou *et al.*, “Multiparameter solid phantom for fluorescence imaging standardization,” in *Proc. SPIE*, Jul. 2017, vol. 10411, doi: 10.1117/12.2286059.
- [73] Z. Wang, G. Popescu, K. V Tangella, and A. Balla, “Tissue refractive index as marker of disease,” *J. Biomed. Opt.*, vol. 16, no. 11, pp. 1–8, Nov. 2011, doi: 10.1117/1.3656732.
- [74] V. G. Peters, D. R. Wyman, M. S. Patterson, and G. L. Frank, “Optical properties of normal and diseased human breast tissues in the visible and near infrared,” *Phys. Med. Biol.*, vol. 35, no. 9, pp. 1317–1334, 1990, doi: 10.1088/0031-9155/35/9/010.
- [75] R. Choe *et al.*, “Differentiation of benign and malignant breast tumors by in-vivo three-dimensional parallel-plate diffuse optical tomography,” *J. Biomed. Opt.*, vol. 14, no. 2, p. 024020, 2009, doi: 10.1117/1.3103325.
- [76] P. Taroni *et al.*, “Non-invasive optical estimate of tissue composition to differentiate malignant from benign breast lesions: A pilot study,” *Sci. Rep.*, vol. 7, 2017, doi: 10.1038/srep40683.
- [77] G. C. Langhout *et al.*, “Differentiation of healthy and malignant tissue in colon cancer patients using optical spectroscopy: A tool for image-guided surgery,” *Lasers Surg. Med.*, vol. 47, no. 7, pp. 559–565, 2015, doi: 10.1002/lsm.22388.
- [78] A. J. R. Balthasar *et al.*, “Optical signature of nerve tissue—Exploratory ex vivo study comparing optical, histological, and molecular characteristics of different adipose and nerve tissues,” *Lasers Surg. Med.*, vol. 50, no. 9, pp. 948–960, 2018, doi: 10.1002/lsm.22938.
- [79] C. M. O’Kelly Priddy, V. A. Forte, and J. E. Lang, “The importance of surgical margins in breast cancer,” *Journal of Surgical Oncology*, vol. 113, no. 3, pp. 256–263, 2016, doi: 10.1002/jso.24047.
- [80] C. G. Ethun and K. A. Delman, “The importance of surgical margins in melanoma,” *Journal of Surgical Oncology*, vol. 113, no. 3, pp. 339–345, 2016, doi: 10.1002/jso.24111.
- [81] P. Symvoulidis, C. C. Perez, M. Schwaiger, V. Ntziachristos, and G. G. Westmeyer, “Serial sectioning and multispectral imaging system for versatile biomedical applications,” *2014 IEEE 11th Int. Symp. Biomed. Imaging*, pp. 890–893, 2014, doi: 10.1109/ISBI.2014.6868014.
- [82] N. Barapatre *et al.*, “Quantitative detection of drug dose and spatial distribution in the lung revealed by Cryoslicing Imaging,” *J. Pharm. Biomed. Anal.*, vol. 102, pp. 129–136, 2014, doi: 10.1016/j.jpba.2014.09.001.
- [83] L. Schermelleh, R. Heintzmann, and H. Leonhardt, “A guide to super-resolution fluorescence microscopy,” *Journal of Cell Biology*, vol. 190, no. 2, pp. 165–175, 2010, doi: 10.1083/jcb.201002018.

- [84] B. O. Leung and K. C. Chou, "Review of super - Resolution fluorescence microscopy for biology," *Applied Spectroscopy*, vol. 65, no. 9. pp. 967–980, 2011, doi: 10.1366/11-06398.
- [85] D. Zhu, K. V. Larin, Q. Luo, and V. V. Tuchin, "Recent progress in tissue optical clearing," *Laser Photonics Rev.*, vol. 7, no. 5, pp. 732–757, 2013, doi: 10.1002/lpor.201200056.
- [86] H. Hama *et al.*, "ScaleS: an optical clearing palette for biological imaging.," *Nat. Neurosci.*, vol. 18, no. 10, pp. 1518–29, 2015, doi: 10.1038/nn.4107.
- [87] M. Sibai, I. Veilleux, J. T. Elliot, F. Leblond, D. W. Roberts, and B. C. Wilson, "Quantitative fluorescence imaging enabled by spatial frequency domain optical-property mapping in the sub-diffusive regime for surgical guidance," in *SPIE*, 2015, vol. 9311, p. 93110C, doi: 10.1117/12.2080205.
- [88] J. Sun *et al.*, "Enhancing in vivo tumor boundary delineation with structured illumination fluorescence molecular imaging and spatial gradient mapping.," *J. Biomed. Opt.*, vol. 21, no. 8, p. 80502, 2016, doi: 10.1117/1.JBO.21.8.080502.
- [89] J. L. Starck, E. Pantin, and F. Murtagh, "Deconvolution in Astronomy: A Review," *Publ. Astron. Soc. Pacific*, vol. 114, pp. 1051–1069, 2002, doi: 10.1086/342606.
- [90] P. Ruiz, X. Zhou, J. Mateos, R. Molina, and A. K. Katsaggelos, "Variational Bayesian Blind Image Deconvolution: A review," *Digit. Signal Process.*, vol. 47, pp. 116–127, 2015, doi: 10.1016/j.dsp.2015.04.012.
- [91] J. G. McNally, T. Karpova, J. Cooper, and J. a Conchello, "Three-dimensional imaging by deconvolution microscopy.," *Methods*, vol. 19, no. 3, pp. 373–85, 1999, doi: 10.1006/meth.1999.0873.
- [92] G. Krishnamurthi, C. Y. Wang, G. Steyer, and D. L. Wilson, "Removal of subsurface fluorescence in cryo-imaging using deconvolution.," *Opt. Express*, vol. 18, no. 21, pp. 22324–22338, 2010, doi: 10.1364/OE.18.022324.
- [93] G. J. Steyer, D. Roy, O. Salvado, M. E. Stone, and D. L. Wilson, "Removal of out-of-plane fluorescence for single cell visualization and quantification in cryo-imaging," *Ann. Biomed. Eng.*, vol. 37, no. 8, pp. 1613–1628, 2009, doi: 10.1007/s10439-009-9726-x.
- [94] N. Dey *et al.*, "Richardson-Lucy algorithm with total variation regularization for 3D confocal microscope deconvolution," *Microsc. Res. Tech.*, vol. 69, no. 4, pp. 260–266, 2006, doi: 10.1002/jemt.20294.
- [95] R. H. Wilson, K. P. Nadeau, F. B. Jaworski, B. J. Tromberg, and A. J. Durkin, "Review of short-wave infrared spectroscopy and imaging methods for biological tissue characterization," *J. Biomed. Opt.*, 2015, doi: 10.1117/1.jbo.20.3.030901.
- [96] A. M. Smith, M. C. Mancini, and S. Nie, "Bioimaging: second window for in vivo imaging," *Nat. Nanotechnol.*, vol. 4, no. 11, pp. 710–711, 2009, doi: 10.1038/nnano.2009.326.
- [97] S. L. Jacques, "Optical Properties of Biological Tissues: A Review," *Phys. Med. Biol.*, vol. 58, no. 11, pp. R37-61, 2013, doi: 10.1088/0031-9155/58/11/R37.
- [98] G. Hong *et al.*, "Multifunctional in vivo vascular imaging using near-infrared II fluorescence," *Nat. Med.*, vol. 18, no. 12, pp. 1841–1846, 2012, doi: 10.1038/nm.2995.
- [99] J. T. Robinson, G. Hong, Y. Liang, B. Zhang, O. K. Yaghi, and H. Dai, "In vivo fluorescence imaging in the second near-infrared window with long circulating carbon

- nanotubes capable of ultrahigh tumor uptake,” *J. Am. Chem. Soc.*, vol. 134, no. 25, pp. 10664–10669, 2012, doi: 10.1021/ja303737a.
- [100] D. J. Naczynski *et al.*, “Rare-earth-doped biological composites as in vivo shortwave infrared reporters,” *Nat. Commun.*, vol. 4, 2013, doi: 10.1038/ncomms3199.
- [101] S. Xu, J. Cui, and L. Wang, “Recent developments of low-toxicity NIR II quantum dots for sensing and bioimaging,” *TrAC - Trends in Analytical Chemistry*, vol. 80, pp. 149–155, 2016, doi: 10.1016/j.trac.2015.07.017.
- [102] J. Pichaandi and F. C. J. M. Van Veggel, “Near-infrared emitting quantum dots: Recent progress on their synthesis and characterization,” *Coordination Chemistry Reviews*, vol. 263–264, no. 1, pp. 138–150, 2014, doi: 10.1016/j.ccr.2013.10.011.
- [103] A. L. Antaris *et al.*, “A small-molecule dye for NIR-II imaging,” *Nat. Mater.*, vol. 15, no. 2, pp. 235–242, 2016, doi: 10.1038/nmat4476.
- [104] B. K. Byrd *et al.*, “Characterizing short-wave infrared fluorescence of conventional near-infrared fluorophores,” *J. Biomed. Opt.*, vol. 24, no. 03, p. 1, 2019, doi: 10.1117/1.jbo.24.3.035004.
- [105] Z. Starosolski, R. Bhavane, K. B. Ghaghada, S. A. Vasudevan, A. Kaay, and A. Annapragada, “Indocyanine green fluorescence in second near-infrared (NIR-II) window,” *PLoS One*, vol. 12, no. 11, 2017, doi: 10.1371/journal.pone.0187563.
- [106] J. A. Carr *et al.*, “Shortwave infrared fluorescence imaging with the clinically approved near-infrared dye indocyanine green,” *Proc. Natl. Acad. Sci. U. S. A.*, vol. 115, no. 17, pp. 4465–4470, 2018, doi: 10.1073/pnas.1718917115.
- [107] B. K. Byrd *et al.*, “First experience imaging short-wave infrared fluorescence in a large animal: indocyanine green angiography of a pig brain,” *J. Biomed. Opt.*, vol. 24, no. 8, pp. 1–4, Aug. 2019, [Online]. Available: <https://doi.org/10.1117/1.JBO.24.8.080501>.
- [108] Z. Hu *et al.*, “First-in-human liver-tumour surgery guided by multispectral fluorescence imaging in the visible and near-infrared-I/II windows,” *Nat. Biomed. Eng.*, vol. 4, no. 3, pp. 259–271, 2020, doi: 10.1038/s41551-019-0494-0.
- [109] a. Bogaards, H. J. C. M. Sterenborg, and B. C. Wilson, “In vivo quantification of fluorescent molecular markers in real-time: A review to evaluate the performance of five existing methods,” *Photodiagnosis Photodyn. Ther.*, vol. 4, no. 3, pp. 170–178, 2007, doi: 10.1016/j.pdpdt.2007.02.003.
- [110] A. Kim, M. Khurana, Y. Moriyama, and B. C. Wilson, “Quantification of in vivo fluorescence decoupled from the effects of tissue optical properties using fiber-optic spectroscopy measurements,” *J. Biomed. Opt.*, vol. 15, no. 6, p. 067006, 2010, doi: 10.1117/1.3523616.
- [111] P. A. Valdes, J. P. Angelo, H. S. Choi, and S. Gioux, “qF-SSOP: real-time optical property corrected fluorescence imaging,” *Biomed. Opt. Express*, vol. 8, no. 8, p. 3597, 2017, doi: 10.1364/BOE.8.003597.
- [112] R. S. Bradley and M. S. Thorniley, “A review of attenuation correction techniques for tissue fluorescence,” *J. R. Soc. Interface*, vol. 3, no. August 2005, pp. 1–13, 2006, doi: 10.1098/rsif.2005.0066.
- [113] P. B. Garcia-Allende *et al.*, “Uniqueness in multispectral constant-wave epi-illumination imaging,” *Opt. Lett.*, vol. 41, no. 13, p. 3098, 2016, doi: 10.1364/ol.41.003098.

- [114] A. Liemert and A. Kienle, "Exact and efficient solution of the radiative transport equation for the semi-infinite medium," *Sci. Rep.*, vol. 3, p. 2018, Jun. 2013, [Online]. Available: <https://doi.org/10.1038/srep02018>.
- [115] A. Kienle, L. Lilge, M. S. Patterson, R. Hibst, R. Steiner, and B. C. Wilson, "Spatially resolved absolute diffuse reflectance measurements for noninvasive determination of the optical scattering and absorption coefficients of biological tissue," *Appl. Opt.*, vol. 35, no. 13, pp. 2304–2314, 1996, doi: 10.1364/AO.35.002304.
- [116] A. Kienle and M. S. Patterson, "Improved solutions of the steady-state and the time-resolved diffusion equations for reflectance from a semi-infinite turbid medium," *J. Opt. Soc. Am. A*, vol. 14, no. 1, p. 246, 1997, doi: 10.1364/josaa.14.000246.
- [117] J. T. Bruulsema, J. E. Hayward, T. J. Farrell, M. Essenpreis, and M. S. Patterson, "Optical properties of phantoms and tissue measured in vivo from 0.9 to 1.3 μm using spatially resolved diffuse reflectance," in *Optical Tomography and Spectroscopy of Tissue: Theory, Instrumentation, Model, and Human Studies II*, Aug. 1997, vol. 2979, pp. 325–334, doi: 10.1117/12.280261.
- [118] T. J. Pfefer *et al.*, "Reflectance-based determination of optical properties in highly attenuating tissue," *J. Biomed. Opt.*, vol. 8, no. 2, p. 206, 2003, doi: 10.1117/1.1559487.
- [119] G. M. Palmer and N. Ramanujam, "Monte Carlo-based inverse model for calculating tissue optical properties. Part I: Theory and validation on synthetic phantoms," *Appl. Opt.*, vol. 45, no. 5, pp. 1062–1071, 2006, doi: 10.1364/AO.45.001062.
- [120] J. Angelo, C. R. Vargas, B. T. Lee, I. J. Bigio, and S. Gioux, "Ultrafast optical property map generation using lookup tables," *J. Biomed. Opt.*, vol. 21, no. 11, p. 110501, 2016, doi: 10.1117/1.jbo.21.11.110501.
- [121] T. A. Erickson, A. Mazhar, D. Cuccia, A. J. Durkin, and J. W. Tunnell, "Lookup-table method for imaging optical properties with structured illumination beyond the diffusion theory regime," *J. Biomed. Opt.*, vol. 15, no. 3, p. 036013, 2010, doi: 10.1117/1.3431728.
- [122] B. Yang, M. Sharma, and J. W. Tunnell, "Attenuation-corrected fluorescence extraction for image-guided surgery in spatial frequency domain," *J. Biomed. Opt.*, vol. 18, no. 8, p. 80503, 2013, doi: 10.1117/1.JBO.18.8.080503.
- [123] B. W. Pogue *et al.*, "Imaging targeted-agent binding in vivo with two probes," *J. Biomed. Opt.*, vol. 15, no. 3, p. 30513, 2010, doi: 10.1117/1.3449109.
- [124] K. M. Tichauer, K. S. Samkoe, K. J. Sexton, J. R. Gunn, T. Hasan, and B. W. Pogue, "Improved tumor contrast achieved by single time point dual-reporter fluorescence imaging," *J. Biomed. Opt.*, vol. 17, no. 6, p. 066001, 2012, doi: 10.1117/1.jbo.17.6.066001.

Appendix A. Publication 1: Comprehensive Phantom for interventional fluorescence molecular imaging

Paper 1: The paper with title “Comprehensive phantom for interventional fluorescence molecular Imaging” was authored by Maria Anastasopoulou, Maximilian Koch, Dimitris Gorpas, Angelos Karlas, Uwe Klemm, Pilar Beatriz Garcia-Allende and Vasilis Ntziachristos and was published in Journal of Biomedical Optics.

As described in Chapter 1, calibration and standardization of imaging systems is a challenge for Fluorescence imaging. In this paper, current fluorescence phantoms for standardization were reviewed, their limitations were discussed and the need for a universal strategy for fluorescence imaging calibration was highlighted. The novelty of this paper is the demonstration and evaluation of a new class of comprehensive phantoms that could be used for inter-laboratory system assessment and calibration. For the first time system specifications such as illumination homogeneity, resolution, dependency on tissue optical properties and depth, camera sensitivity and cross talk from light leaking into the fluorescence channel are assessed simultaneously through a comprehensive phantom. This is particularly an important prerequisite for intraoperative fluorescence imaging systems where a comprehensive phantom makes possible the measurement of several camera parameters with a single or few images acquisition. Thus, there is no need for development of many different phantoms, that each one would test only one or few parameters and would not be able to monitor the concurrent trade-off among all the parameters.

The analysis of the phantom and suggested possible uses of the analysis in characterizing camera system parameters are demonstrated. These system parameters that are extracted from system measurements can be employed to

- i) find optimal operation among parameters' trade-off,
- ii) to confirm system stability and performance from day to day and
- iii) to compare different imaging systems one to each-other.

We have continued this work with the improved second generation of phantoms and with demonstration of methodology for easy automated parameter extraction for system benchmarking. As an impact we received requests from other labs regarding procurement of our comprehensive phantoms.

As the first author of this paper, I performed the phantom analysis and showed the possible uses from a snapshot of the phantom. I performed the phantom characterization, therefore, I

created slab phantoms for the optical properties characterization and I performed the experiments to capture the transmittance profiles of the slabs.

Prof. Vasilis Ntziachristos, Dr. Pilar Beatriz Garcia Allende and Maximilian Koch conceptualized the first design of the phantoms and me, Maximilian Koch and Dr. Dimitris Gorpas have designed the second improved generation of Phantoms.

I drafted the manuscript, which was continuously improved after corrections from the other co-authors. Finally, I created all the graphs and figures (except Fig.3.c that was designed by Dr. Angelos Karlas) and was advised by Prof. Vasilis Ntziachristos and Dr. Dimitris Gorpas for further improvement.

This work is licensed under the Creative Commons Attribution 4.0 International License. The full legal code of the CC BY 4.0 license can be found at:

<https://creativecommons.org/licenses/by/4.0/legalcode>.

Publication

Maria Anastasopoulou, Maximilian Koch, Dimitris Gorpas, Angelos Karlas, Uwe Klemm, Pilar Beatriz Garcia-Allende, Vasilis Ntziachristos, "Comprehensive phantom for interventional fluorescence molecular imaging," *J. Biomed. Opt.* **21**(9), 091309 (2016), doi: 10.1117/1.JBO.21.9.091309.

Conference talk

Part of this study was presented as invited talk in OSA European Conferences on Biomedical Optics (ECBO) 2017.

Comprehensive phantom for interventional fluorescence molecular imaging

Maria Anastasopoulou^{a,b}, Maximilian Koch^{a,b}, Dimitris Gorpas^{a,b}, Angelos Karlas^{a,b}, Uwe Klemm^a, Pilar Beatriz Garcia-Allende^{a,b} and Vasilis Ntziachristos^{a,b,*}

^a Helmholtz Zentrum München, Institute for Biological and Medical Imaging, Ingolstädter Landstraße 1, Neuherberg D-85764, Germany

^b Technical University Munich, Chair for Biological Imaging, Arcisstraße 21, Munich D-80333, Germany

Abstract. Fluorescence imaging has been considered for over a half-century as a modality that could assist surgical guidance and visualization. The administration of fluorescent molecules with sensitivity to disease biomarkers and their imaging using a fluorescence camera can outline pathophysiological parameters of tissue invisible to the human eye during operation. The advent of fluorescent agents that target specific cellular responses and molecular pathways of disease has facilitated the intraoperative identification of cancer with improved sensitivity and specificity over non-specific fluorescent dyes that only outline the vascular system and enhanced permeability effects. With these new abilities come unique requirements for developing phantoms to calibrate imaging systems and algorithms. We briefly review herein progress with fluorescence phantoms employed to validate fluorescence imaging systems and results. We identify current limitations and discuss the level of phantom complexity that may be required for developing a universal strategy for fluorescence imaging calibration. Finally, we present a phantom design that could be used as a tool for inter-laboratory system performance evaluation.

Keywords: interventional fluorescence imaging, phantoms, polyurethane, standardization, intraoperative

*Vasilis Ntziachristos, Email: v.ntziachristos@tum.de

1 Introduction

White light imaging and human vision lack the ability to visualize under the tissue surface and are not sensitive to pathophysiological and molecular differences between diseased and healthy tissue, occasionally limiting the accurate estimation of tumor extent and tumor margins. Interventional fluorescence imaging may address these limitations in surgical or endoscopic surveillance and guidance and improve intraoperative cancer detection. Features such as high sensitivity, real-time imaging and sub-surface signal detection make interventional fluorescent molecular imaging an attractive modality for surgical guidance.

There are three general mechanisms for generating contrast for fluorescence imaging: the first uses non-specific fluorescence dyes that are distributed in the vascular system; the second uses fluorescent agents that target specific moieties associated with disease and the third is based on visualizing intrinsic or induced auto-fluorescence [1]. One of the most widely used non-specific fluorescent agents is ICG (Indocyanine green), which was FDA approved in 1959 and has been extensively used in various clinical applications including surgery or endoscopy

[1] [2]. ICG distributes primarily in the vascular system and may preferentially perfuse tumors through the enhanced permeability and retention (EPR) effect but it has not been so far shown efficient for tumor delineation and margin detection. Another dye used in intraoperative applications is methylene blue which is primarily employed in for sentinel lymph node identification and mapping [3], [4]. Lymph node mapping has also been successfully achieved by ICG [5]–[7]. Fluorescent agents that target specific cellular or molecular disease moieties are increasingly considered for improving intraoperative disease detection over ICG. Folate (B-vitamin) conjugated to fluorescein isothiocyanate (Folate-FITC) has been used to detect cancer foci in ovarian cancer patients and yielded five times more accurate visualization over stand-alone color images [8]. Similar agents have outlined renal cell carcinoma during surgery [9] and are considered in breast cancer detection [10]. A FITC labeled peptide that binds specifically to high-grade dysplasia and adenocarcinoma has been developed and used successfully for esophageal neoplasia visualization [11]. Furthermore, FITC labeled adalimumab was used for visualization of mTNF+ cells and correlated their number to the short term Crohn's disease response rates [12]. There is a much larger pool of potent agents, including labelled drugs that are considered for intraoperative imaging [1], [13]. The use of 5-ALA (aminolevulinic acid) to induce cancer auto-fluorescence has been also considered for intra-operative imaging applications. Glioma cells convert 5-ALA to Protoporphyrin IX (PPIX) which emits an intense red fluorescence signal under blue illumination. The approach has been employed in fluorescence guided resection of malignant gliomas or benign tumors such as ependymomas or meningiomas in adults [14], [15] and children [16], [17].

A large number of fluorescent camera implementations has been developed to capture fluorescence images from tissue during surgery or endoscopy [6], [18]–[20]. A common example uses a color and a fluorescence camera, visualizing the same field of view so that color and fluorescence images can be registered. Hybrid color-fluorescence cameras combine morphological (white-light) views and the underlying fluorescence contrast onto one image. Single camera systems visualizing only fluorescence have also been considered for reducing cost and camera weight [21]. Alternative approaches build systems with multiple cameras in order to visualize at different spectral bands. For example, three camera systems have been employed to collect images from two different NIR channels and one visible channel [5] [22] or for collecting information at different spectral regions for correcting fluorescence images for illumination and tissue-absorption variations in real time [23] [24]. Endoscopic and laparoscopic systems have also been developed and successfully applied in minimally invasive cancer

therapy [20] [25]. Several fluorescence imaging systems are currently commercialized for intraoperative and endoscopic use.

The wide range of intraoperative system technologies today comes with the fundamental requirement to benchmark different systems and better understand fluorescence imaging performance. For this reason, fluorescence phantoms have been proposed for system calibration. These phantoms typically mimic the optical properties of human or animal tissue at select spectral windows and contain known contrast which is employed to characterize the camera performance. In the following we review common fluorescence phantoms and then propose a new phantom design strategy that combines multiple targets at a single block, aiming to offer a comprehensive method for fluorescence imaging evaluation.

2 Fluorescence phantoms

The development of optically diffusive phantoms that mimic the optical properties of living tissue and the bio-distribution of fluorochromes in tissues has been considered for investigating light-tissue interaction phenomena and for assessing different imaging systems [26]. Generally, the phantoms developed should meet two basic requirements. They need to provide: i) long-term photo-stability in diverse environmental conditions and ii) a fixed shape (termed solid phantom) that allows no mechanical deformation over time. To meet these requirements phantoms typically use epoxy, polyester resin or polyurethane as base material which can be cured and machined to different shapes and volumes and quantum dots for fluorescence emission. Unlike organic fluorophores that suffer from fast photo-bleaching, quantum dots provide better photo-stability, required in applications involving long-term imaging [27]–[29].

2.1 Phantoms simulating tissue optical properties

Several photon propagation parameters and system specifications can be examined using phantoms. A polyurethane-based phantom has been suggested to assess the sensitivity of fluorescence cameras [30]. The phantom comprised six cylindrical wells that contained TiO_2 particles to impart photon scattering and varying quantities of NIR fluorescent quantum dots (QDots) dispersed in polyurethane (Fig. 1a). The camera sensitivity was then assessed from an image of the phantom by observing the number of visible wells on the image. In addition, epoxy-

resin-based phantoms that combine titanium dioxide (TiO_2) and aluminum oxide (Al_2O_3) can be employed to control for photon scattering anisotropy and the phase function phantom [31].

A different phantom, made by spraying a polyurethane–quantum-dot solution onto a reflective surface, has been suggested for determining the leakage of excitation light into the fluorescence channel of a camera [32]. Images from the quantum dot (QDot) distribution containing both fluorescence and light leakage signals are compared to images from an area that does not contain QDots to separate the strength of fluorescence contributions compared to excitation light cross-talk into the fluorescence channel. The authors further suggest the use of varying QDots solutions to infer the dynamic range of the camera.

In another study [33], a customized cylindrical structure with fully submerged thin tubes containing a solution of (CdSe)ZnS QDots in chloroform was constructed for assessing the imaging quality achieved as a function of fluorochrome depth. The medium surrounding the tubes consisted of a water-based homogeneous solution containing Intralipid-20%, Naphthol Green B powder and distilled water. A small amount of AlexaFluor 568 (0.2mg in a total volume of 320mL) was added to simulate tissue auto-fluorescence (Fig. 1b). The use of phantoms that establish a geometry with varying thickness and optical properties (Fig. 1c) was suggested for characterizing tissue auto-fluorescence and validating fluorescence tissue analysis [34]. The phantoms were made of porcine skin gelatin and employed Rhodamine B (RhB) or Fluorescein isothiocyanate (FITC) to impart fluorescence. The optical properties were selected to correspond to normal and diseased brain tissues. Rectangular phantoms containing variable-diameter cylindrical inclusions placed in parallel were also suggested [34].

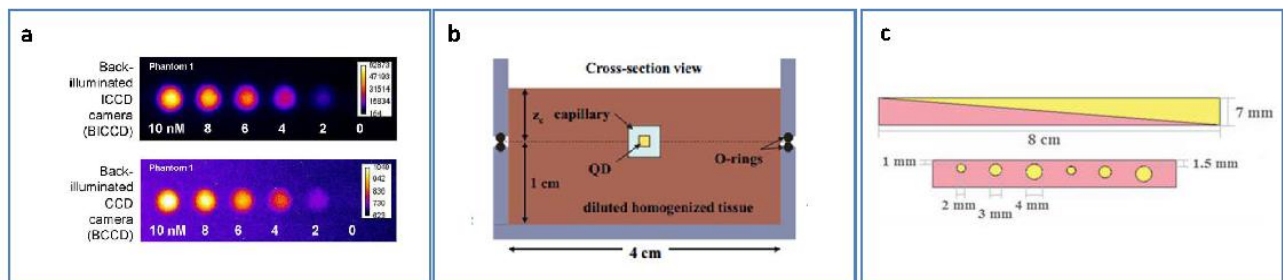


Figure 1: (a) Phantom of fluorescent wells of different strength employed to assess the sensitivity of far-red and near-infrared fluorescence imaging systems. Adapted from [30] with permission.(b) Cylindrical phantom constructed to assess fluorescent capillaries immersed at different depths under the surface within a medium simulating tissue optical properties (Cross-sectional view) reproduced from [33] with permission.(c) Schematics of a bilayer (up) and an inclusion (down) phantom. Adapted from [34] with permission.

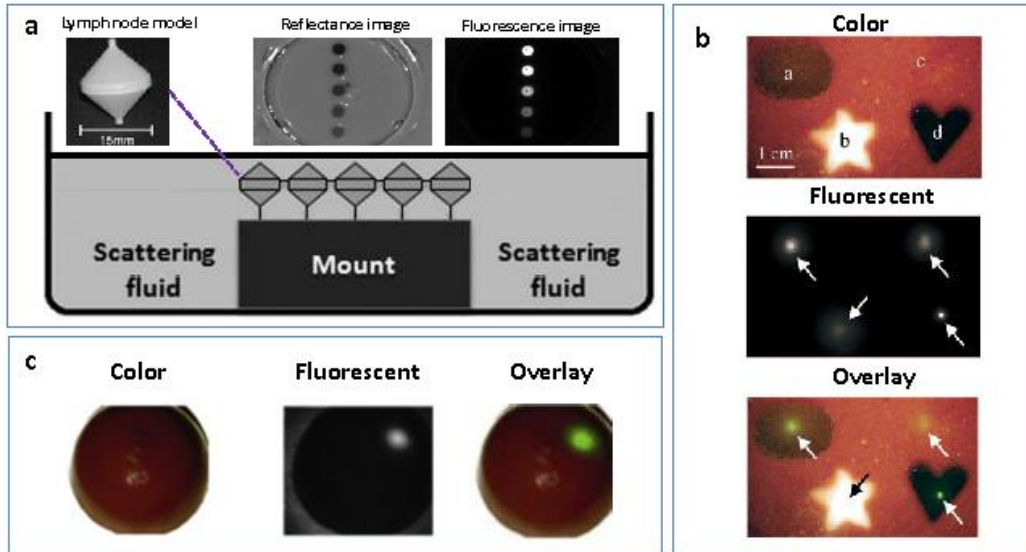


Figure 2: (a) Fluorescence lymph node phantom: Cross-sectional view, reflectance image and normalized epi-fluorescence image. Adapted from [21] with permission, (b) Complex phantom containing four compartments (a,b,c,d) with different optical properties, each of them contains a fluorescent 1mm bead (indicated by arrow) that is detected using NIRF reproduced from [35] with permission.(c) Preoperative detection of fluorescent tumor-simulating inclusion using NIRF; figure reproduced from [36] with permission.

2.2 Shape-maintaining and organ-mimicking fluorescent phantoms

A different class of tissue-mimicking phantoms focuses on simulating the geometrical features of tissue organs and can be used for clinical training in intraoperative imaging. A lymph-node mimicking phantom was constructed [21] to assess the efficacy of a real-time fluorescence imaging system (Fig. 2a). The phantom was made of thin walled polyoxomethylene cones (15 mm long and 300 μ m thick) filled with scattering fluid (water and whole ultra-heat treated milk of 3.5% fat) and fluorescent dye (ICG-Pulsion). Five lymph node-mimicking cones were mounted on a holder and immersed in a glass reservoir containing a water and milk scattering fluid.

Rectangular- or breast-shaped phantoms were also considered as a tool to train surgeons in intraoperative fluorescence imaging in breast cancer [35], [36]. A phantom made of Tris-buffered saline (TBS, buffer), sodium azide, gelatin and varying amounts of intralipid and haemoglobin was employed to simulate the geometry, optical properties and the mechanical properties of the human breast [35]. Indocyanine green (ICG)-tagged polystyrene divinylbenzene beads (AG1-X8) or Pam78-labeled hydroxyapatite crystals (simulating breast cancer microcalcifications) were used as fluorophore inclusions (Fig. 2b). In Ref. 36 varying-

shaped ICG-agarose inclusions were embedded in a mixture of TBS, gelatin, NaN₃, haemoglobin and Intralipid®, and the final structure was visualized using a customized NIRF system optimized for real-time surgical imaging[36] (Fig. 2c).

Table 1: Examples of fluorescent phantoms found in the literature (non-exhaustive list)

Reference	Chromophore	Scattering agent	Absorbing agent	Matrix material	Shape	Tissue-specific	Purpose
Zhu et al. 2014 [30] (Fig. 1-a)	QDots 800 ITK	TiO ₂ scattering particles	-	Polyurethane	Plate with many cylindrical wells	No	Assess - compare CCD cameras
Zhu et al. 2012 [32]	Qdots 800 ITK	-	-	Polyurethane	Film coated rectangular surface	No	Light leakage quantification –sensitivity estimation
Roy et al. 2011 [33] (Fig. 1-c)	(CdSe)ZnS Qdots	Intralipid	Naphthol Green B powder	Water	Capillary embedded in cylindrical structure	No	Assess imaging of subsurface fluorescence agents
Szyc et al. 2015 [21] (Fig. 2-a)	ICG-Pulsion	Milk	-	Water	Plate with five conical phantoms	Yes - SLN	Assess fluorescence imaging system (SLN mapping)
De Grand et al. 2006 [[35](Fig.2-b)	(ICG)-labeled AG1-X8 or Pam78-labeled hydroxyapatite crystals	Intralipid	Hemoglobin	Gelatin	Rectangular- or breast-shaped	Yes – Breast	Training platform for surgeons
Pleijhuis et al. 2011 [36] (Fig. 2-c)	ICG	Intralipid	Hemoglobin	Agarose/ Gelatin	Breast-shapes	Yes- Breast	Assess the applicability of NIRF imaging in breast-conserving

2.3 Requirement for a new class of phantoms

Table 1 summarizes a non-exhaustive list of fluorescent phantoms and demonstrates a great variability in approaches and materials used. The phantoms listed have been developed to address different specifications and needs, for example the characterization of a specific property (e.g. sensitivity) or the study of a physical property (e.g. effect of depth). Typically only a single or few specifications are addressed[30] [32] [37]. However, there is a large range of parameters that may require validation in the clinical use of fluorescence cameras. Parameters such as the illumination homogeneity, the resolution, the dependency of fluorescence intensity on tissue optical properties or depth are not generally comprehensively addressed in the phantoms built so far. Therefore, there is a need for a new class of phantoms that simultaneously assess multiple parameters. This is particularly a requirement in intraoperative settings, where a single image calibration can longitudinally confirm system operation. Also a comprehensive phantom that concurrently enables the measurement of multiple camera parameters is necessary for the comparison of different camera systems or operational parameters. The use of a comprehensive phantom therefore eliminates the need to develop a large number of different phantoms, each testing a single or few parameters only.

3 Methods

We designed and constructed a solid polyurethane phantom with the purpose of evaluating a range of camera parameters using a single snapshot. The parameters assessed include sensitivity, fluorescence intensity variations as a function of optical properties and depth, cross talk from excitation light leaking into the fluorescence channel, illumination homogeneity and resolution.

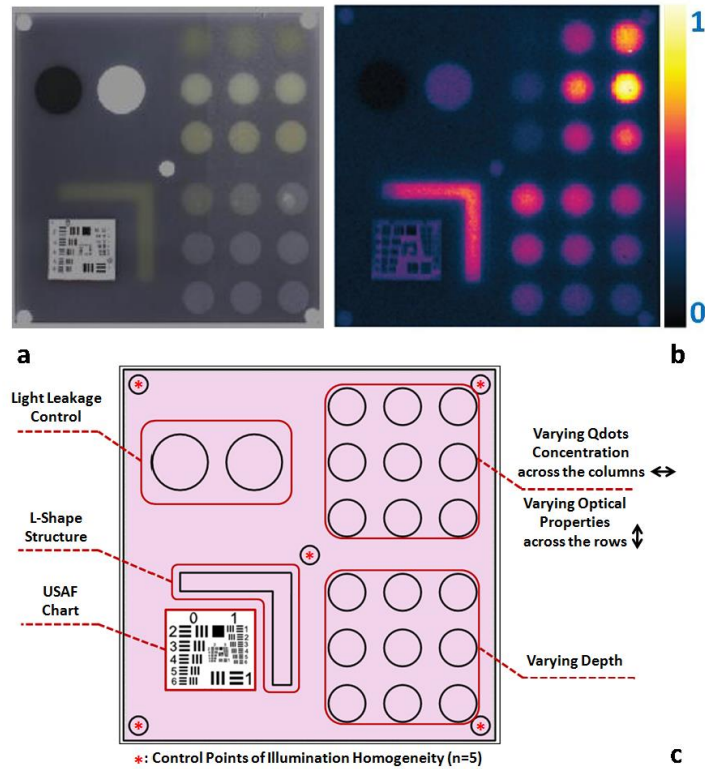


Figure 3: Top view of the phantom. a) Color image of the phantom. b) Fluorescence image (765 to 855nm) of the phantom excited at 750 nm. c) Schematic of the phantom

3.1 Phantom design and fabrication

The solid phantom designed is depicted in Fig. 3. Figure 3a shows a color image of the fabricated phantom and Fig. 3b shows a fluorescence image of the phantom. The phantom is made of transparent rigid polyurethane (WC-783 A/B, BJB Enterprises, Tustin, USA) and contains different structures interrogating different aspects of fluorescence camera specifications and imaging performance. The outer dimensions of the phantom are 10 x 10 x 2.2 cm³. The background absorption was set to $\sim 0.5 \text{ cm}^{-1}$ at 750 nm, using alcohol soluble nigrosin (Sigma Aldrich, St.Louis, USA). Scattering was imparted by using 1 mg/g TiO₂ particles (Titanium IV Oxide, Sigma Aldrich, St. Louis, USA), resulting in a reduced scattering coefficient of $\sim 10 \text{ cm}^{-1}$ at 750 nm. The high background absorption coefficient in this phantom offers the additional advantage of low photon diffusion from the different structures selected into the background medium. The absorption coefficient was determined by measuring the extinction coefficient of nigrosin using an Ocean Optics USB4000-UV-VIS spectrometer and then selecting the appropriate concentration to impart the desired absorption coefficient. The reduced

scattering coefficient was determined by fitting the diffusion equation in a measurement of the spatial transmittance profile of a point source through a 1cm slab of cured polyurethane containing TiO₂ particles and a known absorption coefficient, as determined by measuring the solvent by photo-spectrometry prior to the addition of the particles. All the inlets in the phantom, except for the ones used for depth dependence evaluation, were made 12 mm deep. The different phantom compartments are schematically explained in Fig. 3c.

The upper right quadrant of the phantom interrogates the sensitivity and fluorescence intensity variation as a function of optical properties through an array of nine fluorescent wells (10 mm diameter). The wells contain a mix of cured polyurethane with quantum dots (800 nm emission; Thermofisher Scientific, Waltham, USA) at varying concentrations (1 nM, 5 nM and 10 nM) across the columns and varying absorber (20 µg/g, 20 µg/g and 40 µg/g Hemin) and varying TiO₂ amounts (0.33, 0.66 and 1 mg/g TiO₂) across the rows. Hemin (Sigma Aldrich, St. Louis, USA) was selected to simulate an absorption coefficient 0.25 cm⁻¹ for 20 µg/g and 0.5 cm⁻¹ for 40 µg/g

The bottom right quadrant comprises nine fluorescence wells; whereby 10 mm diameter cylinders made of 10nM 800 nm quantum dots 0.66 mg/g TiO₂ particles and 20 µg/g Hemin were embedded at varying depths within the phantom, i.e. at an increasing depth from the phantom surface at 0.2, 0.4, 0.6, 0.8, 1, 1.33, 1.66, 2 and 3 mm. After the quantum dot (QDot) mix was poured into the well to reach the appropriate depth, it was allowed to cure and then the cavity was filled with the same material employed in the construction of the phantom body. This quadrant examines the fluorescence sensitivity to depth and can be used to study the ability of a system or method to account for the effects of depth on the fluorescence signal.

The upper left quadrant examines the camera dark-current offset and the camera cross-talk, i.e. the excitation light leakage into the fluorescence channel. Light leakage could be caused due to inadequate excitation light rejection from system filters. This area comprises a circular well of very high absorption coefficient (3.74 mg/g Nigrosin) and one of low absorption and high scattering coefficient (10mg/g Titanium oxide) offering reflecting characteristics. The circular elements were embedded in the background material and do not contain fluorescence substances. Inspection of the dark area approximates the dark light camera photon count “dc-offset” (although a separate measurement with the excitation light off can be also performed). Inspection of the reflective non-fluorescent area reveals the camera cross-talk with better signal to noise ratio characteristics over observing the cross-talk seen from the phantom background material. This cross-talk measurement can be utilized in different ways as discussed in the

results (see 3.2). . In addition, signals captured in the fluorescence channel from the highly scattering well of the upper left quadrant can be employed in a differential way to evaluate stray light, for example using two measurement; one with ambient light on and one with ambient light off.

Finally the lower left quadrant tests for the resolution of the optical system and cameras employed. A standard 1951 United States Air Force resolution test chart is fixed on top of the phantom to interrogate the white-light optical resolution, useful for characterizing the color or the fluorescence camera employed. In addition, an L shaped diffusive fluorescence structure, made of polyurethane, 0.66 mg/g TiO₂ particles , 20 µg/g Hemin and 10 nM quantum dots was embedded for the examination of photon diffusion and of fluorescence resolution. The outer dimensions of the L shaped structure are 30 mm x 30 mm x 12 mm, whereas the width of each branch is 5 mm.

Five identical reflective circular areas (5 mm diameter) made of 10 mg/g Titanium oxide in polyurethane; 4 at the corners of the phantom and 1 at the center sample the homogeneity of the light illumination employed by the camera system.

The phantom was produced by molding a cuboid made of the base material. After curing, the cuboid was treated by face milling of the surfaces. Openings were milled for each of the desired wells and shapes. All milling procedures were performed on a cartesian computer numerical controlled 3-axis milling router with µm resolution.

3.2 Imaging system

A home-made EagleRay-V3 imaging system previously developed for intraoperative imaging[38] was employed for the experimental measurements herein. The EagleRay-V3 system is a hybrid color-fluorescence system employing an iXon-3 electron multiplying charge-coupled device (DU-897 EMCCD; Andor Technology, Belfast, Ireland) for fluorescence detection and a 12-bit-CCD camera (pixelfly qe, PCO, Kelheim, Germany) for color detection. A 300 mW continuous laser diode (BWF2-750-0, B&W Tek, Newark, USA) at 750 nm was used for fluorescence excitation and a 250 W halogen lamp (KL-2500 LCD, Scott, Mainz, Germany) was employed for white light illumination.

4 Results

We demonstrate the analysis of phantom images and suggest possible uses of the analysis in characterizing system parameters. These parameters can be employed to compare different systems to each-other, using a single photographic measurement for each system. Another use of the parameters extracted from phantom measurements is to confirm that the system performs identically from day to day; a parameter that is particularly critical in intra-operative environments.

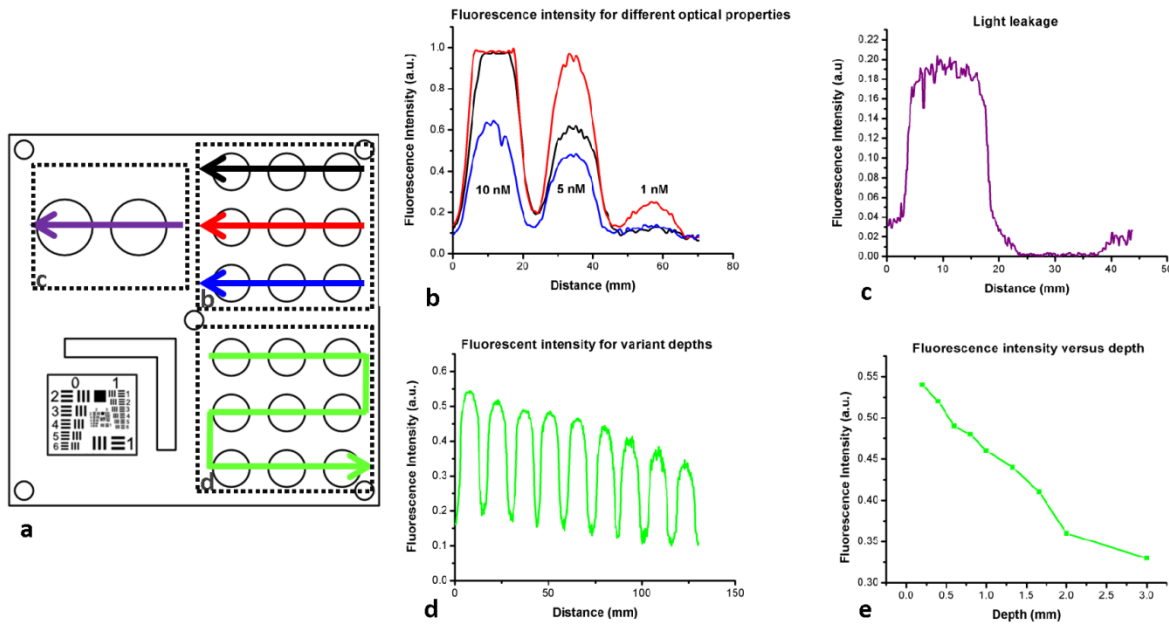


Figure 4: Cross sections of the fluorescent image of the phantom. (a) Phantom schematic with arrows painted with colors corresponding to the cross sections. (b) Fluorescence intensity across each column (different fluorophore concentration). (c) Intensity across the highly reflecting and absorbing area. (d) Fluorescence Intensity for different depths. (e) Fluorescence Intensity versus the depth distance.

4.1 Sensitivity and intensity variation due to optical properties

System sensitivity can be assessed by observing the fluorescence collected from the upper right quadrant wells. Fig. 4b shows the fluorescence profiles across the 9 wells, plotted from right to left as shown on Fig. 4a. The profiles demonstrate variations in intensity since each row of the 3x3 matrix of cells contains a different combination of optical properties and each column contains a different QDot concentration at 1, 5 and 10 nM from right to left respectively. The plot allows the evaluation of sensitivity not only under different fluorochrome concentrations, but also for varying optical properties. Even though each column contains exactly the same amount of

quantum dots, different fluorescence intensities are recorded from the three wells in that column due to the variation of optical properties. Importantly therefore, the upper right quadrant can be also employed to evaluate algorithms that account for the effects of optical properties on the fluorescence intensity.

As observed on Fig.4d, the system can detect 1nM of fluorochrome concentration only in the low attenuation well. Therefore it appears that under the operational conditions applied herein, the sensitivity of the system is between 1nM and 5nM, depending on the background optical properties.

4.2 Light Leakage

Fig. 4c depicts the cross section across the two wells contained in the upper left quadrant of the phantom, which examines the light leakage and dark count. The light leakage measurement can be utilized in different ways. It can be related to fluorescence intensity measurements (for example from the upper right quadrant of the phantom) to provide a relative metric of light leakage recorded from a low-absorption and non-fluorescent lesion to measurements from lesions containing varying amounts of fluorochrome. The ratio of fluorescence measurement for a certain well in the upper right quadrant over the light leakage signal is a quality metric; the higher the value the better the ability of a camera to discriminate a fluorochrome over cross-talk. Another method utilizing the light leakage measurement is to observe the intensity of the excitation light reflected off the reflective well using the color camera (i.e. from Fig. 3a) and generate a ratio of the light leakage measurement (from Fig. 3b) over reflected light on Fig. 3a. This ratiometric measure can be also used to compare the performance of different cameras or examine the performance of algorithms correcting for light leakage.

The measurement shown in Fig. 4c was intentionally performed using filters offering medium excitation light rejection to illustrate that it is possible to obtain light leakage signals that are stronger than fluorescence signals, depending on the system design. For example when comparing the signal intensity collected in the leakage channel to the fluorescence intensity seen in the left-most column of the upper-right quadrant, one can observe that the light-leakage is stronger than the fluorescence signal obtained from low (1nM) QDot concentrations and highly absorbing lesions.

4.3 Depth

Figure 4d shows the fluorescence intensity profiles as a function of fluorochrome depth across the nine varying depth entities, plotted in the order that is indicated by the arrow on Fig.4.a. As expected, a decrease of fluorescence intensity is observed for increasing depth. The rate of signal drop with depth is depicted in Fig.4e. The figure shows at least a 2-fold fluorescence intensity reduction over the first 3 mm of lesion depth and for the optical properties selected. This measurement can be employed to examine the performance of cameras and algorithms that account for depth-related fluorescence signal variations.

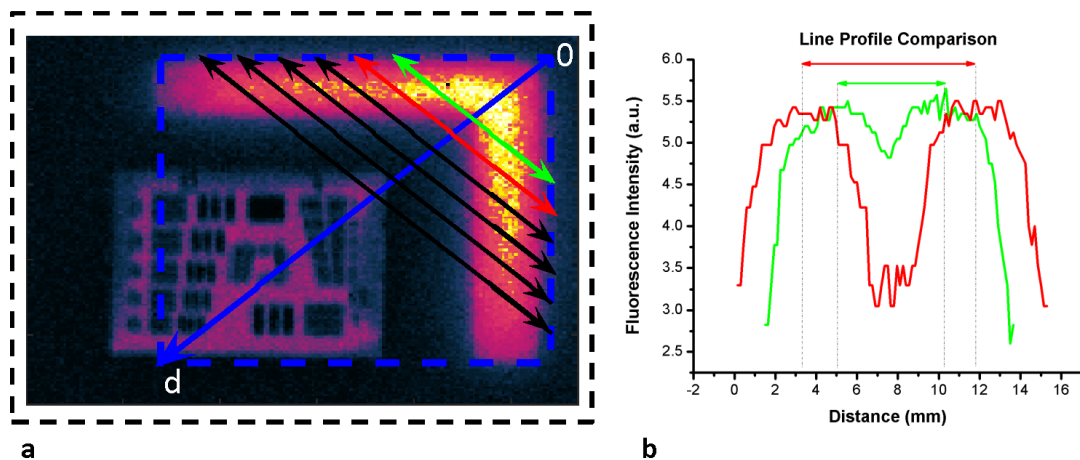


Figure 5: Resolution assessment (a) L shaped structure and the lines drawn across the x axis. (b) Cross section profiles of the green and red line from figure (a) and their distance from the inner vertex of L-shape structure is shown.

4.4 Fluorescence Resolution

Figure 5 shows the fluorescence image from the lower left quadrant, which can be employed to evaluate the diffusive resolution achieved in the fluorescence channel. The manufactured L-shape has a sharp border. However, due to photon diffusion, the border appears of low resolution. To evaluate the diffusive resolution, we plotted fluorescence intensity profiles (Fig. 5b) along the diagonal double-arrow lines plotted on Fig. 5a. The diagonal double-arrow line indicates the x-axis on Fig. 5b, whereby the y-axis is the fluorescence intensity recorded along the profile shown and the position on the d axis indicates the distance from the inner vertex of the L-shape structure. The minimum step between the lines could be 1 pixel diagonal, but for better visualization, a step of 20 diagonal lines was used. The profiles confirm that even though the L-Shape has been constructed with a hard border between fluorescence and non-

fluorescence material, the resulting reading has a diffusive appearance. These readings can be useful for evaluating cameras and algorithms that improve upon photon diffusion. One resolution improvement metric that could be implemented with this phantom would be the comparison achieved between the L-shape edge (border) resolved on a diffusion-corrected image and the location of the known manufactured edge of the L-shape structure. Another resolution metric could be implemented by reporting the distance on the x-axis (Fig. 5b), whereby the plotted fluorescence intensity profiles start to be resolved. The L-shape phantom allows for a gradual distance increase between the two edges, so that different distances between the edges can be seamlessly evaluated.

4.5 Illumination Homogeneity

The illumination homogeneity can be evaluated by plotting the intensity measurements recorded for the 5 reflective wells placed in the corners and center of the phantom. Figure 6a,b depicts the intensity profiles as cross-sections across the 5 reflective wells. These profiles serve as a quick estimation of the illumination field homogeneity. Using 5 sampling points we can define a three dimensional surface that approximates the illuminating field. Since a single illumination source was employed in the study, we fitted a cubic spline curve to the 5 points, as shown in Fig.6c. More generally a larger number of sampling points on the phantom and higher order polynomial surface fits can be employed for describing more complex illumination fields. Tracking the illumination pattern, as shown in Fig.6c, can help in correcting the fluorescence images by normalizing them for the excitation field variation or help to adjust the illumination to make it more homogeneous.

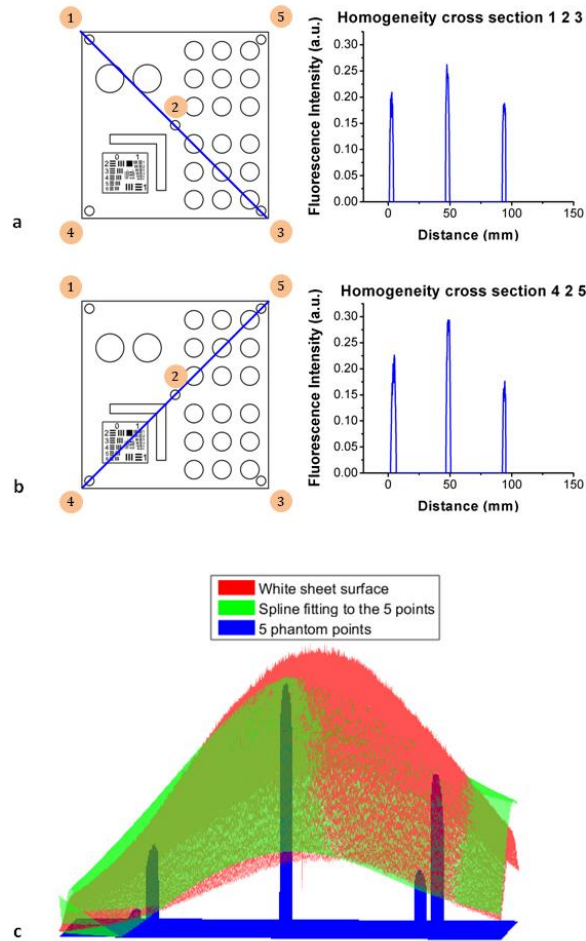


Figure 6: Assessment of the homogeneity of the illumination field of the camera system. a) Homogeneity profiles across the left-upper-corner – right-bottom-corner. b) Homogeneity profiles across the right-upper corner –left bottom corner. (c) Comparison of the 5 reflective spots surface profile with the surface profile of a white reflectance sheet.

5 Discussion

There is a large selection of camera systems and technologies developed to serve clinical fluorescence molecular imaging applications. The diversity in fluorescence detection directs the need for fluorescence phantoms that can seamlessly characterize the performance of a system or method over time or compare systems to each-other. Ideally, a single phantom could offer comprehensive information on multiple system parameters with a single snapshot.

The phantom constructed can assess multiple parameters of a camera while maintain long term stability requirements. The use of materials that do not vary their optical properties over time is critical. Phantoms that are employed for surgical training are usually manufactured based on

hydrogels (agar and gelatin). Hydrogels impart tissue-like mechanical plasticity and make phantoms appropriate for surgical training and simulating intraoperative fluorescence imaging conditions. However, hydrogels do not maintain long term optical property and shape stability (rigidity). Solid phantoms made of epoxy, polyester resin or polyurethane offer a better solution for camera characterization, since they can maintain shape rigidity and can be machined to elaborate patterns and shapes. Silicone phantoms have been also proposed [39] and offer an intermediate solution of maintaining plasticity and longer term optical property stability. Overall, we selected herein polyurethane as the base material due to the long term stability of optical properties it provides [40], [41].

Scattering is imparted using three main approaches, i.e. using lipid microparticles, polymer microparticles or white metal oxide powders [26]. A widely used lipid-based scatterer is intralipid. Intralipid is an emulsion of soya oil in water that is sold commercially in calibrated lipid solutions for intravenous feeding and it is used primarily in liquid phantoms or gelatin phantoms. Regarding the polymer microspheres, polystyrene is a common microsphere employed and imparts a scattering spectrum that can be easily predicted with theoretical calculations [26]. Nevertheless, the widespread availability of white metal oxide powders due to its use in manufacturing common white paint and its seamless integration with polyurethane often makes TiO_2 powder a preferred choice for solid phantoms [37], [42], [43].

Absorbing powders and inks have been used as the main approaches to impart absorption in phantoms. India ink produces a relatively flat absorption spectrum across most of the visible and near infrared wavelength [26]. Regarding powders, a common powder employed in literature is nigrosine.[44] Other powders that have been reported are Graphite powder [45] and Naphthol Green B powder[33]. Coffee has been also utilized as an absorbing agent since it attains an absorption spectrum similar to that of human melanin [44]. In this work we selected to use nigrosine as the absorbing pigment in the matrix material due to its seamless incorporation into polyurethane. Hemin was also used as absorbing agent in the testing inlets because it resembles the optical spectrum of blood.

The selection of the fluorescent moiety employed in a phantom is guided by its photo-stability and the ability to easily incorporate with the phantom's base materials. Quantum dots are preferred in the manufacturing of fluorescence phantoms due to their advantageous photo-stability over time and their ability to integrate in solid phantoms without quenching. Quantum dots can fluoresce in the visible and near-infrared and are therefore well-suited to simulate the fluorescence of biocompatible fluorophores such as ICG or Fluorescein isothiocyanate (FITC).

The phantom shown has additional complexity over previously reported phantoms. Extended micromachining is necessary in order to impart the desired patterns in the different quadrants. In addition methods for fabricating multilayer structures were necessary, in particular for simulating fluorochromes at different depths; processes that include mold multilayer curing. Phantoms that represent higher complexity that simulate diverse structural and optical heterogeneities common in biological tissue, may benefit by 3D printing techniques [45] and rapid prototyping of phantom with patient oriented capabilities[46].

The developed phantom that was presented above can be used as a universal comprehensive tool for the assessment of a system performance over time and for the comparison of different systems. Nevertheless some parameters can be also determined in an absolute manner, for example the minimum fluorochrome amount that can be recorded, which indicates sensitivity, or the illumination field homogeneity. A major advantage of the phantom over previous developments is that multiple system parameters can be measured in one snapshot. In results we discussed possible uses of the measurements performed. Overall different utilizations of the parameters analyzed and different phantom configurations may be proposed to examine different parameters or the same parameters in different ways. However, we expect the use of complex phantoms that could assess camera performance in one snapshot could become essential for standardization and calibration operations in fluorescence molecular imaging. In the future such phantoms can be used for testing algorithmic and methodological approaches designed to improve the performance of fluorescence imaging, for example against the variation of optical properties or depth. In addition a larger amount of wells can be implemented to test for a larger range of sensitivities and optical property variation. The latter would be important to better assess dynamic range characteristics of the camera, which is also a critical parameter in clinical fluorescence imaging studies.

Acknowledgements

The research leading to these results has received funding from the Deutsche Forschungsgemeinschaft (DFG), Germany [Leibniz Prize 2013; NT 3/10-1].

References

1. M. Koch and N. Ntziachristos, "Advancing surgical vision with fluorescence imaging," *Annu. Rev. Med.*, 67 153 –164 , (2016).
2. J. T. Alander et al., "A review of indocyanine green fluorescent imaging in surgery," *Int. J. Biomed. Imaging*, 2012 1 –26 (2012).
3. M. Chu and Y. Wan, "Sentinel lymph node mapping using near-infrared fluorescent methylene blue," *J. Biosci. Bioeng.*, 107 455 –459 (2009).
4. A. Nour, "Efficacy of methylene blue dye in localization of sentinel lymph node in breast cancer patients," *Breast J.*, 10 388 –391 (2004).
5. S. L. Troyan et al., "The FLARE(TM) intraoperative near-infrared fluorescence imaging system: a first-in-human clinical trial in breast cancer sentinel lymph node mapping," *Ann. Surg. Oncol.*, 16 2943 –2952 (2009).
6. Y. Fujisawa et al., "A custom-made, low-cost intraoperative fluorescence navigation system with indocyanine green for sentinel lymph node biopsy in skin cancer," *Dermatology*, 222 261 –268 (2011).
7. Y. Tajima et al., "Sentinel node mapping guided by indocyanine green fluorescence imaging in gastric cancer," *Ann. Surg.*, 249 58 –62 (2009).
8. G. M. van Dam et al., "Intraoperative tumor-specific fluorescence imaging in ovarian cancer by folate receptor- α targeting: first in-human results," *Nat. Med.*, 17 1315 –1319 (2011).
9. T. J. Guzzo et al., "Intraoperative molecular diagnostic imaging can identify renal cell carcinoma," *J. Urol.*, 195 (3), 749 –755 (2015).
10. S. Singhall, "Intraoperative imagery of breast cancer with folate-fitc (EC17)," (2016)
11. M. B. Sturm et al., "Targeted imaging of esophageal neoplasia with a fluorescently labeled peptide: first-in-human results," *Sci. Transl. Med.*, 5 (184), 184ra61 (2013).
12. R. Atreya et al., "In vivo imaging using fluorescent antibodies to tumor necrosis factor predicts therapeutic response in Crohn's disease," *Nat. Med.*, 20 313 –318 (2014).
13. W. Scheuer et al., "Drug-based optical agents: infiltrating clinics at lower risk," *Sci. Transl. Med.*, 4 134ps11 (2012).

14. W. Stummer et al., "Fluorescence-guided resection of glioblastoma multiforme utilizing 5-ALA-induced porphyrins: a prospective study in 52 consecutive patients," 93 1003 –1013 (2000).
15. S. Esteves et al., "A pilot cost-effectiveness analysis of treatments in newly diagnosed high-grade gliomas: the example of 5-aminolevulinic acid compared with white-light surgery," *Neurosurgery*, 76 552 –562 (2015).
16. W. Stummer et al., "Predicting the 'usefulness' of 5-ALA-derived tumor fluorescence for fluorescence-guided resections in pediatric brain tumors: a European survey," *Acta Neurochir. (Wien)*, 156 2315 –2324 (2014).
17. L. M. Bernal García et al., "Fluorescence-guided resection with 5-aminolevulinic acid of meningeal sarcoma in a child," *Child's Nerv. Syst.*, 3 –6 (2015).
18. G. Themelis et al., "Real-time intraoperative fluorescence imaging system using light-absorption correction," *J. Biomed. Opt.*, 14 (6), 064012 (2014).
19. J. S. D. Mieog et al., "Novel intraoperative near-infrared fluorescence camera system for optical image-guided cancer surgery," *Mol. Imaging*, 9 (4), 223 –231 (2010).
20. C. Chi et al., "Intraoperative imaging-guided cancer surgery: from current fluorescence molecular imaging methods to future multi-modality imaging technology," *Theranostics*, 4 1072 –1084 (2014).
21. Ł. Szyc et al., "Development of a handheld fluorescence imaging camera for intraoperative sentinel lymph node mapping," *J. Biomed. Opt.*, 20 (5), 051025 (2015).
22. S. L. Troyan et al., "The FLARE intraoperative near-infrared fluorescence imaging system: a first-in-human clinical trial in breast cancer sentinel lymph node mapping," *Ann. Surg. Oncol.*, 16 2943 –2952 (2009).
23. G. Themelis, J. S. Yoo and V. Ntziachristos, "Multispectral imaging using multiple-bandpass filters," *Opt. Lett.*, 33 1023 –1025 (2008).
24. L. M. A. Crane et al., "Intraoperative multispectral fluorescence imaging for the detection of the sentinel lymph node in cervical cancer: a novel concept," *Mol. Imaging Biol.*, 13 1043 –1049 (2011).
25. M. D. Jafari et al., "The use of indocyanine green fluorescence to assess anastomotic perfusion during robotic assisted laparoscopic rectal surgery," *Surg. Endosc.*, 27 (8), 3003 –3008 (2013).
26. B. W. Pogue and M. S. Patterson, "Review of tissue simulating phantoms for optical spectroscopy, imaging and dosimetry," *J. Biomed. Opt.*, 11 (4), 041102 (2006).

27. U. Resch-Genger et al., "Quantum dots versus organic dyes as fluorescent labels," *Nat. Methods*, 5 763 –775 (2008).
28. X. Gao et al., "In vivo molecular and cellular imaging with quantum dots," *Curr. Opin. Biotechnol.*, 16 63 –72 (2005).
29. A. P. Alivisatos, W. Gu and C. Larabell, "Quantum dots as cellular probes," *Annu. Rev. Biomed. Eng.*, 7 55 –76 (2005).
30. B. Zhu, J. C. Rasmussen and E. M. Sevick-Muraca, "A matter of collection and detection for intraoperative and noninvasive near-infrared fluorescence molecular imaging: to see or not to see?," *Med. Phys.*, 41 022105 (2014).
31. P. Krauter et al., "Optical phantoms with adjustable subdiffusive scattering parameters," *J. Biomed. Opt.*, 20 (10), 105008 (2015).
32. B. Zhu et al., "Validating the sensitivity and performance of near-infrared fluorescence imaging and tomography devices using a novel solid phantom and measurement approach," *Technol. Cancer Res. Treat.*, 11 (1), 95 –104 (2012).
33. M. Roy et al., "Homogenized tissue phantoms for quantitative evaluation of subsurface fluorescence contrast," *J. Biomed. Opt.*, 16 (1), 016013 (2011).
34. B. Leh, "Optical phantoms with variable properties and geometries for diffuse and fluorescence optical spectroscopy," *J. Biomed. Opt.*, 17 (10), 108001 (2012).
35. A. M. De Grand et al., "Tissue-like phantoms for near-infrared fluorescence imaging system assessment and the training of surgeons," *J. Biomed. Opt.*, 11 (1), 014007 (2006).
36. R. G. Pleijhuis et al., "Near-infrared fluorescence (NIRF) imaging in breast-conserving surgery: assessing intraoperative techniques in tissue-simulating breast phantoms," *Eur. J. Surg. Oncol.*, 37 32 –39 (2011).
37. T. Moffitt, Y.-C. Chen and S. A. Prahl, "Preparation and characterization of polyurethane optical phantoms," *J. Biomed. Opt.*, 11 (4), 041103 (2006).
38. J. Glatz et al., "Concurrent video-rate color and near-infrared fluorescence laparoscopy," *J. Biomed. Opt.*, 18 (10), 101302 (2013).
39. G. Lamouche et al., "Review of tissue simulating phantoms with controllable optical, mechanical and structural properties for use in optical coherence tomography," *Biomed. Opt. Express*, 3 1381 (2012).
40. I. Noiseux et al., "Development of optical phantoms for use in fluorescence-based imaging," *Proc. SPIE*, 7567 75670B (2010).

41. M. L. Vernon et al., "Fabrication and characterization of a solid polyurethane phantom for optical imaging through scattering media," *Appl. Opt.*, 38 4247 –4251 (1999).
42. G. Wagnières et al., "An optical phantom with tissue-like properties in the visible for use in PDT and fluorescence spectroscopy," *Phys. Med. Biol.*, 42 1415 –1426 (1997).
43. J. Baeten et al., "Development of fluorescent materials for diffuse fluorescence tomography standards and phantoms," *Opt. Express*, 15 8681 –8694 (2007).
44. R. B. Saager et al., "Multilayer silicone phantoms for the evaluation of quantitative optical techniques in skin imaging," *Proc. SPIE*, 7567 756706 (2010).
45. M. Wang et al., "3D printing method for freeform fabrication of optical phantoms simulating heterogeneous biological tissue," *Proc. SPIE*, 8945 894509 (2014).
46. J. I. Gear et al., "Development of patient-specific molecular imaging phantoms using a 3D printer," *Med. Phys.*, 41 (8), 082502 (2014).

Appendix B. Publication 2: Fluorescence imaging reversion using spatially variant deconvolution

Paper 2: The paper with title “Fluorescence imaging reversion using spatially variant deconvolution” was authored by Maria Anastasopoulou, Dimitris Gorpas, Maximilian Koch, Evangelos Liapis, Sarah Glasl, Uwe Klemm, Angelos Karlas, Tobias Lasser and Vasilis Ntziachristos and was published in Scientific Reports.

As described in Chapter 1, Near Infrared Fluorescence Molecular Imaging (NIR FMI) is emerging into a valuable tool for surgical guidance and early diagnosis in oncology, but, NIR FMI suffers from photon diffusion in tissue that degrades image quality. Photon scattering in tissue distorts image quality and deteriorates the tumor margin detection during fluorescence intraoperative surgery. Low resolved images can mislead the surgeon to excessive removal of healthy tissue or to incomplete cancer resection. Herein, we introduce the concept of acquiring the spatially-dependent impulse response of the tissue image and show a novel framework that uses these spatially-dependent kernels into a deconvolution process to enhance the quality of the acquired fluorescence image.

A point-like beam from a Digital Light Projector (DLP) is scanned across the area of interest, and the corresponding spatially variant kernels are retrieved, fitted to Gaussian curves and enable a spatially adaptive deconvolution, that we developed, based on a modified fast Lucy-Richardson deconvolution algorithm. Unlike other fluorescence diffusion correction methods, which presume tissue homogeneity, the proposed method considers the spatial heterogeneity of scanned tissue by relying on experimentally-extracted tissue-specific data. Herein, we describe our method and showcase its efficiency with phantoms and ex vivo tissues of tumor bearing mice. The improvement achieved in this proof-of-concept study is very promising for future clinical applications. Moreover, we discuss how our method can be implemented in clinical systems and we are currently working towards minimization of both acquisition and computational times.

As the first author of this paper, I performed all the phantom and ex vivo experiments. I did all the data analysis and implemented the deconvolution algorithm. I also configured the DLP scanning, acquisition and fitting with the help of Dr. Dimitris Gorpas and Maximilian Koch. I wrote the deconvolution algorithm with help from Maximilian Koch and Dr. Tobias Lasser. I developed the phantoms for the proof of concept imaging. Additionally, I wrote the performance metrics scripts with advice from Dr. Tobias Lasser and Dr. Dimitris Gorpas. Furthermore, I

selected the tumor models to showcase the algorithm with biological advice from Dr. Evangelos Liapis, Sarah Glasl, Uwe Klemm and Dr. Angelos Karlas.

I drafted the manuscript, which was continuously improved after corrections from the other co-authors. Finally, I created all the graphs and schematics and was advised by Prof. Vasilis Ntziachristos, Dr. Dimitris Gorpas and Dr. Tobias Lasser for further improvement.

This work is licensed under the Creative Commons Attribution 4.0 International License. The full legal code of the CC BY 4.0 license can be found at:

<https://creativecommons.org/licenses/by/4.0/legalcode>.

Publication

Maria Anastasopoulou, Dimitris Gorpas, Maximilian Koch, Evangelos Liapis, Sarah Glasl, Uwe Klemm, Angelos Karlas, Tobias Lasser, Vasilis Ntziachristos, “Fluorescence imaging reversion using spatially variant deconvolution”, *Sci. Rep.* **9**(1), 18123 (2019), doi:10.1038/s41598-019-54578-0

Conference talk

Part of this study was presented in SPIE Biomedical Optics Symposium (BIOS) in Photonics West Conference 2020.

Fluorescence imaging reversion using spatially variant deconvolution

Maria Anastasopoulou^{1, 2}, Dimitris Gorpas^{1, 2}, Maximilian Koch^{1, 2}, Evangelos Liapis^{1, 2}, Sarah Glasl², Uwe Klemm², Angelos Karlas^{1, 2}, Tobias Lasser³, Vasilis Ntziachristos^{1, 2, *}

¹ Chair of Biological Imaging and TranslaTUM, Technical University Munich, Munich, 81675, Germany

² Institute of Biological and Medical Imaging, Helmholtz Zentrum München, Neuherberg, 85764, Germany

³ Computer Aided Medical Procedures, Technical University Munich, Garching, 85748, Germany

*v.ntziachristos@tum.de

ABSTRACT

Fluorescence imaging opens new possibilities for intraoperative guidance and early cancer detection, in particular when using agents that target specific disease features. Nevertheless, photon scattering in tissue degrades image quality and leads to ambiguity in fluorescence image interpretation and challenges clinical translation. We introduce the concept of capturing the spatially-dependent impulse response of an image and investigate Spatially Adaptive Impulse Response Correction (SAIRC), a method that is proposed for improving the accuracy and sensitivity achieved. Unlike classical methods that presume a homogeneous spatial distribution of optical properties in tissue, SAIRC explicitly measures the optical heterogeneity in tissues. This information allows, for the first time, the application of spatially-dependent deconvolution to correct the fluorescence images captured in relation to their modification by photon scatter. Using experimental measurements from phantoms and animals, we investigate the improvement in resolution and quantification over non-corrected images. We discuss how the proposed method is essential for maximizing the performance of fluorescence molecular imaging in the clinic.

Introduction

Fluorescence imaging has been widely used for assessing the distribution of fluorescent agents in tissues[1]–[5] and it is increasingly considered in clinical applications[6]–[10]. The administration of agents with specificity for disease biomarkers opens up the field of Fluorescence Molecular Imaging (FMI), which has led to marked improvements in guiding surgery[11]–[16] and detecting cancer early[17] in pilot clinical studies.

Despite this early demonstration of clinical potential, the imaging performance of the method is limited by the interaction of photons with the tissue optical properties, i.e. scattering and absorption. This photon-tissue interaction degrades image quality, reduces the resolution in the optical image and negatively impacts the overall quantification accuracy and may lead to misinterpretation of fluorescence distribution in tissues[18]–[20]. In clinical studies, the dependence of the fluorescence image on optical properties may lead to false positives and false negatives[1], [12]. Moreover, blurry fluorescence images lead to uncertainty about the precise delineation of tumor margins and may impair the decision-making process during surgery, increasing the risk of incomplete tumor resection or excessive removal of healthy tissue.

While these FMI limitations are generally known[1], [12], [20], there has been limited methodology proposed to improve on the dependence of fluorescence images on optical properties and/or light diffusion[21], [22]. Computational methods have been considered for improving decision making during surgery by estimating tumor borders based on adaptive thresholds[23], but they operate on uncorrected fluorescence images that are subject to image degradation due to photon diffusion. Another promising strategy performs FMI in the so-called second near-infrared optical window (NIR-II, 1000-1400 nm)[24], [25], due to the known reduction of photon scattering with increasing wavelength. While signals collected in NIR-II experience less scattering than in the NIR, the image dependence on tissue optical properties does not fundamentally change in the NIR-II. Scattering remains a source of resolution reduction and tissue absorption is generally greater in the NIR-II than in the NIR-I, which makes images more strongly dependent on absorption depending on tissue type and experimental conditions. Structured illumination methods have been suggested for improving the contrast and resolution of fluorescence imaging by selectively exciting specific spatial modes in tissue that favor the target imaged[26], [27]. Demonstrated in phantoms and animals, this class of methods generally requires scanning different spatial patterns in tissue. To address this problem, a method that retrieves optical properties as a single snap-shot has been suggested[21].

Fluorescence images are then corrected using a computational model, which however does not take into account spatial dependencies across the image, but only corrects the intensity of the images on a pixel-to-pixel basis.

Deconvolution is more commonly used for image enhancement in a variety of applications spanning astronomy[28], computer vision[29], widefield fluorescence microscopy[30] and confocal microscopy[31]. The deconvolution procedure treats the acquired image as the convolution of the original image (ground truth) with a degradation kernel. Then, the convolution process is computationally "inverted", leading to the original image. Deconvolution operations typically work on the assumption that image modification is due to imperfections of the measurement device employed. Typically, in optical systems, a space- and time-invariant kernel is employed, termed a point spread function (PSF), which is dependent on the hardware properties of the device utilized.

Even though deconvolution is well established in other imaging fields, its application to clinical fluorescence images has not been widely considered[32], because FMI degradation depends primarily on the optical properties of the tissue imaged and not on the acquisition device. For example, the resolution of a charge-coupled device (CCD) camera can be on the order of a few tens of microns, such that the physical limits of photon diffusion result in an image with a resolution at least one order of magnitude worse. Typically, tissues in the surgical field of view vary in the amount of scattering and absorption and the images collected may be further affected by bleeding and other fluids. Therefore, the FMI degradation kernel is spatially dependent on the tissue imaged and generally not known, limiting the application of deconvolution to FMI images. In light of the expanding clinical applications of FMI, there remains a critical unmet need to develop approaches that revert the effect of tissue on FMI performance[20] and lead to accurate fluorescence images, overcoming the aforementioned challenges.

We hypothesized that the combination of two novel concepts relating to capturing and reverting the effect of optical properties would lead to improving FMI performance. The first concept relates to spatially resolving the effects of tissue on the fluorescence image. The second concept relates to using this spatially dependent information to correct fluorescence images, enabling for the first time the application of deconvolution to FMI. Uniting these two concepts, we introduce herein Spatially Adaptive Impulse Response Correction (SAIRC), a novel framework that uses spatially variable kernels in an adaptive fashion to correct the fluorescence images. The inventive step of the method is the use of an inexpensive Digital Light Processing

(DLP) projector that excites spatial impulse responses (PSFs) across the field of view imaged by projecting illumination points (delta functions) onto tissue. SAIRC captures these spatial impulse responses of tissue and assembles them in a matrix of spatially varying kernels that drives a variant deconvolution scheme. We developed spatially adaptive deconvolution based on a modified fast Lucy-Richardson algorithm[33]. In this paper, we describe studies to demonstrate the SAIRC principle in phantoms and animal measurements, and we discuss how SAIRC can be implemented in clinical FMI systems for real-time applications.

Results

Phantoms and tissues were imaged using a previously described FMI system (Fig. 1a) used in clinical studies in open surgery[11], [23], [34] or endoscopy[17], [35]–[39] and illuminated by a spatial impulse response, using the red channel of a DLP projector (wavelength, 624 ± 18 nm) (Fig. 1b), that was scanned throughout the tissue. The broadening of the impulse responses emitted at tissues was captured by a monochromatic camera (Fig. 1c). Different parts of tissue from an HCT116 tumor-bearing mouse demonstrated different broadening, which is characteristic of different optical properties. As an example, highly scattering cancerous tissue (spot d; Fig. 1c) shows higher broadening (Fig. 1d) compared to an impulse response collected from intestinal and muscle tissue (spots e, f; Fig. 1c) that show less broadening (Fig. 1e,f). At each of the three spots studied herein, we fitted a 2D symmetrical Gaussian function (Fig. 1g) to better illustrate the differences in broadening and optical properties among the different tissue types.

We extracted the standard deviation (sigma) from each fitted Gaussian for random spots (spots d-f; Fig. 1c and for four spots in each of the areas 1 (cancer), 2 (intestinal), and 3 (muscle), where each of the areas was defined as having relatively uniform optical properties. The sigma value distribution (Fig. 1h) showed that sigma varied only slightly within each area, and that the sigma distribution varied significantly across different areas according to Mann-Whitney test (Fig. 1h). After scanning the entire tissue surface with the projected DLP point and extracting the sigma value from each Gaussian fitting (see Methods; Retrieval of the kernels), we assembled a 2D sigma map (Fig. 1i) that displays the spatial variation in tissue diffusion. The sum of all the projected points (Fig. 1j) resembles the illumination of the tissue with a homogeneous planar source.

The sigma map (Fig. 1i) was also employed to assemble the PSFs that were used for variant deconvolution of the blurred fluorescence image of the tissue. From the histogram of the sigma

map (Fig. 1k), the sigma values were binned into n equally sized bins, and the lowest value of each bin was used to construct a Gaussian kernel. This kernel was deconvolved with the raw blurry fluorescence image using a modified Lucy-Richardson deconvolution scheme. The deconvolution process was repeated for every binned kernel, and the final corrected fluorescence image was constructed using a weighted summation of all the deconvolved images. This binning process minimized the deconvolution time with multiple kernels.

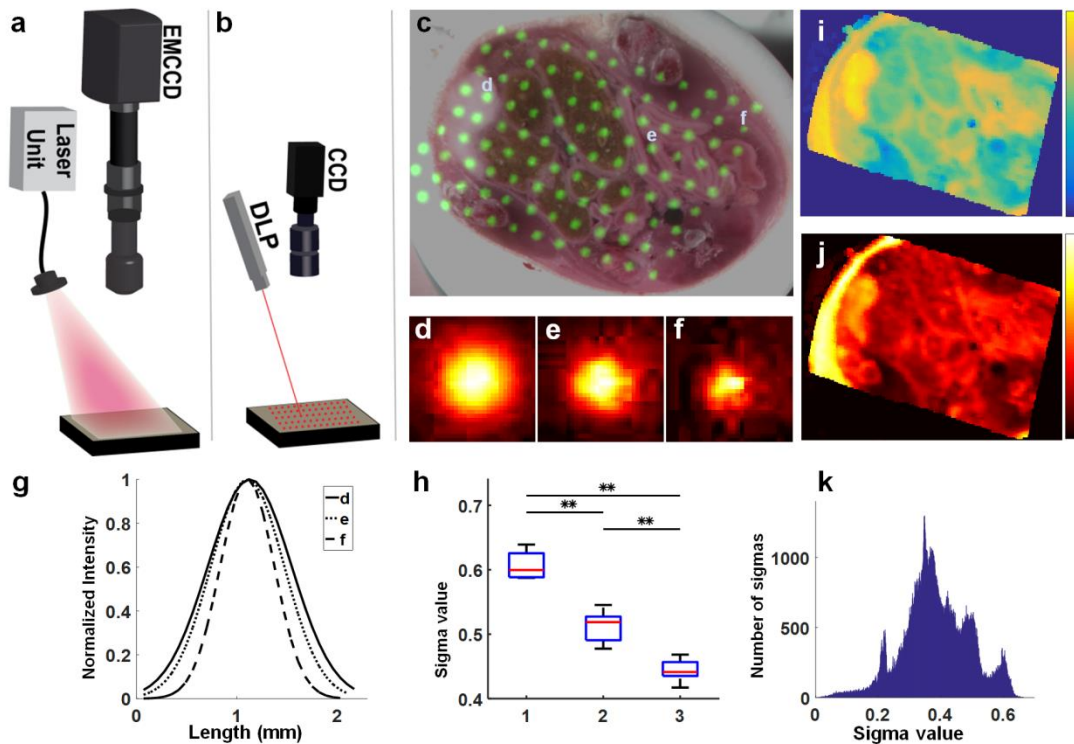


Figure 1: Schematic of the SAIRC process to enhance fluorescence imaging. Schematic system configuration for (a) fluorescence image acquisition and (b) scanning with the projector. (c) Color image of tissue from a mouse with an HCT116 tumor embedded in OCT (Optical Cutting Temperature) compound after several cuts, overlaid (green pseudocolor) with some of the acquired impulse response images from the scanned area. The small panels underneath show images of spots from different areas: (d) tumor; (e) intestine; (f) muscle. Spots d, e and f are indicated in panel (c). (g) Comparison of the normalized profile of Gaussian curves fitted to the points d, e, and f. (h) Distribution of the sigma values fitted to five random spots chosen from areas 1, 2, 3 around points d, e, f. (i) Two-dimensional sigma map, extracted from the fitted Gaussians for the whole scanning area. (j) Sum of all the acquired impulse response images. (k) Histogram of sigma values binned into n bins, each of which contained the same number of sigma values. ** $p < 0.01$

We designed a phantom to explore basic parameters of the proposed SAIRC framework and to determine SAIRC performance in acquired images containing substantial noise (Fig. 2). A cross-shaped agar phantom containing Alexa Fluor 750 and dairy cream ($\mu_s = 150 \text{ cm}^{-1}$, $\mu_a = 0.05 \text{ cm}^{-1}$) (Fig. 2a) was embedded into a background agar medium consisting of areas with different optical properties (Fig. 2b). The background medium consisted of area i ($\mu_s = 150 \text{ cm}^{-1}$, $\mu_a = 2.32 \text{ cm}^{-1}$), area ii ($\mu_s = 150 \text{ cm}^{-1}$, $\mu_a = 1.16 \text{ cm}^{-1}$) and area iii ($\mu_s = 150 \text{ cm}^{-1}$, $\mu_a = 0.58 \text{ cm}^{-1}$), each formulated with different concentrations of black ink (see Methods; Targets; Phantom). Because of their different optical properties, these areas should modify the projected points differently.

Fig. 2c was considered the ground truth image (see Methods; System and data acquisition; Ground truth images) and shows the fluorescence image of the phantom in Fig. 2a which was surrounded by air. Fig. 2d shows the raw fluorescence image of the phantom of Fig. 2b. We can observe the difference between the edges of area i and the edges of areas ii and iii: the edges in area i appear better resolved as compared to areas ii and iii. Instead, diffusion dominates in areas ii and iii, where the phantom's edges appear more blurry. Fig. 2e shows the results of the SAIRC process. Then, the results of SAIRC were compared with those obtained using regularized Wiener deconvolution (see Methods; Data Processing; Evaluation of Performance), which applies regularization and a fixed PSF (Fig. 2f). As can be seen, the SAIRC-corrected image (Fig. 2e) was better resolved than the original fluorescence image (Fig. 2d) and the image obtained from the Wiener deconvolution method (Fig. 2f), while it resembled the ground truth image (Fig. 2c) more closely. The edges were adequately restored from round to rectangular, recovering the original shape of the phantom; in addition, the noise artifacts were suppressed by the use of the regularization term λ , and the shape was smoothed out. It was necessary to use a relatively high λ value, reflecting the greater amount of noise in the acquired image.

To quantify the ability of SAIRC to restore image sharpness and edge quality, we drew line fluorescence intensity profiles across two different regions of the phantom (dotted blue lines 1 and 2 in Fig. 2b). In Fig. 1g we compared the intensity profiles in the raw, SAIRC, regularized Wiener and ground truth images, and we observed that the SAIRC profile was closest to the ground truth image for both lines. Furthermore, we assessed the image sharpness by calculating the Brenner gradient (see Methods; Data Processing; Evaluation of Performance), which was 0.0018 for the initial image, 0.0022 for the SAIRC-corrected image and 0.0010 for the regularized Wiener image. Consequently, the SAIRC-corrected image was 22% sharper

than the initial image. The root mean square (RMS) difference from the ground truth image was estimated to be 0.0621 for the initial image, 0.0445 for the SAIRC-corrected image, and 0.0457 for the regularized Wiener corrected image. This indicates that SAIRC increased similarity to the ground truth image by 28% compared to the raw image.

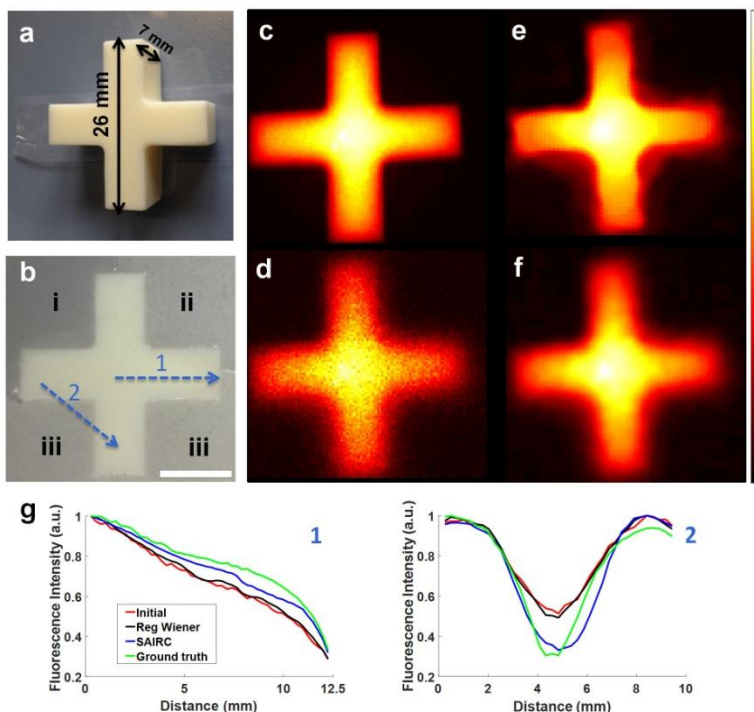


Figure 2: SAIRC improvement in fluorescence image quality of a phantom. (a) Color photograph of the phantom surrounded by air. (b) Color photograph of the phantom surrounded by three areas (i, ii, iii) with different optical properties based on different ink concentrations (see main text). Scalebar: 10 mm. (c) Ground truth fluorescence image. (d) Raw fluorescence image of panel (b). (e) Fluorescence image after the implementation of SAIRC. (f) Fluorescence image after the implementation of regularized Wiener deconvolution. (g) Fluorescence intensity profiles 1 and 2 from panel (b). Intensities 1 and 2 are normalized to 0-1. Initial: Raw Fluorescence Image, Reg Wiener: regularized Wiener deconvolution, SAIRC: Deconvolved Image with spatially adaptive kernels.

Encouraged by these results in phantoms, we tested our SAIRC algorithm by imaging abdominal cryosections of mouse bearing 4T1 tumor injected with the tumor-targeting fluorescence agent Integrinsense 750, or mice bearing HCT116 tumors expressing the near-infrared fluorescent protein iRFP720.

Fig. 3 shows the performance of the SAIRC method for imaging mouse bearing a 4T1 tumor. Upper panels of Fig. 3a and 3b depict color images of the OCT-embedded tissue block and a thin slice from the block, respectively. Lower panels of Fig. 3a and 3b show the corresponding raw fluorescence images. The fluorescence image of the thin slice (Fig. 3b) was considered the

ground truth, due to its diffusion-free thickness. Comparison of the raw fluorescence image in Fig. 3b with the SAIRC-corrected fluorescence image (lower panel in Fig. 3c) shows that deconvolution process by using the acquired sigma map (upper panel of Fig. 3c) mitigated the effect of light diffusion on image quality, providing higher resolution, sharpness and resemblance to the ground truth image. Comparison of zoomed-in regions i, ii and iii further revealed how SAIRC correction clarified details in the fluorescence image, bringing it closer to the ground truth image. In fact, SAIRC was associated with a doubling of sharpness, as quantified with the Brenner gradient (0.0003 for Fig. 3a vs 0.0006 for Fig. 3c). SAIRC also increased similarity to the ground truth image by 37%, as quantified with RMS (Root Mean Square) (0.1918 for Fig. 3a vs 0.1402 for Fig. 3c). Some discrepancies between the corrected image and the thin slice can be attributed to tissue distortion during the cutting process.

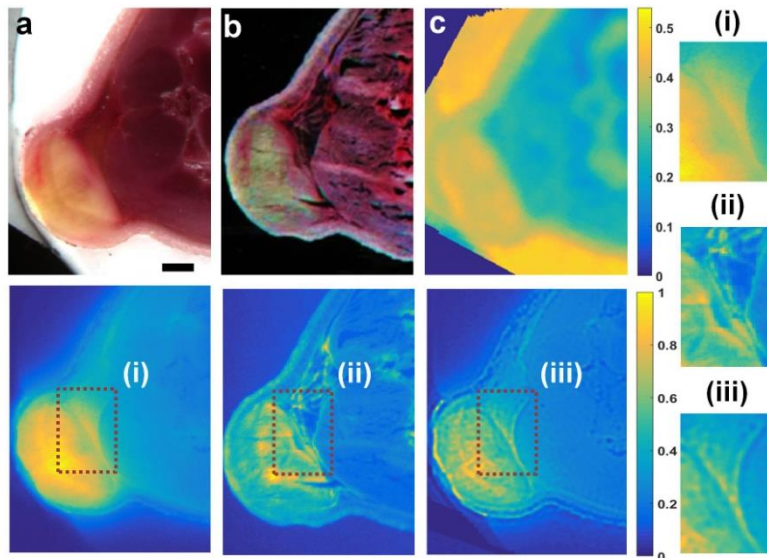


Figure 3: SAIRC improvement in the quality of fluorescence images of one mouse containing a 4T1 tumor injected with Integrinsense 750. (a) Upper: color image of the back of a mouse bearing a 4T1 tumor after embedding in OCT compound. Lower: the corresponding raw fluorescence image of the tissue block. Scalebar: 1 mm. **(b)** Upper: color image of a thin slice (50 μ m) from the OCT-embedded tissue block in front of a black background. Lower: the corresponding fluorescence image of the thin slice, which served as the ground truth image. **(c)** Upper: sigma map acquired from the scanning process (color bar in mm). Lower: corrected fluorescence image after the implementation of SAIRC. **(i-iii)**: Zoomed-in areas of the regions of interest in the lower images in panels (a), (b) and (c).

We observed similar improvements in image quality when we repeated the imaging experiments using tissue from two mice bearing HCT116 tumors expressing iRFP720 (Fig. 4). In this case SAIRC correction (Fig. 4c and g) brought the fluorescence images closer to the ground truth

image [Fig. 4d (i) and 4h (i)] than the initial images (Fig. 4b and 4f). As an additional verification of our results obtained with our custom FMI set-up, we obtained stitched fluorescence microscope images of the thin slices. The resulting images [Fig. 4d (ii) and 4h (ii)] were consistent with those from our in-house system. Some tumor characteristics, which are marked with white arrows, are not visible in the raw fluorescence image but are revealed after SAIRC correction.

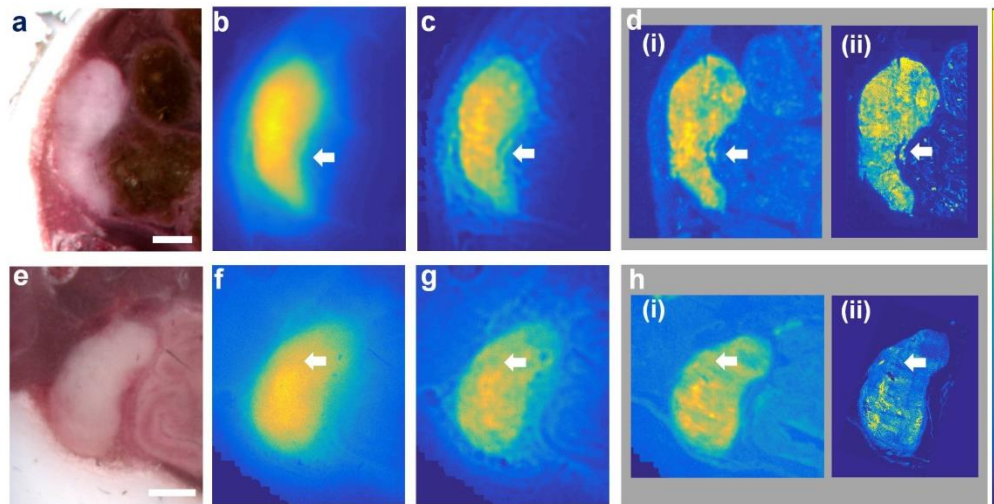


Figure 4: SAIRC improvement in quality of fluorescence images of mice bearing HCT116 tumors expressing IRFP720. The upper row corresponds to one mouse, while the lower row corresponds to a second mouse. **(a, e)** Color images of the abdominal area, after embedding in OCT compound. Scalebar: 1 mm. **(b, f)** Raw fluorescence image of the tissue block in panels (a) and (e). **(c, g)** Corrected image after the implementation of SAIRC. **(d, h)** (i) Fluorescence image of a thin slice (50 μm) of the tissue block obtained under the same conditions as the block image. (ii) Stitched images of the thin slices obtained from a commercial fluorescence microscope. White arrows indicate tumor features that become clearly distinguishable only after SAIRC correction.

Discussion

In this work, we demonstrate SAIRC, a novel fluorescence image correction scheme, which accurately captures optical property variations across the entire imaging area and enhances the acquired image via an iterative deconvolution process. A point-like beam from a DLP scans the imaging area, and spatially variant deconvolution kernels are retrieved from every corresponding beam region in the image and fitted to symmetrical Gaussian curves. Then, a Lucy-Richardson deconvolution method is applied, in which a regularization parameter[33] is used to suppress noise, and kernel spatial variability is binned in order to minimize

computational time. The final corrected image is the result of a weighted sum of the deconvolution results with the binned kernels. We validate and demonstrate the efficiency of our method using custom-made phantoms and ex vivo tissues from tumor-bearing mice. SAIRC improved fluorescence image resolution and contrast, increasing resemblance to the ground truth image by up to 37% and doubling the sharpness. This approach may increase the sensitivity and accuracy of FMI in preclinical and clinical applications, including surgical guidance and endoscopy.

In this work, we captured the diffusion modification at each point on the tissue by scanning over the tissue and translating the impulse response from every location to a representative value. This allowed us to visualize how diffusion in the tissue modifies the projected kernel in a 2D map. This information captures the spatial heterogeneity of the tissue and imports this spatial variability into a correction method based on deconvolution.

SAIRC correction enhanced image quality and structural details in phantoms and tumor tissue in mice. We further showed that SAIRC can perform well even when the acquired image contains a large amount of noise, such as with a highly noisy fluorescence phantom image. In this case, a higher value for the regularization parameter was needed. Sharpness of phantom images was enhanced by up to 22% relative to the initial fluorescence image, based on Brenner gradient estimation, while there was a 28% improvement compared with the initial image. We reduced the regularization parameter when processing the images of mouse tissue, where noise was less. In this case, the sharpness of the tissue image increased two-fold, and accuracy improved by 37%. We obtained greater improvements in sharpness and accuracy with mouse tissue than with phantoms. This can be attributed to the lower quality of the initial raw phantom image, where noise was greater. We further demonstrated that SAIRC provides better enhancement than another deconvolution method that uses regularization and invariant PSF.

SAIRC has the potential to be used with different combinations of imaging systems, tissue types and near-infrared fluorescence agents. The current method can be used with a variety of fluorescence agents upon proper modification of the projector light source, with the only limitation being the light penetration depth from both the excitation light and the projected scanning point. However, this intrinsic limitation is at the same time a great advantage of SAIRC, as the acquired data are not further blurred due to light propagating deep into tissues. SAIRC has the potential to be applied in fluorescence surgical navigation, where it can provide better insight into tumor structure and surroundings (Figs. 3-4). This is very important, since more accurate imaging of tumor areas offers better tumor delineation during surgical navigation and better insight into tumor topology. We envision the translation of SAIRC into a clinical FMI

environment, offering better tumor delineation and insights into tumor heterogeneity, especially since such application is mainly focused on surface-derived rather than depth-resolved information. To implement SAIRC into clinical FMI, which requires real-time visualization, the overall process of scanning reflected points, fitting, and deconvolution will need to be greatly accelerated. We are working towards improving the scanning speed by scanning with a grid of multiple points simultaneously and by using a parallel rather than serial regime to conduct fitting for the sigma extraction (see Supplementary Notes on “2. Faster scanning acquisition”).

The current method may be improved through more accurate kernel acquisition and better fitting. In this work we employed the raw resolution of the projector without any lens coupling in front, which limited the resolution of the acquired sigma map. By coupling the projector to a focusing lens system, it may be possible to increase the spot resolution, although this would reduce the field of view unless projectors with higher number of effective pixels are used. In addition, more sophisticated methods for fitting (e.g. summation of non-symmetrical Gaussians) and for weighing different deconvolution results may increase the accuracy of the final image, while scanning time can be reduced by projecting a grid rather than single points, as well as by using parallel programming. We anticipate that these planned SAIRC improvements will increase the achieved similarity to the ground truth image from 37% (rms value of the difference between the ground truth and corrected image) to a much higher value. We note that SAIRC should not be strongly affected by differences in light scattering by tissue at the two different wavelengths of excitation and emission (see Supplementary Notes on “1. Wavelength differences in SAIRC”). Nevertheless, we are currently working on implementing SAIRC with a laser-coupled projector that would enable at a variety of wavelengths and thus minimize any possible influence on SAIRC due to the difference in tissue optical properties between excitation and detection wavelengths.

A dual-tracer method for imaging tumors in vivo has recently been described[40], [41], in which a targeted tracer and a non-targeted one with close but separable fluorescence emission peaks are used to estimate tracer uptake by cancerous tissue. It may be possible to combine this method with SAIRC to generate tracer distributions of even higher resolution and accuracy. This will require additional work on SAIRC: although the method can correct for diffusion effects on fluorescence image resolution and contrast, it does not correct for the effect of absorption on the intensity of the fluorescence signal. The captured kernel can take into account optical properties and so may allow correction of fluorescence intensity[42], which we are currently exploring. In order to be more accurate for this correction we need to expand the SAIRC scheme with scanning acquisition with both excitation and emission wavelength. By scanning with the

corresponding wavelengths for both tracers and integrating this information into the SAIRC framework, we will be able to make the fluorescence signal more accurate and linearly proportional to the concentration of targeted and non-targeted tracers, disengaging the spatial variations in the optical properties of both tracer images of the heterogeneous tissue. This is critical[43] for the best performance of dual-tracer method. Then, the concentration and localization of the tracer can be estimated through a tracer compartmental model[44].

In summary, we demonstrated here the ability of SAIRC to correct fluorescence image degradation resulting from light diffusion and thereby a step closer towards improvement of distribution uptake of endogenous or exogenous tracers used in several clinical and basic research imaging applications. Combining our method with the range of fluorescence agents available, some of which efficiently target specific tissues such as tumors, and a dual tracer scheme may lead to new possibilities for imaging pathophysiological processes and guiding surgery. By extending the limits of fluorescence imaging, our method may help promote its incorporation into high-end imaging set-ups for surgery, endoscopy and other preclinical and clinical applications.

Methods

Targets

Phantom

A negative mold of a cross with dimensions 27 x 27 x 6 cm was developed and a mixture of scattering, absorbing, fluorescent agent and base material was cast inside the mold. Agar (1%) was selected as the base material, dairy cream (30% fat) as scattering agent, and acrylic ink as absorbing material. Alexa Fluor 750 (Thermo Fisher Scientific, Waltham, USA) was used as the fluorescent agent. The final composition of the phantom was 4 nM of Alexa Fluor 750, 15% fat dairy cream and 1% agar (Fig. 1a).

To test the efficacy of our deconvolution method, three additional areas of different optical properties were created around the fluorescence area. The three areas were formed by successive filling, solidifying and removing of excess agar, ink and cream milk in a petri dish. All

three areas contained 15% fat dairy cream. Area i also contained 0.25% ink; area ii, 0.125% ink; and area iii, 0.0625% ink (Fig. 2b).

Animal models

All animal procedures were performed in accordance with protocols approved by the Government of Upper Bavaria. The cryo-imaging experiments were performed with female NOD SCID Shorn mice (Envigo, Germany) approximately 8 weeks old. In two mice, 2×10^6 HCT116 human colon cancer cells expressing iRFP720 (ATCC, CCL-247, transfected in-house) were injected orthotopically into the abdominal area. In a third mouse, 1×10^6 4T1 breast cancer cells (ATCC, CRL-2539) were injected orthotopically into the mammary fat pad. All three tumors were allowed to grow until they reached a length of approximately 8 mm. Then, the animal bearing the 4T1 tumor was injected intravenously with Integrisense 750 (2 nmol; PerkinElmer), and sacrificed 24 h later. Mice were frozen at $-50\text{ }^{\circ}\text{C}$ and cryosliced as described previously[45][46] for imaging.

System and data acquisition

Fluorescence imaging

For the acquisition of the fluorescence phantom image, an optical system that has been previously described[47] was used. Briefly, a 750-nm, 300-mW Continuous Wave fiber-coupled diode laser (BWF2-750-0, B&W, Newark, USA) was employed for the excitation of the phantom and an NIR emission filter (ET810/90, Chroma, Rockingham, USA) for the emission. Fluorescence images were recorded using a fluorescence camera (512 x 512, DV897DCS-BV EMCCD, Andor, Belfast, Northern Ireland), whereas the reflectance images were captured using a 14-bit CCD grayscale camera (Grasshopper 3, PointGrey, Wilsonville, USA). The two images were automatically co-registered and the values of the sigmas were adjusted accordingly. Fluorescence images were automatically acquired using C++ software developed by our group[35].

For mouse cryo-imaging, a cryoslicing system[45] equipped with a fluorescence camera (Luca R EMCCD, Andor) was used. For the excitation of HCT116 mice, a 680-nm CW diode laser (B&W Tek, 300 mW) was used; for the 4T1 mouse, a 750-nm CW diode laser (B&W Tek, 300

mW) was used. A 721/42 filter (Chroma) was employed as emission filter for acquiring fluorescence images of the HCT116 mice and an LP 785 filter (Chroma) as emission filter for the 4T1 mouse. For the fluorescence images that were used as ground truth, thin slices of 50 μm from the block tissue were imaged using the cryo-imaging system.

Stitched fluorescence microscopy images were acquired using a Zeiss Axio Imager M2 microscope with a AxioCam MRm monochrome digital camera.

Ground truth images

In the case of phantoms, image distortion was considered to be caused mainly by the optical properties of the three areas surrounding the phantom and not by the fluorescent phantom itself. For this reason, the acquired image of the phantom surrounded by air was considered as the ground truth image and it was averaged to suppress the noise. In mouse tissue experiments, we considered the thin slice to be minimally affected by diffusion and therefore to be the closest to the true fluorescence distribution within the specific slice. We chose to acquire slices of 50 μm , so that fluorescence signal would be strong enough.

Retrieval of the kernels

Due to the spatial variability of the convolution kernel and the discrete nature of the image, we defined a $K(x,y)$ kernel function, where x,y are the pixel coordinates, to represent the kernels for every pixel within the captured image. To calculate each single kernel, we projected a point-like source onto the sample surface by means of a DLP projector (DLP 3000 Lightcrafter, Texas Instruments, Dallas, USA), and we recorded the reflection image produced. Each reflection image represents the spatially-resolved reflectance of the source and it depends on the optical properties of the sample at this specific point. We considered this image as an approximation for the unknown convolution kernel that essentially blurs the true fluorescence image locally. This point-like source was used to scan the entire area of interest (see supplementary Video, kernels with green pseudocolor), and all reflection images were recorded for the whole area. As a result, a unique kernel was assigned to each image pixel.

The projector was positioned above the sample at a very small angle (below 5 degrees) such that the projected spots did not appear distorted. Only the red LED channel (624 ± 18 nm) of the projector was utilized since it was the closest to the absorbance and emission peaks of the fluorescence agents in the phantom and mouse tissue. Instead of using the raw reflection image as a kernel, every reflection point image was fitted to a symmetrical, two-dimensional Gaussian

curve[48], [49], although more complex models involving sums of Gaussians exist[50]. Each Gaussian curve was considered homogeneous in all directions and the standard deviation value (sigma) was retrieved for every curve.

In order to retrieve values from the whole imaging surface, the latter was scanned by the point-like beam source on a pixel-by-pixel basis[51]. After Gaussian fitting and averaging[51] of the neighboring pixels, a two-dimensional array of sigma values was formed, containing a sigma value for every pixel of the acquired raw fluorescence image. The reflection images were recorded by means of a second camera, but it is also possible to use the fluorescence imaging camera without any emission filter. Sigma values were adjusted using the same calibration surface for the various experiments, and all the images were co-registered.

To correct for uneven light projection, the reflection image was divided by the reflection image of a homogeneous white surface when all the pixels of the projector were on. To disengage the projected spot from the projection system characteristics, we did the following. We considered that the measured kernel (K_{measured}) equals the convolution (equation 1) of the raw trace ($I_{\text{projector}}$) on the imaging surface with the unknown kernel (K) we were seeking. We assumed that kernel used in the deconvolution scheme (K) depends exclusively on the local optical properties of the tissue.

$$K_{\text{measured}} \approx I_{\text{projector}} * K \quad (1)$$

In order to estimate the spatially variable $I_{\text{projector}}$, we used a homogeneous black semi-reflective surface and repeated the aforementioned scanning procedure to retrieve reflectance images that approximate the $I_{\text{projector}}$. Symmetrical Gaussian curves were then fitted in an effective way (coefficient of determination > 0.85), and a two-dimensional array with sigma values was generated. Finally, since K_{measured} and $I_{\text{projector}}$ were both approximated by Gaussians, we could extract the sigma of the kernel K from the following equation (equation 2), which is based on Gaussian convolution properties:

$$\text{sigma}_K = \sqrt{\text{sigma}_{K_{\text{measured}}}^2 - \text{sigma}_{I_{\text{projector}}}^2} \quad (2)$$

Data Processing

Deconvolution

The raw acquired image was considered to be the result of a convolution operation of the true fluorescence image with a kernel that is dependent upon the optical properties of the imaging area. The distortion introduced by the optical imaging system was considered negligible compared to diffusion effects due to light-tissue interactions.

After assigning a sigma value to every pixel, we needed to perform deconvolution for each pixel separately. Nevertheless, a per-pixel deconvolution step would be extremely computationally intensive and, thus, time-consuming. Therefore, we binned the sigma values into n equally sized bins and the lowest sigma value of every bin was used to create a new Gaussian kernel which was taken as the input kernel for the upcoming deconvolution step. For the deconvolution step, we elected to perform a Lucy-Richardson iterative restoration method, widely used in other bioimaging applications. We also used a regularization constraint based on total variation to suppress the noise that is amplified during the iterations [33]. Finally, we performed m cycles of deconvolution and weighted the results according to eq. 3:

$$W_i = 1 - \left(\frac{|\text{sigma}(x,y) - \text{sigma}_{\text{bin}(i)}|}{\max(\text{sigma}) - \min(\text{sigma})} \right) \quad (3)$$

where W_i is the weight for the i th deconvolution of the (x, y) pixel, $\text{sigma}(x, y)$ is the corresponding sigma value from the sigma map and $\text{sigma}_{\text{bin}(i)}$ is the binned sigma value that was used for the construction of the kernel of the i th deconvolution. The contribution of each deconvolution result to a given pixel is higher when the sigma value of that pixel is closer to the sigma value of the kernel used to produce the deconvolution result. All computations were performed in MATLAB (Mathworks, USA).

Evaluation of performance

We examined the sharpness of the corrected fluorescence images using the Brenner gradient[52], which is an image differentiation function that can be used as a measure of image focus. The larger the gradient, the sharper the image is. Furthermore, the root mean square (RMS) of the difference between corrected and ground truth images was used as a metric to assess improvement due to the correction process. The lower the value, the more the corrected image resembles the ground truth.

Finally, we compared SAIRC with another deconvolution method that uses regularization and a fixed PSF. This method is based on regularized Wiener deconvolution[53] and is implemented in the ImageJ plugin FFTJ. For the PSF, we simulated a homogeneous Gaussian kernel based

on the average value from the sigma map. The regularization parameter was optimized by visual inspection in order to reach a compromise between blurriness and appearance of artifacts in the final image.

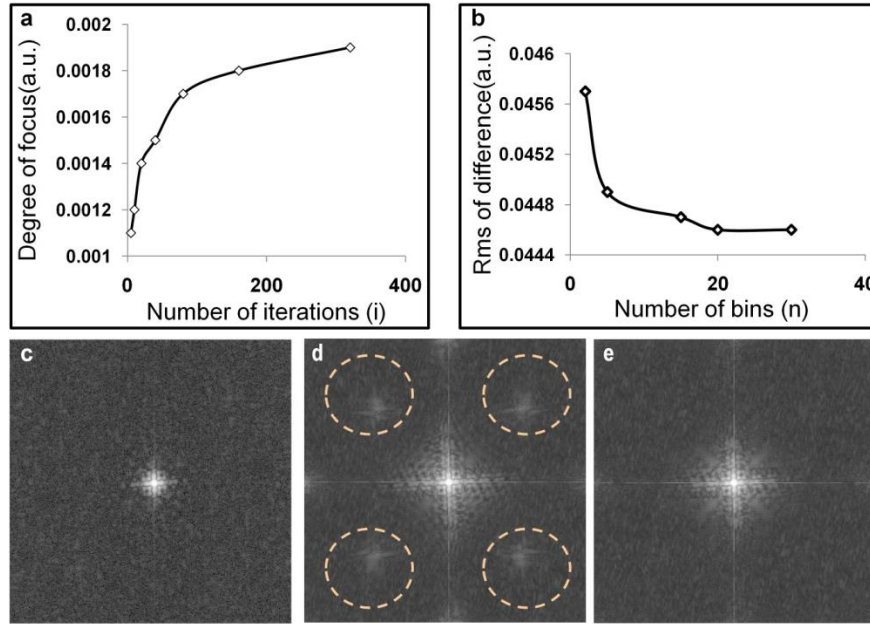


Figure 5: Metrics to estimate optimal parameters for the deconvolution algorithm. (a) Evaluation of image sharpness regarding the number of iterations. **(b)** Rms value of the image difference regarding the number of the sigma bins. **(c)** Amplitude Fourier domain of the initial fluorescence image. **(d)** Amplitude Fourier domain of the deconvolved fluorescence image (high λ). **(e)** Amplitude Fourier domain of a deconvolved fluorescence image (suitable λ).

Estimation of deconvolution parameters

In order to optimize the number of iterations, the number of bins, and the regularization parameter (λ), all of which are inputs in the deconvolution algorithm, we performed tests with different parameter combinations and identified the values that gave the best performance according to quality metrics. We tested the optimal number of iterations by assessing the image sharpness with respect to different iteration numbers. Fig. 5a depicts the Brenner's degree of focus measure regarding the number of iterations with a certain number of bins and λ (20 bins, $\lambda = 0.02$). We observed a trend of increasing Brenner's gradient as the iterations increased between 5 and 100. Beyond 100 iterations, the increase in sharpness slowed. Even if the degree of focus was slightly better after 300 iterations, some artifacts started to appear in the

image. For this reason, we performed < 300 iterations to keep computation time ~ 1 min without compromising image quality.

To select an appropriate amount of bins for the sigma values, we used as a metric the RMS of the difference between the corrected and ground truth fluorescence images. As observed in Fig. 5b, for a certain number of iterations and λ (iterations=100, $\lambda=0.02$), the RMS appeared to decrease with increasing number of bins, as expected. After 20 bins, though, the RMS appeared to start saturating, indicating that a large number of bins would not improve the quality of the deconvolution result. Thus, we may minimize the computational time by using only 20 bins.

The regularization parameter λ should be selected in a way that is high enough to suppress the image noise but low enough so it will not impede the restoration process. For high λ , points of very high intensity become more prominent because they are amplified at each iteration[33]. This can be noticed in the Fourier amplitude space of the image. Fig. 5c represents the amplitude Fourier space of the raw blurred fluorescence image, while Fig. 5d represents the equivalent for the deconvolved image. We observed that more frequency content was restored after deconvolution, as expected. Nevertheless, we also observed the amplification of other parasitic frequencies (dotted circles in Fig. 5d) as λ increased. For this reason, after inspecting the Fourier space of the deconvolved image, we selected the maximum λ just before the appearance of the parasitic frequencies. For the phantom, we selected λ values around 0.02, whereas for the tissue values around 0.001. The higher value of the phantom parameter can be attributed to the much greater noise in the phantom than in mouse tissue.

References

1. Koch, M. & Ntziachristos, V. Advancing Surgical Vision with Fluorescence Imaging. *Annu. Rev. Med.* **67**, 153–164 (2016).
2. Zhang, R. R. *et al.* Beyond the margins: real-time detection of cancer using targeted fluorophores. *Nat. Rev. Clin. Oncol.* **14**, 347–364 (2017).
3. Garland, M., Yim, J. J. & Bogoy, M. A Bright Future for Precision Medicine: Advances in Fluorescent Chemical Probe Design and Their Clinical Application. *Cell Chemical Biology* **23**, 122–136 (2016).
4. Haque, A., Faizi, M. S. H., Rather, J. A. & Khan, M. S. Next generation NIR fluorophores for tumor imaging and fluorescence-guided surgery: A review. *Bioorganic and Medicinal Chemistry* **25**, 2017–2034 (2017).
5. Hong, G., Antaris, A. L. & Dai, H. Near-infrared fluorophores for biomedical imaging. *Nat. Biomed. Eng.* **1**, 0010 (2017).
6. Schaafsma, B. E. *et al.* The clinical use of indocyanine green as a near-infrared

- fluorescent contrast agent for image-guided oncologic surgery. *J. Surg. Oncol.* **104**, 323–332 (2011).
7. Chi, C. *et al.* Intraoperative Imaging-Guided Cancer Surgery: From Current Fluorescence Molecular Imaging Methods to Future Multi-Modality Imaging Technology. *Theranostics* **4**, 1072–1084 (2014).
 8. Olson, M. T., Ly, Q. P. & Mohs, A. M. Fluorescence Guidance in Surgical Oncology: Challenges, Opportunities, and Translation. *Mol. Imaging Biol* **14**. 1–19 (2018).
 9. Boogerd, L. S. F. *et al.* Laparoscopic detection and resection of occult liver tumors of multiple cancer types using real-time near-infrared fluorescence guidance. *Surg. Endosc. Other Interv. Tech.* **31**, 952–961 (2017).
 10. Cornelissen, A. J. M. *et al.* Near-infrared fluorescence image-guidance in plastic surgery: A systematic review. *Eur. J. Plast. Surg.* **41**, 269–278 (2018).
 11. van Dam, G. M. *et al.* Intraoperative tumor-specific fluorescence imaging in ovarian cancer by folate receptor- α targeting: first in-human results. *Nat. Med.* **17**, 1315–1319 (2011).
 12. Scheuer, W., Van Dam, G. M., Dobosz, M., Schwaiger, M. & Ntziachristos, V. Drug-based optical agents: Infiltrating clinics at lower risk. *Science Translational Medicine* **4**, (2012).
 13. Hingorani, D. V *et al.* Nerve-targeted probes for fluorescence-guided intraoperative imaging. *Theranostics* **8**, 4226–4237 (2018).
 14. Belykh, E. *et al.* Intraoperative Fluorescence Imaging for Personalized Brain Tumor Resection: Current State and Future Directions. *Front. Surg.* **3**, (2016).
 15. Boogerd, L. S. F. *et al.* Folate receptor targeted near-infrared fluorescence imaging in high-risk endometrial cancer patients: a tissue microarray and clinical feasibility study. *Oncotarget* **9**, 791–801 (2018).
 16. Tummers, W. S. *et al.* Intraoperative Pancreatic Cancer Detection using Tumor-Specific Multimodality Molecular Imaging. *Ann. Surg. Oncol.* **25**, 1880–1888 (2018).
 17. Nagengast, W. B. *et al.* Near-infrared fluorescence molecular endoscopy detects dysplastic oesophageal lesions using topical and systemic tracer of vascular endothelial growth factor A. *Gut* **68**, 7–10 (2019).
 18. O'Kelly Priddy, C. M., Forte, V. A. & Lang, J. E. The importance of surgical margins in breast cancer. *Journal of Surgical Oncology* **113**, 256–263 (2016).
 19. Ethun, C. G. & Delman, K. A. The importance of surgical margins in melanoma. *Journal of Surgical Oncology* **113**, 339–345 (2016).
 20. Koch, M., Symvoulidis, P. & Ntziachristos, V. Tackling standardization in fluorescence molecular imaging. *Nat. Photonics* **12**, 505–515 (2018).
 21. Valdes, P. A., Angelo, J. P., Choi, H. S. & Gioux, S. qF-SSOP: real-time optical property corrected fluorescence imaging. *Biomed. Opt. Express* **8**, 3597 (2017).
 22. Gardner, C. M., Jacques, S. L. & Welch, A. J. Fluorescence spectroscopy of tissue: recovery of intrinsic fluorescence from measured fluorescence. *Appl. Opt.* **35**, 1780–1792 (1996).
 23. Koch, M. *et al.* Threshold Analysis and Biodistribution of Fluorescently Labeled Bevacizumab in Human Breast Cancer. *Cancer Res.* **77**, 623 LP – 631 (2017).
 24. Smith, A. M., Mancini, M. C. & Nie, S. Bioimaging: second window for in vivo imaging. *Nat. Nanotechnol.* **4**, 710–711 (2009).
 25. Antaris, A. L. *et al.* A small-molecule dye for NIR-II imaging. *Nat. Mater.* **15**, 235–242 (2016).
 26. Mazhar, A. *et al.* Structured illumination enhances resolution and contrast in thick tissue fluorescence imaging. *J. Biomed. Opt.* **15**, 010506 (2010).
 27. Sun, J. *et al.* Enhancing in vivo tumor boundary delineation with structured illumination fluorescence molecular imaging and spatial gradient mapping. *J. Biomed. Opt.* **21**, 80502

- (2016).
28. Starck, J. L., Pantin, E. & Murtagh, F. Deconvolution in Astronomy: A Review. *Publ. Astron. Soc. Pacific* **114**, 1051–1069 (2002).
 29. Ruiz, P., Zhou, X., Mateos, J., Molina, R. & Katsaggelos, A. K. Variational Bayesian Blind Image Deconvolution: A review. *Digit. Signal Process.* **47**, 116–127 (2015).
 30. McNally, J. G., Karpova, T., Cooper, J. & Conchello, J. a. Three-dimensional imaging by deconvolution microscopy. *Methods* **19**, 373–85 (1999).
 31. Laasmaa, M., Vendelin, M. & Peterson, P. Application of regularized Richardson-Lucy algorithm for deconvolution of confocal microscopy images. *J. Microsc.* **243**, 124–140 (2011).
 32. Krishnamurthi, G., Wang, C. Y., Steyer, G. & Wilson, D. L. Removal of subsurface fluorescence in cryo-imaging using deconvolution. *Opt. Express* **18**, 22324–22338 (2010).
 33. Dey, N. *et al.* Richardson-Lucy algorithm with total variation regularization for 3D confocal microscope deconvolution. *Microsc. Res. Tech.* **69**, 260–266 (2006).
 34. Lamberts, L. E. *et al.* Tumor-specific uptake of fluorescent bevacizumab-IRDye800CW microdosing in patients with primary breast cancer: A phase I feasibility study. *Clin. Cancer Res.* **23**, 2730–2741 (2017).
 35. Glatz, J. *et al.* Concurrent video-rate color and near-infrared fluorescence laparoscopy. *J. Biomed. Opt.* **18**, 101302 (2013).
 36. Hartmans, E. *et al.* Potential red-flag identification of colorectal adenomas with wide-field fluorescence molecular endoscopy. *Theranostics* **8**, 1458–1467 (2018).
 37. Tjalma, J. J. *et al.* Molecular fluorescence endoscopy targeting vascular endothelial growth factor a for improved colorectal polyp detection. *J. Nucl. Med.* **57**, 480–485 (2016).
 38. Harlaar, N. J. *et al.* Molecular fluorescence-guided surgery of peritoneal carcinomatosis of colorectal origin: a single-centre feasibility study. *Lancet Gastroenterol. Hepatol.* **1**, 283–290 (2016).
 39. Glatz, J. *et al.* Near-infrared fluorescence cholangiopancreatography: Initial clinical feasibility results. *Gastrointest. Endosc.* **79**, 664–668 (2014).
 40. Pogue, B. W. *et al.* Imaging targeted-agent binding in vivo with two probes. *J. Biomed. Opt.* **15**, 30513 (2010).
 41. Tichauer, K. M. *et al.* Improved tumor contrast achieved by single time point dual-reporter fluorescence imaging. *J. Biomed. Opt.* **17**, 066001 (2012).
 42. Kim, A., Khurana, M., Moriyama, Y. & Wilson, B. C. Quantification of in vivo fluorescence decoupled from the effects of tissue optical properties using fiber-optic spectroscopy measurements. *J. Biomed. Opt.* **15**, 067006 (2010).
 43. Kanick, S. C., Tichauer, K. M., Gunn, J., Samkoe, K. S. & Pogue, B. W. Pixel-based absorption correction for dual-tracer fluorescence imaging of receptor binding potential. *Biomed. Opt. Express* **5**, 3280–3291 (2014).
 44. Hamzei, N. *et al.* Comparison of Kinetic Models for Dual-Tracer Receptor Concentration Imaging in Tumors. *Austin J. Biomed. Eng.* **1**, 9 (2014).
 45. Symvoulidis, P., Perez, C. C., Schwaiger, M., Ntziachristos, V. & Westmeyer, G. G. Serial sectioning and multispectral imaging system for versatile biomedical applications. *2014 IEEE 11th Int. Symp. Biomed. Imaging* 890–893 (2014).
 46. Sarantopoulos, A., Themelis, G. & Ntziachristos, V. Imaging the bio-distribution of fluorescent probes using multispectral epi-illumination cryoslicing imaging. *Mol. Imaging Biol.* **13**, 874–885 (2011).
 47. Gorpas, D., Koch, M., Anastasopoulou, M., Klemm, U. & Ntziachristos, V. Benchmarking of fluorescence cameras through the use of a composite phantom. **22**, 16009–16012 (2017).

48. Reinisch, L. Scatter-limited phototherapy: a model for laser treatment of skin. *Lasers Surg Med* **30**, 381–388 (2002).
49. Steyer, G. J., Roy, D., Salvado, O., Stone, M. E. & Wilson, D. L. Removal of out-of-plane fluorescence for single cell visualization and quantification in cryo-imaging. *Ann. Biomed. Eng.* **37**, 1613–1628 (2009).
50. D'Eon, E. & Irving, G. A quantized-diffusion model for rendering translucent materials. *ACM Trans. Graph.* **30**, 1 (2011).
51. Gorpas, D., Ma, D., Bec, J., Yankelevich, D. R. & Marcu, L. Real-Time Visualization of Tissue Surface Biochemical Features Derived from Fluorescence Lifetime Measurements. *IEEE Trans. Med. Imaging* **35**, 1802–1811 (2016).
52. Santos, A. *et al.* Evaluation of autofocus functions in molecular cytogenetic analysis. *J. Microsc.* **188**, 264-272 (1997).
53. Gonzalez, R. & Woods, R. *Digital image processing*. Prentice Hall (2002).

Supplementary Notes

Fluorescence imaging reversion using spatially variant deconvolution

Maria Anastasopoulou^{1, 2}, Dimitris Gorpas^{1, 2}, Maximilian Koch^{1, 2}, Evangelos Liapis^{1, 2}, Sarah Glasl², Uwe Klemm², Angelos Karlas^{1, 2}, Tobias Lasser³, Vasilis Ntziachristos^{1, 2,*}

¹ Chair of Biological Imaging and TranslaTUM, Technical University Munich, Munich, 81675, Germany

² Institute of Biological and Medical Imaging, Helmholtz Zentrum München, Neuherberg, 85764, Germany

³ Computer Aided Medical Procedures, Technical University Munich, Garching, 85748, Germany

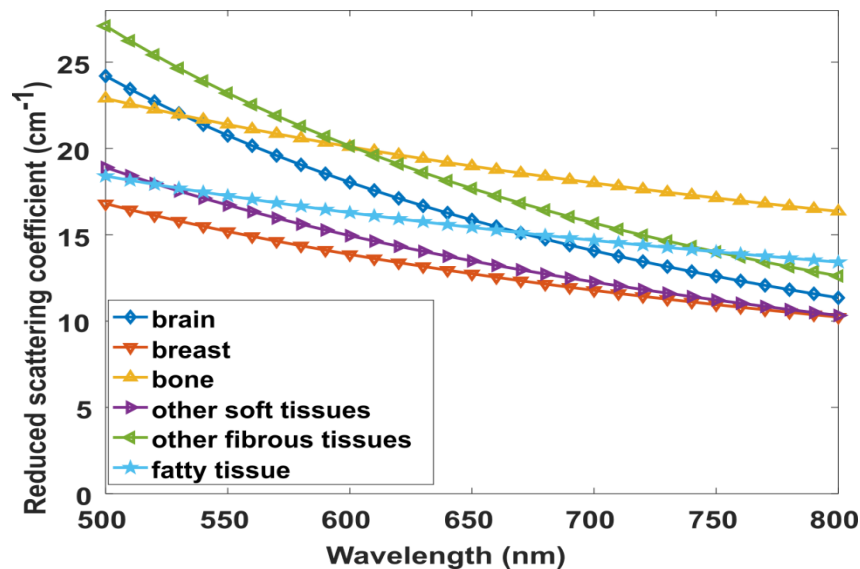
*v.ntziachristos@tum.de

1. SAIRC dependence on wavelength

Since light scattering is wavelength dependent, one would expect that excitation and emission light influence differently the formation of fluorescence images. Indeed, if the reduced scattering coefficient is approximated as a function of wavelengths, for the most common tissue components, from [1]:

$$\mu'_s = a \left(\frac{\lambda}{500(\text{nm})} \right)^{-b} \quad (4)$$

this variation can be observed in Suppl. Fig. 1. In equation (4) λ is the wavelength, a is a scaling factor term and b is the ‘scattering power’ term as fully described in [1]. The average values of a and b from [1] for different tissue components (i.e. brain, breast, bone, other soft tissues, other fibrous tissues, fatty tissue) were applied in equation (4). As shown in Suppl. Fig. 1, the difference between 500 nm and 800 nm is more than 40%. However, when excitation and emission wavelengths are relatively close, this difference becomes significantly smaller. For example in the mice bearing HCT116 tumors that express the near-infrared fluorescent protein iRFP720 (Fig. 4), the excitation was centered at 680 nm and emission at 721 nm, while SAIRC was implemented with a Digital Light Processing (DLP) configuration centered at 624 nm. This is translated to a scattering difference of 9% (averaged from all the components) between DLP and excitation and 15% between DLP and emission. Such values are small enough to be neglected during the development of SAIRC and to showcase its potential. Nevertheless, while working towards the optimization and expansion of SAIRC to also incorporate quantitative fluorescence intensity correction, the wavelength-dependent influence of the tissue optical properties to the acquired data will be considered.

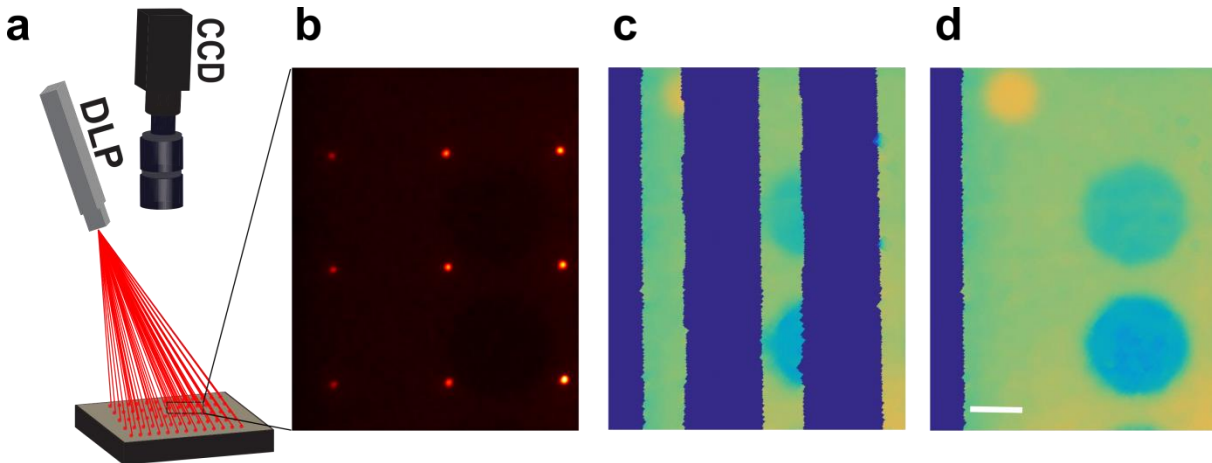


Suppl. Fig. 1: Reduced scattering coefficient for different tissues in the near-infrared range.

2. Faster scanning acquisition

The long-term objective of this study is the translation of SAIRC in clinical applications. That, however, necessitates significantly faster data acquisition. To this end, imaging and scanning of

a grid (Suppl. Fig. 2a) has the potential to significantly reduce acquisition time. This can be further improved by parallelizing the fitting process, in order to simultaneously analyze multiple points, by using a more sensitive camera (i.e. shorter exposure time) and higher computational power. Nevertheless, the preliminary results of Suppl. Fig. 2, that achieved six-fold acquisition time improvement compared to a single point raster scanning in data acquisition are shown.



Suppl. Fig. 2: Simultaneous acquisition of multiple points scanned on the sample. A solid phantom with wells of different optical properties [2] is being scanned. **(a)** Schematic of the DLP projector that projects a grid of points. **(b)** Projected points on the phantom surface with different optical properties. **(c)** Fitting and creation of the sigma map for all the grid points simultaneously. **(d)** Sigma map acquired from the scanning progress. DLP: DLP 3000 Lightcrafter, Texas Instruments, Dallas, USA. CCD: Grasshopper 3, PointGrey, Wilsonville, USA. Scalebar: 5 mm.

3. Supplementary Video: DLP scanning of a mouse bearing a 4T1 tumor

This video illustrates the scanning procedure with a single point raster scanning of a cryosectioned mouse bearing a 4T1 tumor, embedded in OCT (Optimal Cutting Temperature) compound, with the DLP projector. Kernel acquisition video is overlaid with green color on a grayscale image of the tissue.

References

- [1] S. L. Jacques, "Optical Properties of Biological Tissues: A Review," *Phys. Med. Biol.*, vol. 58, no. 11, pp. R37-61, 2013.
- [2] D. Gorpas *et al.*, "Multi-parametric Standardization of Fluorescence Imaging Systems Based on a Composite Phantom," *IEEE Trans. Biomed. Eng.*, p. 1, 2019.

Appendix C. Publication Record

Publications in international peer-reviewed journals

Karlas, A., Kallmayer, M., Fasoula, N. A., Liapis, E., Bariotakis, M., Krönke, M., **Anastasopoulou, M.**, Reber, J., Eckstein, H. H., & Ntziachristos, V. (2020). Multispectral optoacoustic tomography of muscle perfusion and oxygenation under arterial and venous occlusion: A human pilot study. *Journal of Biophotonics*. <https://doi.org/10.1002/jbio.201960169>

Gorpas, D., Koch, M., **Anastasopoulou, M.**, Bozhko, D., Klemm, U., Nieberler, M., & Ntziachristos, V. (2020). Multi-Parametric Standardization of Fluorescence Imaging Systems Based on a Composite Phantom. *IEEE Transactions on Biomedical Engineering*. <https://doi.org/10.1109/TBME.2019.2910733>

Anastasopoulou, M., Gorpas, D., Koch, M., Liapis, E., Glasl, S., Klemm, U., Karlas, A., Lasser, T., & Ntziachristos, V. (2019). Fluorescence imaging reversion using spatially variant deconvolution. *Scientific Reports*. <https://doi.org/10.1038/s41598-019-54578-0>

Karlas, A., Reber, J., Diot, G., Bozhko, D., **Anastasopoulou, M.**, Ibrahim, T., Schwaiger, M., Hyafil, F., & Ntziachristos, V. (2017). Flow-mediated dilatation test using optoacoustic imaging: a proof-of-concept. *Biomedical Optics Express*. <https://doi.org/10.1364/boe.8.003395>

Gorpas, D., Koch, M., **Anastasopoulou, M.**, Klemm, U., & Ntziachristos, V. (2017). Benchmarking of fluorescence cameras through the use of a composite phantom. *Journal of Biomedical Optics*. <https://doi.org/10.1117/1.jbo.22.1.016009>

Anastasopoulou, M., Koch, M., Gorpas, D., Karlas, A., Klemm, U., Garcia-Allende, P. B., & Ntziachristos, V. (2016). Comprehensive phantom for interventional fluorescence molecular imaging. *Journal of Biomedical Optics*. <https://doi.org/10.1117/1.jbo.21.9.091309>

Publications in Conference proceedings

Dimitris Gorpas, **Maria Anastasopoulou**, Maximilian Koch, Uwe Klemm, Markus Nieberler, Vasilis Ntziachristos, "Standardization phantom for intra-operative fluorescence molecular imaging," Proc. SPIE 11079, Medical Laser Applications and Laser-Tissue Interactions IX, 1107913 (22 July 2019); <https://doi.org/10.1117/12.2530283>

Dimitris Gorpas, Maximilian Koch, **M. Anastasopoulou**, Uwe Klemm, Vasilis Ntziachristos, "Phantom and methodology for fluorescence molecular imaging systems benchmarking," Proc. SPIE 10677, Unconventional Optical Imaging, 106771G (24 May 2018); <https://doi.org/10.1117/12.2309766>

Dimitris Gorpas, Maximilian Koch, **Maria Anastasopoulou**, Uwe Klemm, Vasilis Ntziachristos, "Standardization of fluorescence molecular imaging systems," Proc. SPIE 10413, Novel Biophotonics Techniques and Applications IV, 104130J (28 July 2017); <https://doi.org/10.1117/12.2286065>

Maria Anastasopoulou, Dimitris Gorpas, Maximilian Koch, Pilar Beatriz Garcia-Allende, Uwe Klemm, Angelos Karlas, Vasilis Ntziachristos, "Multiparameter solid phantom for fluorescence imaging standardization," Proc. SPIE 10411, Clinical and Preclinical Optical Diagnostics, 104110J (28 July 2017); <https://doi.org/10.1117/12.2286059>

Papers in preparation

Xiaopeng Ma[†], **Maria Anastasopoulou**[†], Maximilian Koch, Sarah Glasl, Oliver T. Bruns, Dimitris Gorpas, Vasilis Ntziachristos, “Performance trade-off in shortwave and near infrared ICG imaging for clinically relevant parameters.”

Augusto Arias, **Maria Anastasopoulou**, Dimitris Gorpas, Vasilis Ntziachristos, “Fluorescence intensity correction through the parametrization of the spatially resolved local reflectances.”

[†]: shared first author

Appendix D. Acknowledgements

The work presented herein was only feasible due to the support that I received during my research journey from several people.

First and foremost, I would like to thank my supervisor Prof. Vasilis Ntziachristos for giving me the opportunity to work in the inspiring field of biomedical imaging, providing me with excellent technical and financial means. I am grateful for all the guidance and feedback he provided me during challenging parts of work and the knowledge and inspiration he offered not only for better problem solving, but also for communicating better the results to an audience.

I would also like to thank Dr. Dimitris Gorpas, who was my group leader and advisor during my PhD studies and he was always available to discuss theoretical and technical problems and to offer his help and guidance. Additionally, I would like to thank Maximilian Koch, who, along with Dimitris offered their valuable support to critical parts of my work.

I also want to thank Sarah Glasl and Uwe Klemm for all the assistance they offered regarding mice and lab procedures. I would also like to thank Dr. Tobias Lasser for his support and discussions regarding computational aspects.

I enjoyed working with Dr. Chapin Rodriguez and Dr. Robert Wilson, our scientific writers, who helped me improve my writing skills.

Many thanks to Prof. Englmeier Karl-Hans, Dr. Andreas Hillmaier, Susanne Stern and Lidia Seidl for their immediate support to any educational or administrative issue that would arise. I would like also to express my gratitude to Mr. Thomas Gerlach from Helmholtz Zentrum workshop that would happily discuss any machining issue.

I want also to thank the current members of the Fluorescence Imaging Group Dr. Augusto Gallego Arias, Dr. Mikhail Mazurenka, Philipp Rauschendorfer, Anna Tenditnaya, Elena Kriukova, Ivo Lipkowitsch, Dr. Sabrina Marcazzan for our nice coffee breaks, discussions and support as long as the past group members Dr. Xiaopeng Ma and Dr. Dmitry Bozhko.

I want also to acknowledge the contribution of my predecessors on the projects Dr. Juergen Glatz, Dr. Beatriz Pilar Garcia-Allende and Dr. Panos Symvoulidis for setting the ground for those projects. I would like also to thank Dr. Angelos Karlas for our nice collaboration both in fluorescence and optoacoustic projects. I would not want to forget mentioning Dr. Roland Boha, Dr. Doris Bengel, Dr. Evangelos Liapis and Pia Anzenhofer for their support.

I would not like to forget to thank Vasilis Sarantos and his team in Rayfos Ltd for our awesome collaboration in PRISAR project and the financial support in the first year of my PhD studies.

Last but not least I would like to thank all my colleagues for our thought provoking discussions and willingness to help such as Dr. Gael Diot, Dr. Dominik Soliman, Antonis Stylogiannis, Kaushik Bashak Chowdury etc.

Appendix E. Letters of approval from publishers

Publication 1: Comprehensive phantom for interventional fluorescence molecular imaging



RE: Request for using my: <https://doi.org/10.1117/1.JBO.21.9.091309> article in cumulative April 6, 2020 5:54 PM

PhD thesis

From: "Katie Sinclair" <katies@spie.org>

To: "Maria Anastasopoulou" <maria.anastasopoulou@helmholtz-muenchen.de>

Dear Ms. Anastasopoulou,

Thank you for seeking permission from SPIE to reprint material from our publications. The article you have requested to reprint from is published under Creative Commons (CC BY 4.0)—Gold Open Access. For articles published under CC BY 4.0, users are free to share (copy, distribute, and transmit), to remix (adapt), and to make commercial use of the Article under the following conditions:

Attribution: Users must attribute the contribution in the manner specified by the licensor (but not in any way that suggests that they or their use of the Article is endorsed by the licensor). See citation formatting below.

Notice: For any reuse or distribution, users must make clear to others the license terms of this work, preferably using a link to the [Creative Commons webpage](#).

The full legal code of the CC BY 4.0 license can be found at <https://creativecommons.org/licenses/by/4.0/legalcode>.

Citation format (Journals):

Author(s), "Article Title," Journal Title and Volume Number (Issue), Article Number (Publication Date). [http://dx.doi.org/...](http://dx.doi.org/)

Best wishes on your dissertation. Please let me know if I may be of further assistance.

Best,

Katie Sinclair
Editorial Assistant, Publications
SPIE – the international society for optics and photonics
katies@spie.org
1 360 685 5436

SPIE.

Publication 2: Fluorescence imaging reversion using spatially variant deconvolution



RE: Request for using my 10.1038/s41598-019-54578-0 article in cumulative PhD thesis

April 2, 2020 1:19 PM

From: "journalpermissions" <journalpermissions@springernature.com>

To: "Maria Anastasopoulou" <maria.anastasopoulou@helmholtz-muenchen.de>

Dear Maria,

Thank you for your recent Springer Nature permissions request. This work is licensed under the Creative Commons Attribution 4.0 International License, which permits unrestricted use, distribution, modification, and reproduction in any medium, provided you:

- 1) give appropriate acknowledgment to the original author(s) including the publication source,
- 2) provide a link to the Creative Commons license/include a notice of the CC license in legend and reference, and indicate if changes were made.

You are not required to obtain permission to reuse this article, but you must follow the above two requirements.

Images or other third party material included in the article are encompassed under the Creative Commons license, unless indicated otherwise in the credit line. If the material is not included under the Creative Commons license, users will need to obtain permission from the license holder to reproduce the material.

To view a copy of the Creative Commons license, please visit <http://creativecommons.org/licenses/by/4.0/>

Please let me know if you have any questions.

Best wishes,
Oda

Oda Sigveland
Rights Executive

SpringerNature
The Campus, 4 Crinan Street, London N1 9XW,
United Kingdom
T +44 (0) 207 014 6851

<http://www.nature.com>
<http://www.springer.com>
<http://www.palgrave.com>